GRANT/GODDARD
IN-47

62657 CR

A Progress Report to

The National Aeronautics and Space Administration P-175

for NASA Contract NAG5-580

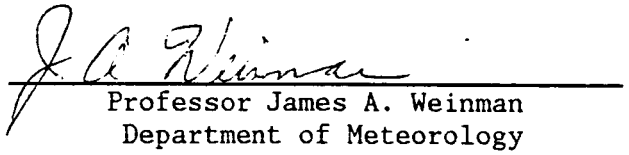
Determine Precipitaion Rates from Visible and Infrared Satellite Images of Clouds by Pattern Recognition Techniques

For the Period of

1 July 1985 - 31 March 1987

Submitted by

Space Science and Engineering Center (SSEC)
at the University of Wisconsin-Madison
1225 West Dayton Street
Madison, Wisconsin 53706
(608)262-0544



Professor James A. Weinman
Department of Meteorology

(NASA-CR-180261) DETERMINE PRECIPITATION RATES FROM VISIBLE AND INFRARED SATELLITE IMAGES OF CLOUDS BY PATTERN RECOGNITION TECHNIQUE Progress Report, 1 Jul. 1985 - 31 Mar. 1987 Ph.D. Thesis (Wisconsin Univ.) G3/47

N87-19850

Unclas
43498

April 8, 1987

UPDATED RESUME AND RESEARCH PROGRESS ON A GRANT TO "DETERMINE PRECIPITATION RATES FROM VISIBLE AND INFRA-RED SATELLITE IMAGES"

ACCOMPLISHED RESULTS:

Our previous work on rainfall retrieval from satellite imagery sought to retrieve rainfall rates in three categories from GOES visible and infra-red images of convective precipitation cells. This work was described in the paper by Wu et al. (1985) (Enclosure 1). That work used statistical texture and radiance features of the imagery to classify the rain in the categories of no, light and medium intensity rain.

A more advanced cloud pattern analysis algorithm was subsequently developed to take the shape and brightness of the various clouds into account in a manner that is more consistent with the human analyst's perception of GOES cloud imagery. The results of that classification scheme were compared with precipitation probabilities observed from ships of opportunity off the U.S. east coast to derive empirical regressions between cloud types and precipitation probability. The cloud morphology was then quantitatively and objectively used to map precipitation probabilities during two winter months during which severe cold air outbreaks were observed over the northwest Atlantic. This work was part of the Ph.D. research of Louis Garand. Table 1 summarizes precipitation probabilities associated with various cloud types. Fig. 1 compares maps of precipitation probability derived from the cloud morphology analysis program for two months and the precipitation probabilty derived from thirty years of ship observation.

Table 1: Frequency of occurrence of precipitation for various cloud classes

Class	Number of Cases	Prob. (%)
Clear	37	0.0
Stratus	29	6.9
Scattered cumulus	101	7.9
Scatt. stratocumulus	49	8.2
Broken cumulus	15	20.0
Cloud streets	37	13.5
Rolls	43	41.9
Polygonal open cells	24	29.2
Convective open cells	18	55.6
Bright closed cells	62	17.7
Nimbostratus	84	52.4
Altocumulus	40	20.0
Altocumulus & other	29	24.1
Thin cirrus	52	0.0
Multilayer cirrus	106	14.2
Cumulonimbus & cirrus	163	58.3
Dense cirrostratus	33	27.3
Overcast cumulonimbus	113	72.6

ORIGINAL PAGE IS
OF POOR QUALITY

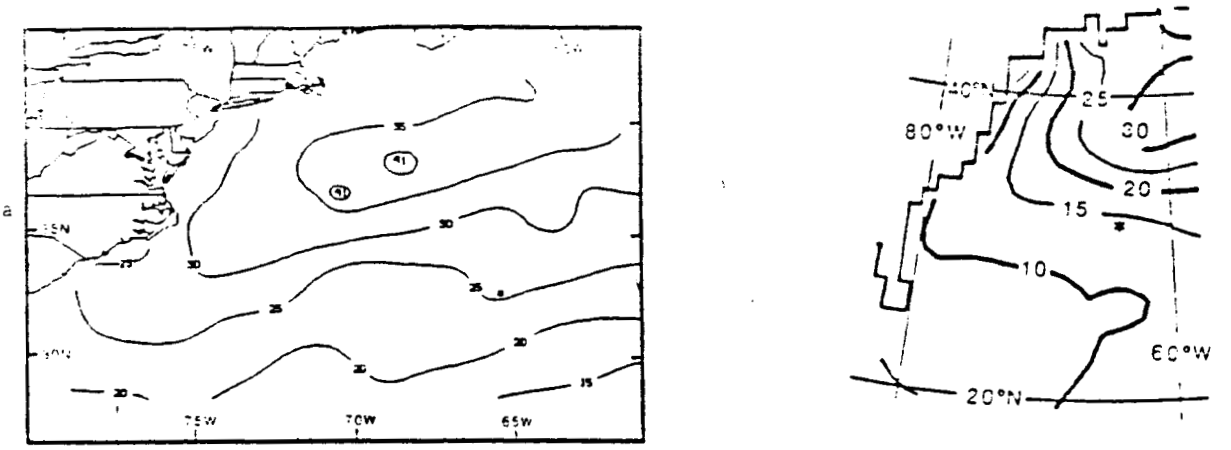


Fig. 1. Mean probability of precipitation retrieved from 11761 cloud images 128 × 128 Km for January and February 1984 and the thirty year climatology of January from Isemer and Hasse's (1985) climatological atlas.

A somewhat unexpected result that emerged from Dr. Garand's analysis of the GOES imagery was the development of a technique to derive surface air and dew point temperatures in cloud capped marine boundary layers. As a consequence it appears that surface air temperatures over the ocean can be derived within an r.m.s. 2 K at a spatial resolution of 128 Km. Fig. 2 shows a time series that compares air temperatures measured by a buoy for two months with those derived from this technique. The cold air outbreaks that correspond to temperature changes of ~ 20 K are clearly determined by this technique. Fig. 3 compares air temperature maps obtained by this technique with those obtained from thirty years of ship data. The influence of the Gulf Stream boundary is evident in the satellite derived data.

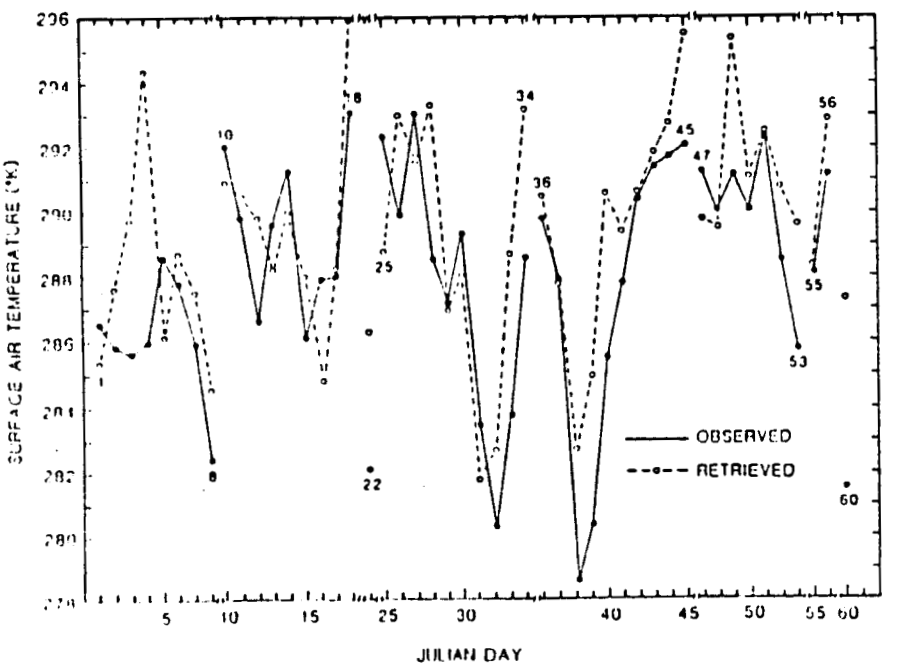


Fig. 2. Time series of observed and retrieved surface air temperatures from Julian days 1 - 60, 1984 at buoy 41001 (34.9 N., 72.9 W.). Numbers on plot indicate Julian day.

ORIGINAL PAGE IS
OF POOR QUALITY

The cloud classification scheme is described in Garand's thesis, and a manuscript that describes the technique in a somewhat abridged form has been submitted for publication in J.C.A.M. (Enclosure 2). Tapes containing the program have been provided to Dr. Man Li Wu at the Goddard Space Flight Center. Ms. Cindy Dixon, one of our graduate students is planning to join Dr. Wu this summer to work on applications of computer pattern analysis to satellite imagery.

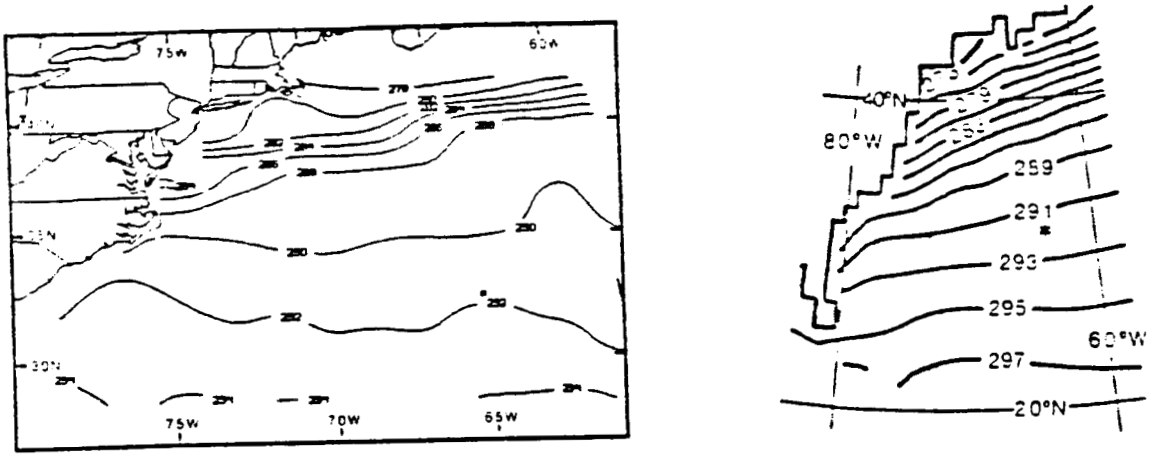


Fig. 3. Surface air temperature distributions retrieved from 11761 sample areas in GOES images during January and February 1984 and the thirty year climatology from Isemer and Hasse (1985).

A pattern analysis algorithm has also been developed to identify features of images of extra-tropical cyclones. This work comprised the M.Sc. thesis of Mr. Craig Burfeind. Burfeind was able to locate the fronts on images of cyclones in various stages of development. The results of that work are presented in Enclosure 3.

PROPOSED RESEARCH:

We will conduct a more detailed analysis of the data that yielded the results shown in the enclosed figures. Data from the CASP/GALE experiment will also be analyzed to provide additional validation of the image analysis algorithms. The results of those additional studies will be included in a description of our work that will be submitted to J.C.A.M.

The mechanisms that produce precipitation differ in cumulonimbus and in nimbostratus clouds. We therefore propose to utilize information on the location of precipitating regions, such as cold or warm frontal zones in extra-tropical cyclones, to adjust the rainfall retrievals. This aspect of our proposed effort will be based on Burfeind's research.

The availability of ground truth with which the algorithm can be adjusted has been a limitation to our past efforts. We used ship records of the existence of rain and NOAA operational radars in our previous studies. We are in the process of acquiring data from radars that have Computer Analyzed Plan Position Indicator, CAPPI, output. These radars are also regularly calibrated with dedicated rain gauges. Data from the FACE tropical rainfall experiment is also in hand. We propose to use that data to develop improved retrievals of rainfall from images obtained from the AVHRR and possibly from the Operational Line Scanner on the military DMSP. The latter imaging system measures reflected moonlight as well as sunlight so that the observation period is extended. It is my understanding that members of the Goddard staff are looking into the feasibility of operating sensors on TRMM and GOES-Next that measure nocturnal reflected visible light.

Reprinted from JOURNAL OF ATMOSPHERIC AND OCEANIC TECHNOLOGY, Vol. 2, No. 3, September 1985
American Meteorological Society

Determination of Rainfall Rates from GOES Satellite Images by a Pattern Recognition Technique

RONGZHANG WU, JAMES A. WEINMAN AND ROLAND T. CHIN

Determination of Rainfall Rates from GOES Satellite Images by a Pattern Recognition Technique

RONGZHANG WU,*† JAMES A. WEINMAN* AND ROLAND T. CHIN**

University of Wisconsin, Madison, WI 53706

(Manuscript received 11 June 1984, in final form 3 January 1985)

ABSTRACT

Radiances from clouds observed in visible and infrared images obtained from the SMS-2, GOES-2, and GOES-4 satellites have been used to estimate rainfall by means of a pattern recognition algorithm that was applied to single images. The algorithm classified rain into three classes: 0—no rain ($0 \leq R < 0.5$ mm h^{-1}); 1—light rain ($0.5 \leq R < 5.0$ mm h^{-1}); and 2—heavy rain (5.0 mm h$^{-1} \leq R$). The rainfall rates used in the training set and those used to test the algorithm were derived from a set of twenty-nine Plan Position Indicator (PPI) displays obtained from NOAA operational radars. Data were derived from summer storms, tropical storms and cyclones.

Rainfall from precipitating clouds was classified by a pattern recognition technique that used textural and radiance features in a hierarchic decision tree. The analysis was applied to regions 20 × 20 km in area that were measured in the visible spectral region with 1 × 1 km and 2 × 2 km resolution and in the infrared with 4 × 8 km resolution. The radiance features used in this analysis were the radiance maxima, minima, and the means. The textural features that were used included the edge strengths per unit area and the maxima and means of the mean, contrast, angular second moment, and entropy in four directions.

Of the areas sampled in this study, approximately one-third were in class 0, one-half were in class 1 and one-sixth were in class 2. Case studies that employed data from both the visible and infrared sensors correctly identified rainfall classes 0 and (1 + 2) in about 90% of the cases and identification into classes 1 and 2 was correct in about 70% of the cases studied. The corresponding skill scores were ~80 and 60% respectively. Data derived only from infrared images yielded correct identification of 0 and (1 + 2) classes in 85% of the cases and identification of classes 0, 1 and 2 was correct in 65% of the cases. The corresponding skill scores were ~65% and 40% respectively.

1. Introduction

The latent heat released by precipitation affects the heat budget of the atmosphere. Rainfall measurements are thus useful input to models of the earth's climate. Latent heat is also the main source of energy of hurricanes (see Anthes, 1982). Adler and Rodgers (1977) used satellite-borne microwave radiometry to measure the latent heat released in hurricanes at large distances from shore based radars. That energy was directly related to the wind speed measurement in the hurricanes. Such considerations have motivated studies on the measurement of precipitation from space. A recent NASA workshop addressed itself to various methods that employed microwave, infrared and visible satellite imagery (see Atlas and Thiele, 1981).

Microwave radiances respond directly to hydrometeors; however, microwave data are available at twelve-hour intervals at best. While rainfall distributions are not uniquely related to the appearance of clouds seen in visible and infrared imagery, rainfall estimates can be derived more frequently from operational geostationary and sun synchronously orbiting meteorological satellites. Combining space borne measurements of precipitation that employ both methods could thus improve the temporal resolution of rainfall rate distributions as well as the accuracy of such determinations.

Cloud observations in visible and infrared images obtained from satellites have been used to estimate rainfall rates over remote areas. The most widely employed techniques described by Barrett and Martin (1981) and by Atlas and Thiele (1981) obtain rainfall rates from regressions against area or rates of areal growth of cold clouds. Techniques such as the ones developed by Griffith *et al.* (1978) require the analysis of sequential images which can be obtained from geostationary satellites. A somewhat different approach was developed by Follansbee and Oliver (1975); that technique relied upon subjective cloud type identification in sample areas, i.e., the recognition of various cloud patterns by an experienced meteorologist. All of these rainfall estimation procedures are time consum-

* Space Science and Engineering Center.

† Also affiliated with: Central Meteorological Bureau, Beijing, People's Republic of China.

** Department of Electrical and Computer Engineering.

© 1985 American Meteorological Society

ing and labor intensive because the meteorologist is obliged to exercise careful judgement.

Lovejoy and Austin (1979) developed a pattern recognition technique that estimated rainfall from visible and infrared GOES satellite images. Their technique analyzed the statistics of radiances in both images. More recently, Negri *et al.* (1984) developed a simplified and objective adaptation of the Griffith-Woodley technique, which avoids the need to trace the temporal development of precipitating clouds.

The present study developed a pattern recognition algorithm to derive rainfall rates from single visible and infrared images or infrared images only. The technique that we used was an outgrowth of the preliminary study of Lee and Chin (1983). This technique determines rainfall in 20×20 km grid elements on the basis of radiance and texture features. Radiance features are global measurements of the 20×20 km grid elements containing information about the overall characteristic of the radiances within the grid element. Texture features are measurements that concern the spatial distribution of the radiances. When the grid contains radiances that vary little, the dominant properties of that grid are the radiance feature. When the grid has a wide variety of radiances, the dominant property of that area is texture. The algorithm classifies rainfall into three classes that correspond to operational radar precipitation levels: 0—no rain ($0 \leqq R < 0.5$ mm h^{-1}); 1—light rain ($0.5 \leqq R < 5.0$ mm h^{-1}); and 2—heavy rain (5.0 mm h$^{-1} \leqq R$). The rainfall rates used in the training sets for the development of the algorithm and those used to test the algorithm were derived from a set of twenty nine plan position indicator (PPI) displays obtained from NOAA operational radars. A training set contains two subsets: 1) the set of images that characterizes typical cloud/rain patterns and 2) a corresponding set of ground truth to identify patterns observed in the first subset. The training set is used to estimate the conditional probability distributions of the features extracted from 1), from which the decision rule (the rule for the identification of the various classes) is constructed. Data were obtained from summer storms, tropical storms and cyclones in the Gulf of Mexico coastal region and near south Florida.

2. Data sets

a. Satellite data

Data were obtained from the geostationary satellites GOES-2 during the summer of 1978, SMS-2 during the summer of 1979 and GOES-4 during the summer of 1983. The sensors on these satellites produced images in the visible spectrum, $0.55 < \lambda < 0.70$ μm, and in the thermal infrared, $10.5 < \lambda < 12.6$ μm. The spatial resolution of the visible sensors was either 1×1 km or 2×2 km while that of the infrared sensors was 4×8 km. The satellite data sources are summarized in Table 1. The infrared pixels were quantized into 256 grey levels that were calibrated in terms of brightness temperature. The images in the visible spectrum were quantized into 64 grey levels; these levels were multiplied by four to produce images that have a dynamic range that matches that in the infrared.

Before commencing the pattern recognition analysis, the visible and infrared images were navigated with respect to terrestrial landmarks so that the radar images could be collocated. Navigation problems were especially troublesome when correlations were sought between satellite and radar imagery of rapidly developing cells that were either at the edges of larger systems or were completely isolated. The existence of rain was indicated but no attempt was made to categorize the intensity of the rainfall in such cases.

Visible radiance levels were corrected to account for the effect of solar zenith angle on the illumination of the clouds by means of the empirical relationship developed by Raschke and Bandeen (1968). The satellite data cited in Table 1 were acquired from different satellites over several years. The calibration of the visible sensors was known to have drifted (see Muench, 1981); accordingly, images of White Sands, New Mexico and bright clouds were used to calibrate the relative response of the visible channel. Conversion from digital counts to directional reflectivity was achieved by the calibration method described by Smith *et al.* (1981). The intrinsic reflectivities of White Sands and bright clouds are independent of time so that the variation in the apparent reflectivities could be determined. The relative radiance values in all of the images obtained from a given satellite were thus restored to an approximately consistent set of values.

Another source of errors was the lack of uniform response of all of the sensors that comprised the visible imaging system. This effect could introduce streakiness in the image that could produce errors in the texture features. This effect will be described in the next section. Most of the data in Table 1 were screened to minimize this effect over scenes of surfaces that were known to be uniform.

Detailed analyses of satellite imagery revealed that the best results were obtained if the training and test data sets were obtained from the same satellite system. The reason for the incompatibility of data acquired from different satellites was not readily apparent; however, there are ample archives of data from any given geostationary satellite so that we do not regard this as a significant problem.

The 20×20 km grid elements that were used in this analysis were selected to match the resolution of the 37 GHz channel of the Scanning Multifrequency Microwave Radiometer of Nimbus 7. The grid elements contained a sufficient number of independent measurements in the infrared images to be statistically useful (~ 13); the situation was better in the visible images where each grid element contained at least one hundred pixels.

TABLE 1. Summary of data sources.

Date	Julian day	Time (GMT)	Satellite	Resolution VIS	Resolution IR	Contrast VIS	Contrast IR	Weather system	Radar station
28 August 1978	240	1500	GOES-2	2 × 2	4 × 8	High	High	Tropical storm	GLS
		1930	GOES-2	2 × 2	4 × 8	High	High	Tropical storm	GLS
25 July 1979	206	1730*	SMS-2	2 × 2	4 × 8	Low	Med/low	Tropical storm	GLS
		1930	SMS-2	2 × 2	4 × 8	Low	Med/low	Tropical storm	GLS
		2100	SMS-2	2 × 2	4 × 8	Low	Med/low	Tropical storm	GLS
26 July 1979	207	1500	SMS-2	2 × 2	4 × 8	Low	Med/low	Tropical storm	GLS
		1700*[2]	SMS-2	2 × 2	4 × 8	Low	Med/low	Tropical storm	GLS
		1830*[3]	SMS-2	2 × 2	4 × 8	Low	Med/low	Tropical storm	GLS
3 September 1979	246	1500	SMS-2	2 × 2	4 × 8	Low	Low	Hurricane	DAB
		1645	SMS-2	2 × 2	4 × 8	Low	Low	Hurricane	DAB
		1800	SMS-2	2 × 2	4 × 8	Low	Low	Hurricane	DAB
		2030	SMS-2	2 × 2	4 × 8	Low	Low	Hurricane	DAB
		1930	SMS-2	1 × 1	4 × 8	Low	Low	Hurricane	DAB
10 July 1979	191	1800	SMS-2	1 × 1	4 × 8	Low	Low	Tropical storm	SIL
		2030	SMS-2	1 × 1	4 × 8	Low	Low	Tropical storm	SIL
11 July 1979	192	1900	SMS-2	1 × 1	4 × 8	High	High	Tropical storm	SIL
5 July 1979	186	1600*	SMS-2	1 × 1	4 × 8	High	High	Thunderstorms	GLS
		1700*[2]	SMS-2	1 × 1	4 × 8	High	High	Thunderstorms	GLS
		1800*†	SMS-2	1 × 1	4 × 8	High	High/med	Thunderstorm	GLS
		1900†	SMS-2	1 × 1	4 × 8	Low	Low	Thunderstorm	GLS
		1930	SMS-2	1 × 1	4 × 8	Low	Low	Thunderstorm	GLS
13 July 1979	194	1530	SMS-2	1 × 1	4 × 8	High	High	Thunderstorm	GLS
		1800	SMS-2	1 × 1	4 × 8	High	High	Thunderstorm	GLS
6 July 1979	187	1830	SMS-2	1 × 1	4 × 8	High	High	Thunderstorm	GLS
		1900	SMS-2	1 × 1	4 × 8	High	High	Thunderstorm	GLS
17 August 1983	229	1800	GOES-4	2 × 2	4 × 8	High	High	Hurricane	GLS
		1900	GOES-4	2 × 2	4 × 8	High	High	Hurricane	GLS
		2000	GOES-4	2 × 2	4 × 8	High	High	Hurricane	GLS
		2130	GOES-4	2 × 2	4 × 8	High	High	Hurricane	GLS

* Denotes training sets used to represent categories characterized by spatial resolution and visible textural contrast $k = [22]$. More than one training set was used where *[2] or *[3] are designated.

† Denotes where the infrared mean textural feature, $k = [8]$, restricts the numbers of infrared features.

b. *Radar data*

Rainfall rates were inferred from radar data that were obtained simultaneously with the satellite imagery (see Table 1). The radar data were obtained from National Weather Service WSR-57 units which have 10 cm wavelengths and a 230 km scan radius. Rainfall rates, R (mm h^{-1}), were computed from the measured radar reflectivities, Z (mm^6 m^{-3}), by the relationship $Z = 55R^{1.6}$; this relationship is in operational use for convective precipitation. Complete PPI scans were obtained in seven minutes, and these scans were obtained within five minutes of the corresponding satellite images. Microfilm images of PPI displays were projected on a transparent grid array with 20 × 20 km spacing. Outlines of rainfall rate contours were manually traced on the grid and the effects of ground clutter were also removed. The rainfall rate classes and coordinates of the grid were then digitized. If a grid element was partially filled by two rain classes, the grid element was assigned the value that occupied the greatest fractional area. Ambiguities could arise around the edges of larger storm systems where small precipitation cells were localized and evolving rapidly. Isolated cells also had to be carefully navigated so that their location was properly weighted among neighboring grid elements. The radar data could be displayed once it was digitized. The analysis of twenty nine PPI and corresponding satellite images was performed on the University of Wisconsin Man-computer Interactive Data Acquisition System (McIDAS); (see Suomi *et al.*, 1983).

3. Analysis

a. *The decision rule*

The maximum likelihood decision rule was used in this study to classify the three rain classes denoted as ω_0, ω_1, and ω_2. A feature vector $\bar{x} = (x_1, x_2, \cdots x_k)$, characterizing the rainfall information in a grid element, was classified as class ω_i if:

ORIGINAL PAGE IS
OF POOR QUALITY

ORIGINAL PAGE IS
OF POOR QUALITY

$$p(\bar{x}|\omega_i)P(\omega_i) > p(\bar{x}|\omega_j)P(\omega_j), \quad \text{for all} \quad j \neq i. \quad (1)$$

where $p(\bar{x}|\omega_i)$ is the conditional density function of $\bar{x}$, and $P(\omega_i)$ is the *a priori* probability of occurrence of rainfall class ω_i. In this study the probability of occurrence of all three rain classes were assumed to be the same. The conditional density functions $p(\bar{x}|\omega_i)$ $i = 0$, 1, and 2 were assumed to be normally distributed and their means and covariances are estimated from a set of training samples. The components of the pattern recognition process, as depicted in Fig. 1, are training and classification. The following problems were then addressed: 1) what features should be extracted from each grid element to give a good representation of the rainfall rates: and 2) how does one choose the proper training sets?

b. *Feature extraction*

We employed 24 features from each of the visible and the infrared images to determine the various rainfall classes: these radiance and textural features are summarized in Table 2. These features have been more comprehensively described by Weszka *et al.* (1976) and Parikh (1977).

The radiance features are statistical parameters derived from all of the pixels in each 20 × 20 km grid element. They include the maximum, minimum, and mean of the radiance grey levels.

One of the texture features that are used to determine radiance variations is the edge strength per unit area defined by the area averaged Roberts gradient

$$\overline{RG} = \frac{1}{(M-d)(N-d)} \sum_{m=1}^{M-d} \sum_{n=1}^{N-d} \{|I(m, n) - I(m+d, n+d)| + |I(m+d, n) - I(m, n+d)|\} \quad (2)$$

where $I(m, n)$ are the radiances at specified Cartesian coordinates m and n, and d is the number of pixels separating the $M \times N$ points. The Roberts gradients, $\overline{RG}$ are designated as k = [7] and [16] in Table 2.

Grey level difference statistics were additional texture features that were employed in this study. These quantities depend on the histograms of the distributions of radiance difference, $h_{\theta,d}(g)$. If pairs of pixels are considered within a 20 × 20 km grid element the grey level radiance difference is:

$$g = |I(m, n) - I(m + \hat{d}, n + \hat{d})|, \quad (3)$$

where both $\hat{d}$ and $\hat{d}$ can assume values of either 0 or $\pm d$: d is the distance separating the pixel pairs and θ = arc tan$(\hat{d}/\hat{d})$ = 0°, 45°, 90°, 135° is the direction in which the pixel pairs are measured. The grey difference g may assume values in the range 0, 1, · · · 255.

The histograms $h_{\theta,d}(g)$ of grey level radiance differences in a grid element provide a measure of the scale size of the cloud features. For example, if a grid element contains clouds whose horizontal dimensions are large and whose texture is smooth compared to the selected pixel separation d, then grey level differences $g \approx 0$ will be highly probable. On the other hand, if clouds

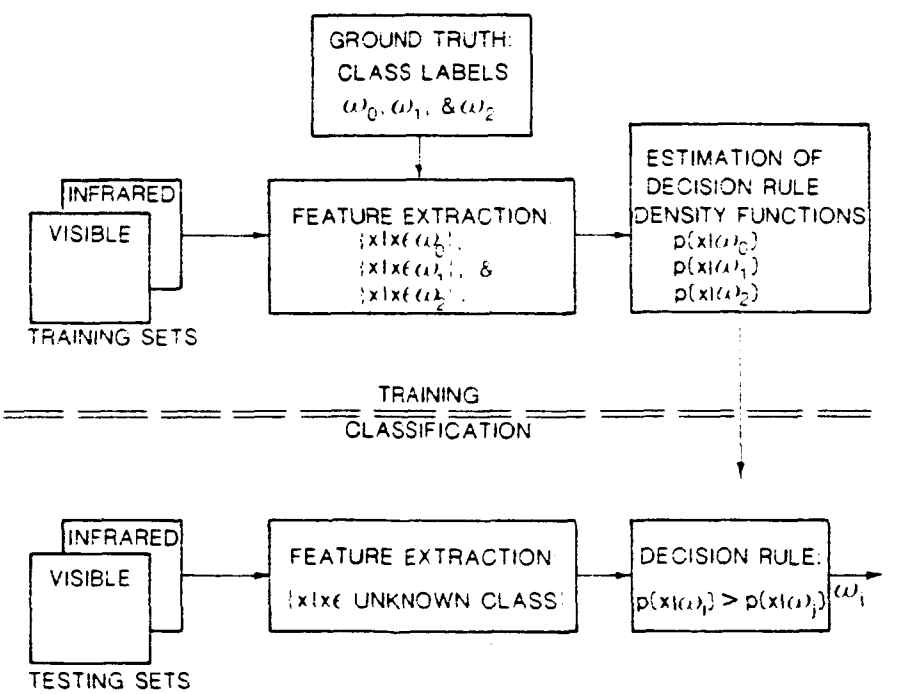


FIG. 1. Schematic diagram of the pattern recognition algorithm.

ORIGINAL PAGE IS
OF POOR QUALITY

TABLE 2. Features* used to characterize satellite images of clouds.

Feature number k	Features		Pixel separation d VIS	IR
	Radiance			
[1]	Mean grey level			
[2]	Standard deviation of grey level			
[3]	Maximum grey level			
[4]	Minimum grey level			
[5]	Maximum/minimum grey level ratio			
[6]	Grey level range			
	Texture			
[7]	Edge strength per unit area	$\overline{RG}$[7]	2	4
[8]-[11]	Maximum within 4 directions	MEAN[8], CON[9], ASM[10], ENT[11]	2	4
[12]-[15]	Mean of 4 directions	MEAN[12], CON[13], ASM[14], ENT[15]	2	4
[16]	Edge strength per unit area	$\overline{RG}$[16]	4	8
[17]-[20]	Maximum within 4 directions	MEAN[17], CON[18], ASM[19], ENT[20]	4	8
[21]-[24]	Mean of 4 directions	MEAN[21], CON[22], ASM[23], ENT[24]	4	8

* A total of 24 features were considered for infrared images only and 48 features were considered for infrared and visible images.

are small or if they are inhomogeneous in appearance compared to the pixel separation, then a larger range of g is more probable in a given grid element. The histograms $h_{\theta,d}(g)$ will thus be spread over a larger range of g as graininess or streakiness increase. Note that the texture may be streaky in a particular direction so that the histogram must be specified as a function of angle θ as well as d.

Four features that characterize the shape of $h_{\theta,d}(g)$ are calculated:

Mean:

$$\mathrm{MEAN}(\theta, d) = \frac{1}{256}\sum_{g=0}^{255} g\left[\frac{h_{\theta,d}(g)}{N}\right]. \quad (4)$$

Contrast:

$$\mathrm{CON}(\theta, d) = \sum_{g=0}^{255} g^2\left[\frac{h_{\theta,d}(g)}{N}\right]. \quad (5)$$

Angular second moment:

$$\mathrm{ASM}(\theta, d) = \sum_{g=0}^{255}\left[\frac{h_{\theta,d}(g)}{N}\right]^2. \quad (6)$$

Entropy:

$$\mathrm{ENT}(\theta, d) = -\sum_{g=0}^{255}\frac{h_{\theta,d}(g)}{N}\ln\left[\frac{h_{\theta,d}(g)}{N}\right]. \quad (7)$$

where N is the total number of pixel pairs in the grid element separated by distance d and direction θ.

The MEAN is the average of the grey level radiance differences. Contrast, CON, is a measure of the local variation of radiances in a grid element. Large values of MEAN and CON in a given direction correspond to markedly structured clouds such as cumulus with shadows. The maximum directional MEAN and CON are designated as k = [8], [17] and k = [9], [18], respectively, in Table 2. The mean of these quantities averaged over four directions are designated as k = [12], [21] and k = [13], [22] in Table 2.

The angular second moment, ASM, is a measure of the homogeneity of grey level differences over distances, d, and angles θ. A large ASM implies that although neighboring pixels may have different grey levels, the differences in these levels at neighboring pixels are similar over many pairs of pixels in the grid element. It is high for cirrus or cumulonimbus anvils, for decks of stratus, and for bands of clouds oriented in the direction of θ. The ASM can depend on angle if the clouds are banded in a dominant direction. The maximum ASM in a given direction are designated as features k = [10] and [19] and the mean ASM over all directions are designated as k = [14] and [23] in Table 2.

Entropy, ENT, is a measure of the absence of a distinct scale of organization. It is a feature that is a maximum when all radiance differences g have an equal probability of occurring. The ENT is low when the texture is smooth and when it is highly structured. This dual valued dependence on $h_{\theta,d}(g)$ arises because ENT is small when $h_{\theta,d}(g) \approx 0$ and ≈ 1. The latter effect is contributed by the logarithmic contribution to ENT. Again ENT depends on direction for features k = [11] and [20] and it can be averaged over all directions in features k = [15] and [24].

The corrected visible and infrared images or the infrared images alone were processed on McIDAS. A pre-processing step rejected clear grid elements in the visible images that had maximum grey level intensities < 80. The 20×20 km grid elements containing clouds roughly in the same stage were identified on the basis of values of the textural contrast feature k = [22].

ORIGINAL PAGE IS
OF POOR QUALITY

c. Feature selection criteria

The radiance and texture features can be regarded as components of a vector $\bar{x} = (x_1, x_2, x_3, \cdots x_k)$ that describes each 20 × 20 km grid element. The feature vectors of the grid elements that comprise a given rainfall class in each scene can be described by a mean vector $\bar{\mu} = (\mu_1, \mu_2, \mu_3, \ldots, \mu_k)$ and a variance vector $\bar{\sigma}^2 = (\sigma_1^2, \sigma_2^2, \sigma_3^2, \cdots \sigma_k^2)$, assuming that $\bar{x}$ is normally distributed and that all features are independent of each other.

Because these vectors can in principle have as many as 48 components, not all of which contribute to the separation of rainfall classes, the number of features had to be reduced. This was achieved by a feature selection procedure which ranked the features in the order of their ability to separate the rainfall rate classes. This was implemented by a divergence that normalized the separation of the means of the feature by the sum of the variances. The divergence, for the feature x_k between rainfall rate categories i and i' is:

$$D(i, i') = \frac{|\mu_k(i) - \mu_k(i')|}{\sigma_k(i) + \sigma_k(i')}, \quad i, i' = 0, 1, \text{ and } 2; \quad i \neq i'. \tag{8}$$

Divergences were computed during the training phase for all pairs of rainfall rate classes. Those features for which the divergences ranked highest were chosen to discriminate between the various rainfall rate classes in the classification phase (see Swain and Davis, 1982).

Table 3 presents a summary of the number of scenes in which various features were ranked in the order of decreasing divergence for separating classes 0 and (1 + 2), i.e., rank 1 was the most effective discriminating feature while rank 9 was the least. Thus we find that for the separation of rain and no rain, visible feature [1] ranked foremost in eight scenes, visible feature [3] ranked foremost in nine scenes, visible feature [14] ranked foremost in eight scenes, etc. Similarly, infrared feature [3] ranked first in 11 scenes, etc.

The visible radiance features k = [1], [3] and [4] were frequently significant discriminating features; however, texture features k = [11], [14] and [15] were also frequently significant discriminating features. While these texture features affected the appearance of precipitating clouds, they have only been recognized subjectively in previous studies as mentioned in the introduction. Texture features defined over large pixel separations, d = 4, appeared to be weakly related to rainfall. This is consistent with the findings of Yau and Rogers (1984), which suggest that most precipitating cells are smaller than ~10 km.

The infrared radiance features k = [1], [3] and [4] were frequently significant in identifying precipitating regions, [i.e., those designated (1 + 2)]. However, texture features k = [10], [12] and [15] were also significant. Here too, the texture features that were defined in terms of the smallest pixel separation were the most important.

Separating rainfall classes 1 and 2 was most frequently achieved with features [1], [3] and [4] in the visible and in the infrared images. No texture features were consistently able to contribute to this preliminary separation. Accordingly, the classification was conducted in two steps: the no-rain and rain separation 0, and (1 + 2), used features that differed from those used to subsequently separate between classes 1 and 2.

d. Feature properties and training sets

The visible and infrared contrast features [22] are shown in Fig. 2 as functions of time. The points represent each class mean of these features for rainfall classes 0, 1 and 2. These two figures show that the feature values changed with time and varied with storm systems. No simple threshold could be found to separate each class for all cases. These figures show that clouds in different stages of convective activity had different feature values. For example, on day 186 of 1979 at 1600 GMT, clouds were in a growth stage and at 1900 GMT Fig. 2a shows that the clouds were in a decay stage. This implied that the separation of rainfall classes should be performed by taking different convective activity stages into account.

The contrast is a measure of convective activity so that this feature should be correlated in the visible and infrared channels. Moreover, large values of visible contrast indicate that small scale convective activity is strong as in the early stages of cumulus growth. As the cumulus clouds mature, anvils and cirrus shields exhibit lower contrast. Contrast, rather than infrared brightness temperature, was selected as an initial screening feature because some tropical storms only grow to modest altitudes so that radiance features which depend on brightness temperature could miss such clouds. For example, the active thunderstorm shown in Fig. 2a has greater contrast than the stable tropical storm shown in Fig. 2d. As a result, feature [22] was used to divide training sets into three classes, i.e., high, medium and low contrast [22].

A visible contrast that was appreciably greater than the infrared contrast was attributed to streakiness in the visible image. The subsequent analysis of such an image would only consider the visible features k = [1], [3], [4], [5], and [6] and all of the relevant infrared features. An example of such a case is shown in Fig. 2c where the high visible contrast, CON[22] > 150, is clearly inconsistent with the intermediate infrared contrast. This figure can be compared to Fig. 2b in which visible and infrared contrasts are similar in magnitude.

It was generally preferable to utilize the visible contrast after its verisimilitude was determined because the spatial resolution of the visible channels was greater

ORIGINAL PAGE IS
OF POOR QUALITY

TABLE 3. Number of images in which pattern recognition feature [k] were ranked between 1 and 9 for rainfall classification (0). no rain. and (1 + 2). rain.

Radiance features	Pixel separation	k	Rank 1	2	3	4	5	6	7	8	9
			Visible								
Mean Grey Level		[1]	8	8		3		1	2	1	1
Max. Grey Level		[3]	9	5	2	1	3	1	1	1	1
Min. Grey Level		[4]		1	7	1	3	4	1	1	1
Texture features	**Pixel separation**										
$\overline{RG}$	2	[7]					3	2	1	2	4
Max. MEAN	2	[8]			1	4		3	3	3	3
Max. ASM	2	[10]					1				2
Max. ENT	2	[11]	1	2	9	4	3	5	2		
Mean. MEAN	2	[12]	1			1	5	1	6	1	3
Mean. CON	2	[13]							1	1	2
Mean. ASM	2	[14]	8	4	5	3	2	1	1	1	
Mean. ENT	2	[15]		7	3	7	4	2	1	1	
$\overline{RG}$	4	[16]					1				
Max. ASM	4	[19]				1	2	3	1	2	2
Max. ENT	4	[20]								4	
Mean. MEAN	4	[21]									1
Mean. ASM	4	[23]						3	4	4	4
Mean. ENT	4	[24]			2			1	3		3
			Infrared								
Radiance features											
Mean Grey Level		[1]		8	2			1	2	2	2
Std. Deviation		[2]				1					
Max. Grey Level		[3]	11		1	1		3	1	2	
Min. Grey Level		[4]	2		7	2		1	3	1	1
Max./Min Ratio		[5]					1		1		
Grey Level Range		[6]		1			1				
Textural features	**Pixel separation**										
$\overline{RG}$	4	[7]		3	1	2	3		3	2	3
Max. MEAN	4	[8]			2	2	1	3		1	1
Max. CON	4	[9]							1	2	1
Max. ASM	4	[10]	7	5	4	8					
Max. ENT	4	[11]				1	2				1
Mean. MEAN	4	[12]	3	3	4		2	1	4	2	
Mean. CON	4	[13]					1	2	1	1	
Mean. ASM	4	[14]	2	2	2	3	5	5	1		1
Mean. ENT	4	[15]	2	5	2		7	2		3	
$\overline{RG}$	8	[16]			2						
Max. MEAN	8	[17]				1		1	2		
Max. CON	8	[18]						1			1
Max. ASM	8	[19]				3	1	1	1	1	1
Max. ENT	8	[20]						1	1		1
Mean. MEAN	8	[21]						1		1	
Mean. CON	8	[22]								1	1
Mean. ASM	8	[23]						1	2	1	2
Mean. ENT	8	[24]				2	2	2	1	2	3

than the resolution of the infrared images and the classification divergence was greater (see Section 3c).

The different resolution of the visible image affects some feature values. For example. on day 186. all images have a resolution of 1 × 1 km. whereas on day 246 of 1979. the resolution was 1 × 1 km at 1930

ORIGINAL PAGE IS
OF POOR QUALITY

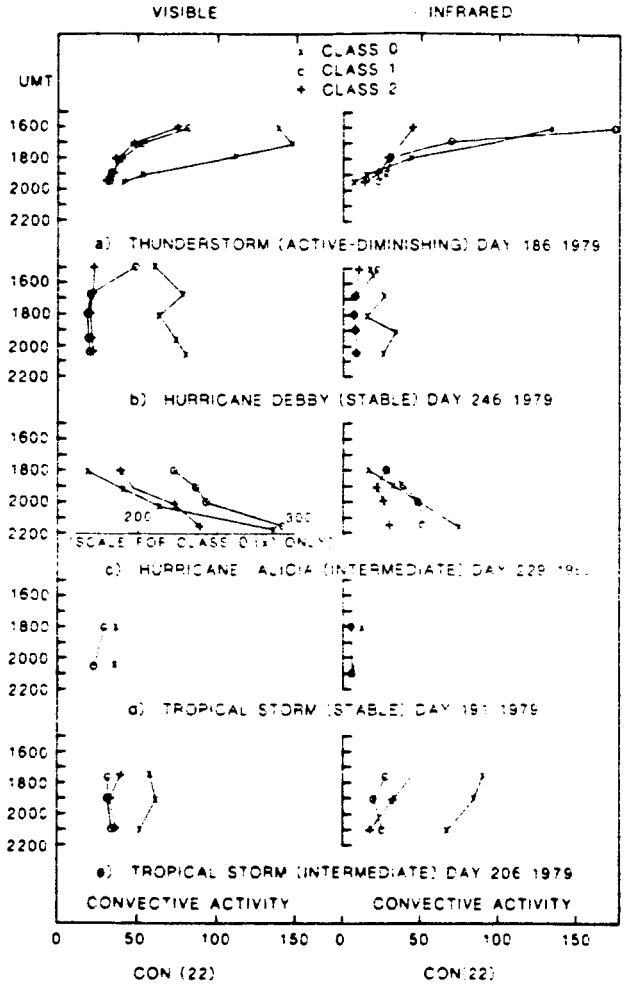


FIG. 2. The mean of the distribution of the contrast texture feature [22] in 20 × 20 km grid elements in visible and infrared images of the indicated precipitating systems. Panel (c) shows an example of the effect of streakiness in the visible image. Data are presented as a function of time to show the evolution of these texture features.

GMT and 2 × 2 km for others. The visible feature [14] was much bigger for images with 1 × 1 km resolution than those with 2 × 2 km resolution. This implies that the training sets and the test sets should be taken at the same resolution.

A detailed inspection of the features displayed in Fig. 2 shows that the contrast category varied significantly. Usually more than two training sets were selected to represent low, medium and high contrast categories for both 1 × 1 km and 2 × 2 km resolution, so that the test sets could be applied to a proper training set. Unfortunately, there were not enough scenes to permit that for all of the events. The training sets are designated by an asterisk in Table 1. If more than one training set was considered for a given contrast category, those training sets are designated by an asterisk with subscript N in Table 1. The schematic idea of the different types of training sets is shown in Fig. 3a.

e. *Decision tree*

The decision tree shown schematically in Fig. 3b was used to separate the rainfall classes. It is described as follows:

The analysis of an image commenced by checking the visible contrast and the resolution of the test set to decide which contrast category applies to the test set. The visible or infrared mean intensity grey level k = [1] was then used to determine which training set should be chosen inside the given contrast category. The visible mean intensity grey level was preferable to the corresponding infrared feature provided that visible data were available. The decision rule determined by the chosen training set was then used to discriminate between the no rain, 0, and the rain, (1 + 2) classes. In the cases tested, the separation was achieved with visible features [1], [3], [4], [14], [15], [19], [23] and [24] and with infrared features [1], [3], [4], [10], [14], and [15] (see Table 3). It was noted that the infrared mean texture feature k = [8] was highly variable as storms developed. If this texture feature was markedly different from the infrared mean texture feature of all of the training sets, then only the infrared intensity features k = [1], [3], and [4] and all of the visible features were used to discriminate between rain and no

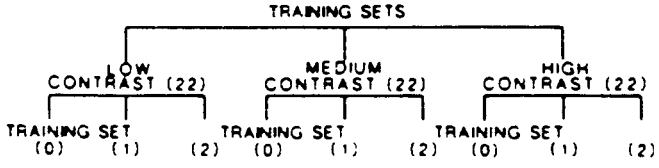


FIGURE 3a DIFFERENT TYPES OF TRAINING SETS

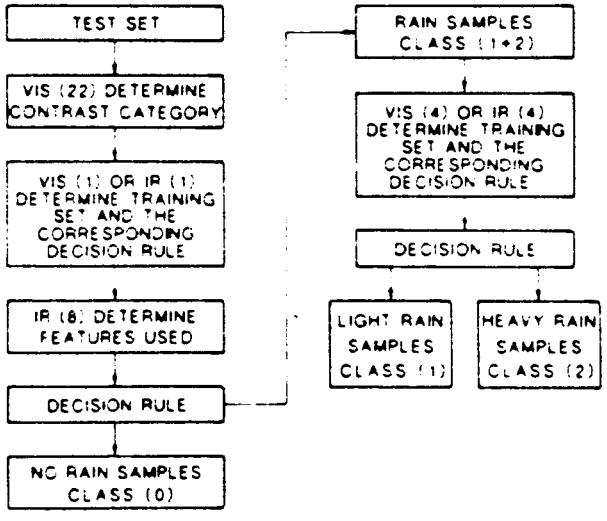


FIGURE 3b DECISION TREE

FIG. 3. (a) Concept of training sets; (b) rainfall classification decision tree.

ORIGINAL PAGE IS
OF POOR QUALITY

TABLE 4. Effect of radiance and texture features on classification of grid elements [No rain (0), rain (1 + 2)].

Features used for separation*	Class statistics		
	Vis:[1]; IR:[1]	Vis:[1], [3], [4]; IR:[1], [3], [4]	Vis:[1], [3], [4], [14], [15], [19], [23], [24] IR:[1], [3], [4], [10], [14], [15]
Resolution (km)**		*Bias*** [no rain (0), rain (1 + 2)]	
1 × 1	1.04 ± 0.07	1.03 ± 0.07	1.00 ± 0.02
2 × 2	0.84 ± 0.14	0.89 ± 0.13	0.96 ± 0.05
		*Correct classification*** [%]	
1 × 1	81 ± 1	84 ± 1	94 ± 1
2 × 2	80 ± 5	78 ± 5	92 ± 3
		*Skill score*** [%]	
1 × 1	50 ± 13	58 ± 8	85 ± 2
2 × 2	60 ± 10	54 ± 9	81 ± 4

* Category vis. contrast. CON[22]:Low.
** No. of image pairs (1 × 1) km resolution:3.
No. of image pairs (2 × 2) km resolution:4.
*** Panofsky and Brier (1968).

rain classes. Otherwise, all of the features were used. The reason for this decision is that the infrared large-scale texture features vary greatly as clouds develop; however, that variation appears to bear little direct relationship to rainfall. The cases where this criterion was invoked are designated by a plus in Table 1.

After determining that each grid element was either in the "nonraining" (0) or the "raining" (1 + 2) classes, those grid elements in which rain was falling were subsequently divided into classes 1 or 2. The features used for this second classification were the visible and infrared radiance mean, maximum and minimum grey levels, k = [1], [3] and [4]. The feature [4] for visible or infrared was used to decide which training set should be used.

This pattern recognition algorithm was performed on a Harris-800 computer. The computer time required to analyze one test set was about two minutes.

4. Rainfall classification results

The effect of different features on the ability to separate the various classes was first investigated. Table 4 shows the separation between the rainfall classes, "rain" (1 + 2), and "no rain" (0), obtained by applying the pattern recognition algorithm to visible and infrared images using different features. The features that were used to separate classes 0 and (1 + 2) are shown. This table illustrates the relative importance of radiance and texture features. Note that the first two columns summarize results obtained when only radiance features such as the mean [1], the maximum [3] and minimum [4] radiance grey levels were considered. The third column shows the effect of including numerous additional texture features in the analysis. The performance of the rainfall retrieval algorithm is evaluated by tabulations of the bias, the percentage of correctly classified grid elements and the skill score percentage (see Panofsky and Brier, 1968).

It is noteworthy that the addition of eight texture features in the analysis improves the skill score by more

TABLE 5. Summary of rainfall classification from infrared images only.*

Rainfall rate classification	Class Statistics	
	0 & (1 + 2)**	0, 1 & 2***
I.R. Contrast [22]	*Bias*† [no rain (0), rain (1 + 2)]	
Low††	1.00 ± 0.14	
High†††	1.07 ± 0.12	
	Correct classification† [%]	
Low	86 ± 6	64 ± 3
High	85 ± 3	64 ± 10
	Skill score† [%]	
Low	67 ± 10	44 ± 4
High	66 ± 8	43 ± 13

* Panofsky and Brier (1968).
** I.R. features k = [1], [3], [4], [7], [8], [10], [11], [12], [14], [15] were used to separate rain or no rain classes.
*** I.R. features k = [1], [3], [4] were then used to divide the rain class (1 + 2) into classes 1 or 2.
† I.R. resolution: 4 × 8 km.
†† No. of images: 11.
††† No. of images: 9.

ORIGINAL PAGE IS
OF POOR QUALITY

than 27 percentage points. In as much as most previously used rainfall estimation algorithms depended only on variations of radiance features, it is encouraging to pursue the use of textural information in this analysis. There is also an indication that visible images with 1×1 km resolution provide somewhat better estimates of the occurrance of rain than the visible images with 2×2 km resolution.

Table 5 presents the classification of rainfall classes 0 and (1 + 2) in the left-hand column and 0, 1, and 2 in the right-hand column. This analysis was conducted with infrared data only; it therefore simulates the ability of the present algorithm to classify rainfall rates from GOES data at night. The contrast texture feature [22] does not appear to affect the skill score. The skill score for classification between no rain grid elements in class 0 and those with rain in (1 + 2) is 67%; this compares somewhat unfavorably with the skill score of 85% obtained from visible and infrared data shown in the most right-hand column of Table 4. It should be noted that the 4×8 km resolution of the infrared sensor only reveals large scale convection while the visible sensor can detect smaller scale convective activity. The classification between rainfall classes 1 and 2 is obtained with radiance features [1], [3] and [4] and the skill score for separation into three rainfall rate classes diminishes to 44%. It is encouraging that no obvious bias is evident in this classification scheme.

Table 6 presents the classification of rainfall classes 0 and (1 + 2) in the left column and into classes 0, 1 and 2 in the right column when both visible and infrared images are analyzed. The contrast texture feature [22] appears to affect the skill score slightly; the low contrast cases appear to have skill scores about 5% higher than the high contrast cases. However, the visible images with 1×1 km resolution appear to provide consistently higher skill scores than those with the lower resolution. The classification into classes 0, 1 and 2 is achieved with a skill score of 65% which is better than the 44% skill score that was provided by the infrared data only. No obvious bias is evident in this data.

The ability of the algorithm to provide objective displays of rainfall distributions is shown in Figs. 4, 5 and 6. These figures show results obtained from thunderstorms, a tropical storm and a hurricane, respectively. Figures 4, 5 and 6a, b show the visible and infrared images from which the rainfall estimates were derived. Figures 4, 5 and 6c, d show the rainfall distributions derived from the present algorithm and those indicated by the NOAA radars respectively. The grey scale coding in Fig. 6c, d is white = no data, light grey = 0, grey = 1, dark grey = 1 or 2, and black = 2; the cross in-

TABLE 6. Summary of rainfall classification from visible and infrared images.

			Class statistics	
	Rainfall rate class		0 & (1 + 2)**	0, 1 & 2***
Number of Image pairs	Visibility Contrast, CON[22]	Resolution (km)	*Bias** [no rain/(0, rain/(1 + 2)]	
5	High	VIS: 1×1 I.R.: 4×8	1.00 ± 0.14	
3	High	VIS: 2×2 I.R.: 4×8	1.00 ± 0.11	
4	Low	VIS: 1×1 I.R.: 4×8	1.00 ± 0.02	
8	Low	VIS: 2×2 I.R.: 4×8	0.96 ± 0.04	
			*Correct classification** [%]	
	High	VIS: 1×1 I.R.: 4×8	91 ± 3	81 ± 9
	High	VIS: 2×2 I.R.: 4×8	90 ± 3	66 ± 1
	Low	VIS: 1×1 I.R.: 4×8	94 ± 1	76 ± 3
	Low	VIS: 2×2 I.R.: 4×8	92 ± 3	73 ± 4
			*Skill score** [%]	
	High	VIS: 1×1 I.R.: 4×8	82 ± 5	70 ± 12
	High	VIS: 2×2 I.R.: 4×8	74 ± 4	48 ± 1
	Low	VIS: 1×1 I.R.: 4×8	85 ± 2	61 ± 4
	Low	VIS: 2×2 I.R.: 4×8	80 ± 8	58 ± 7

* Panofsky and Brier (1968).

** Separation into rainfall class "no rain", (0), or "rain", (1 + 2), for high contrast cases were achieved with VIS k = [1], [3], [4], [7], [8], [10], [11], [12], [14], [15], [19], [23], [24] and I.R. k = [1], [3], [4], [10], [14], [15].

Separation into rainfall class "no rain", (0), or "rain", (1 + 2), for low contrast cases was achieved with VIS k = [1], [3], [4], [14], [15], [19], [23], [24] and I.R. k = [1], [3], [4], [10], [14], [15].

*** Subsequent separation of "rain" into classes (1) or (2) was achieved with VIS k = [1], [3], [4], and I.R. k = [1], [3], [4].

ORIGINAL PAGE IS
OF POOR QUALITY

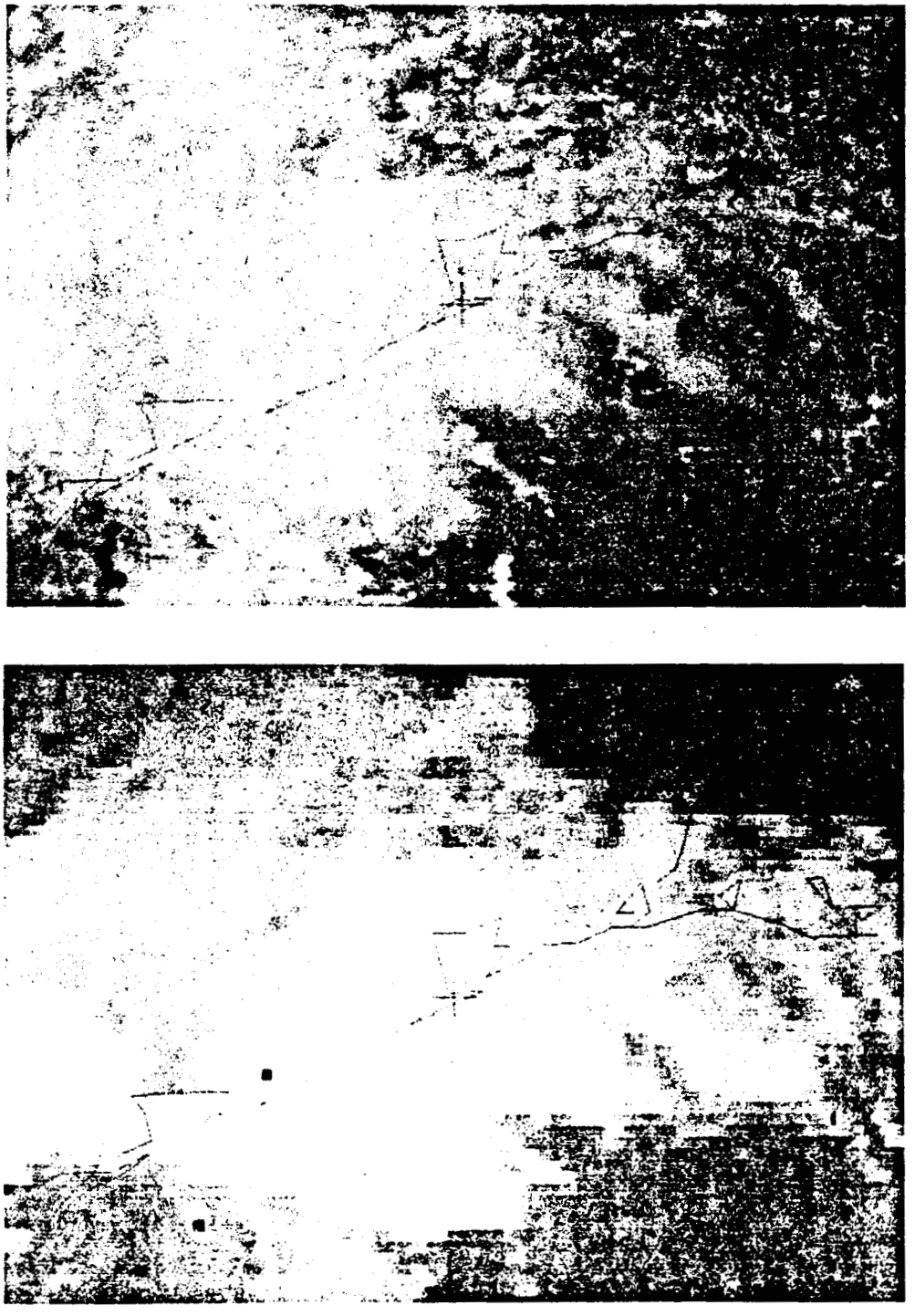


FIG. 4. (a) Visible image obtained from the SMS-2 satellite on 5 July 1979 at 1700 GMT which shows thunderstorms near Galveston, TX. (b) As in 4(a) except that the infrared image is shown.

dicates the location of radar and the dashed lines delineate the coasts. While the details of the rain distributions differ in the latter two figures, the broad features are similar. It may in fact be argued that the elevation angle of the radar introduces a bias against heavy rain observations at large distances from the radar. For example, the satellite image (Fig. 5a) suggests that the center of the tropical storm was more than 100 km southwest of the Galveston radar. The satellite derived rains are indicated as class 2 to the southwest of the

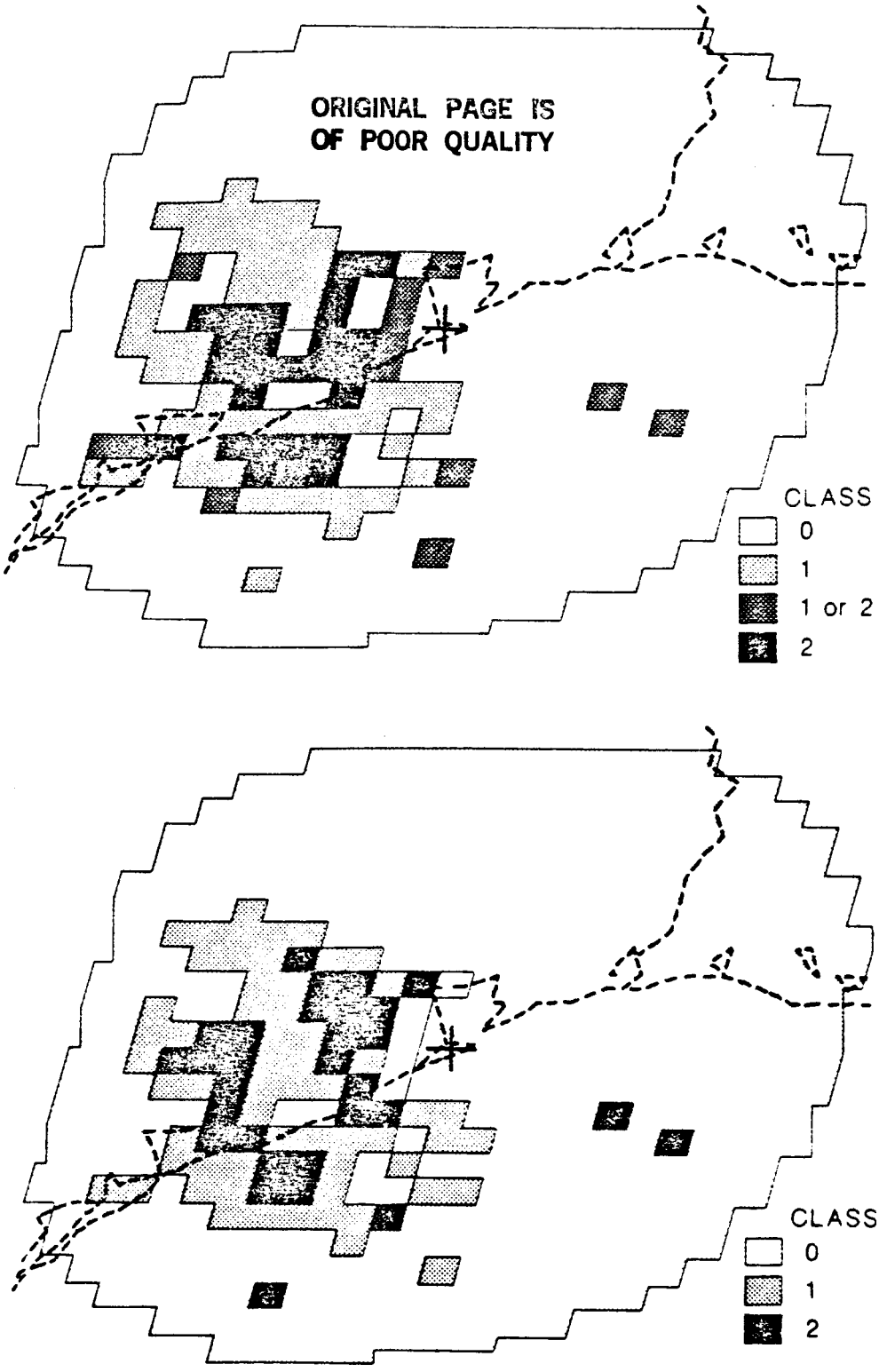


FIG. 4. (c) Derived rainfall category distribution: white = no data, light grey = 0, grey = 1 and black = 2; dark grey = 1 or 2. (d) Radar image obtained from the Galveston radar. The grey scale is the same as for 4(c).

ORIGINAL PAGE IS
OF POOR QUALITY

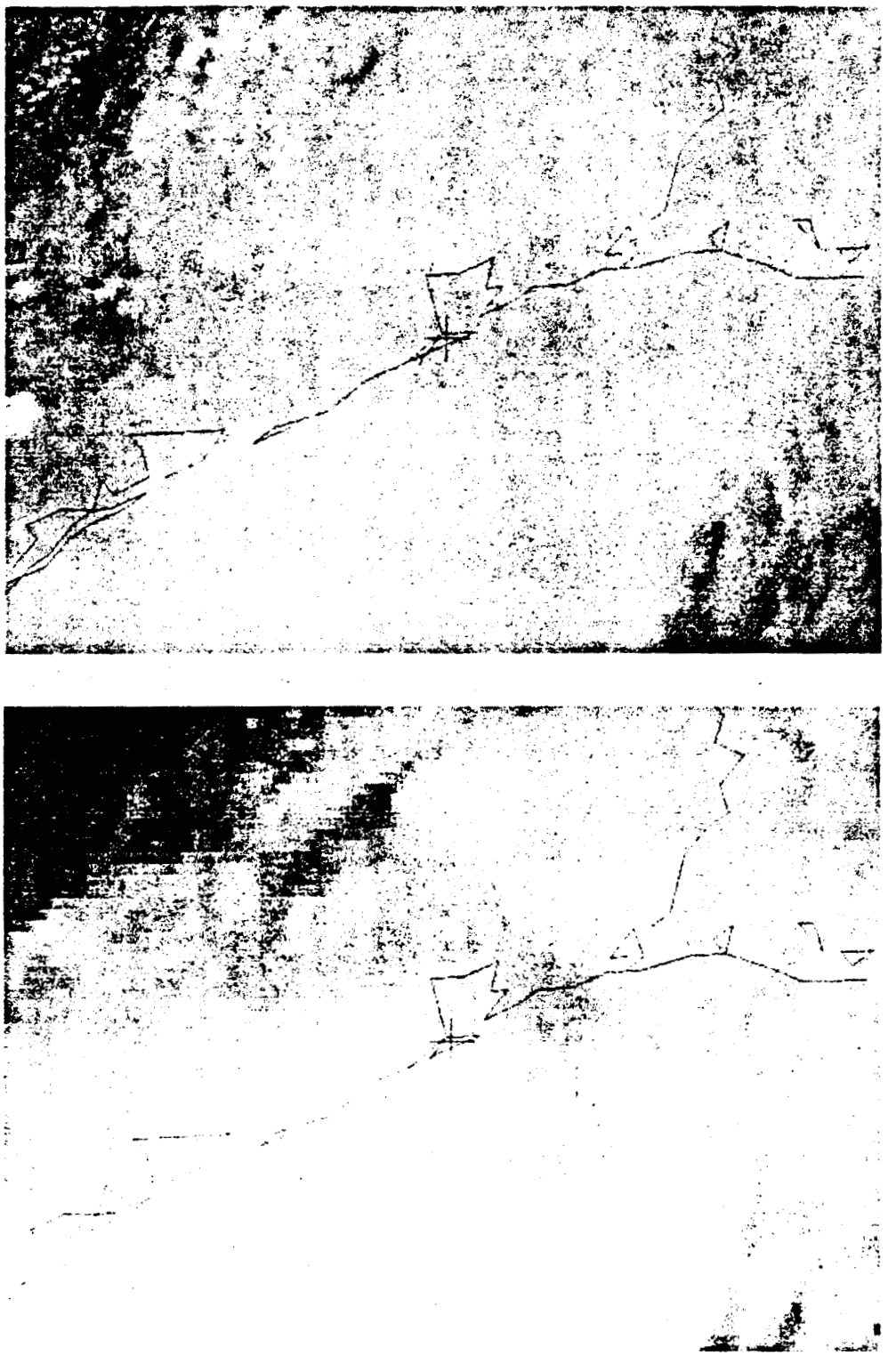


FIG. 5. (a) Visible image obtained from the SMS-2 satellite on 25 July 1979 at 1930 GMT which shows a tropical storm near Galveston, TX. (b) As in 5(a) except that the infrared image is shown.

radar while the radar designates them as class 1. A similar effect is evident in Fig. 6c, d where the eye of Hurricane Debbie is to the south of Daytona Beach yet the radar suggests that the rainfall diminishes to class 0 at the bottom of Fig. 6d.

Discrepancies occur most frequently at the edges of

ORIGINAL PAGE IS
OF POOR QUALITY

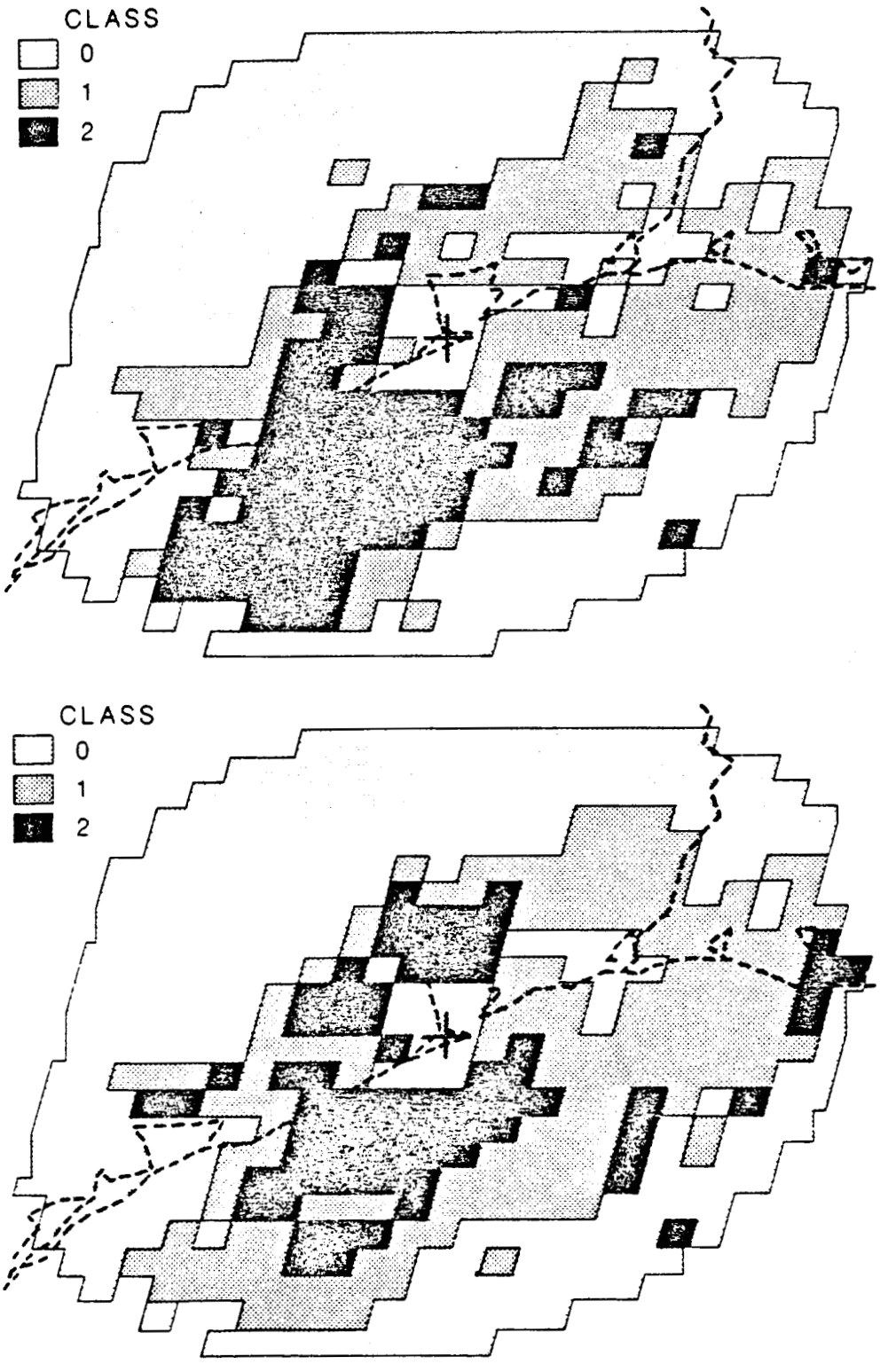


FIG. 5. (c) Derived rainfall category distribution: white = no data, light grey = 0, grey = 1 and black = 2. (d) Radar image obtained from the Galveston radar. The grey scale is the same as for 5(c).

the larger precipitating systems and near isolated cells, where ambiguities in assigning radar-derived rainfall rates to grid elements were the greatest because of navigation problems. It was only possible to indicate that rain was falling on some isolated or edge grid elements because no training sets that adequately discriminated

ORIGINAL PAGE IS
OF POOR QUALITY

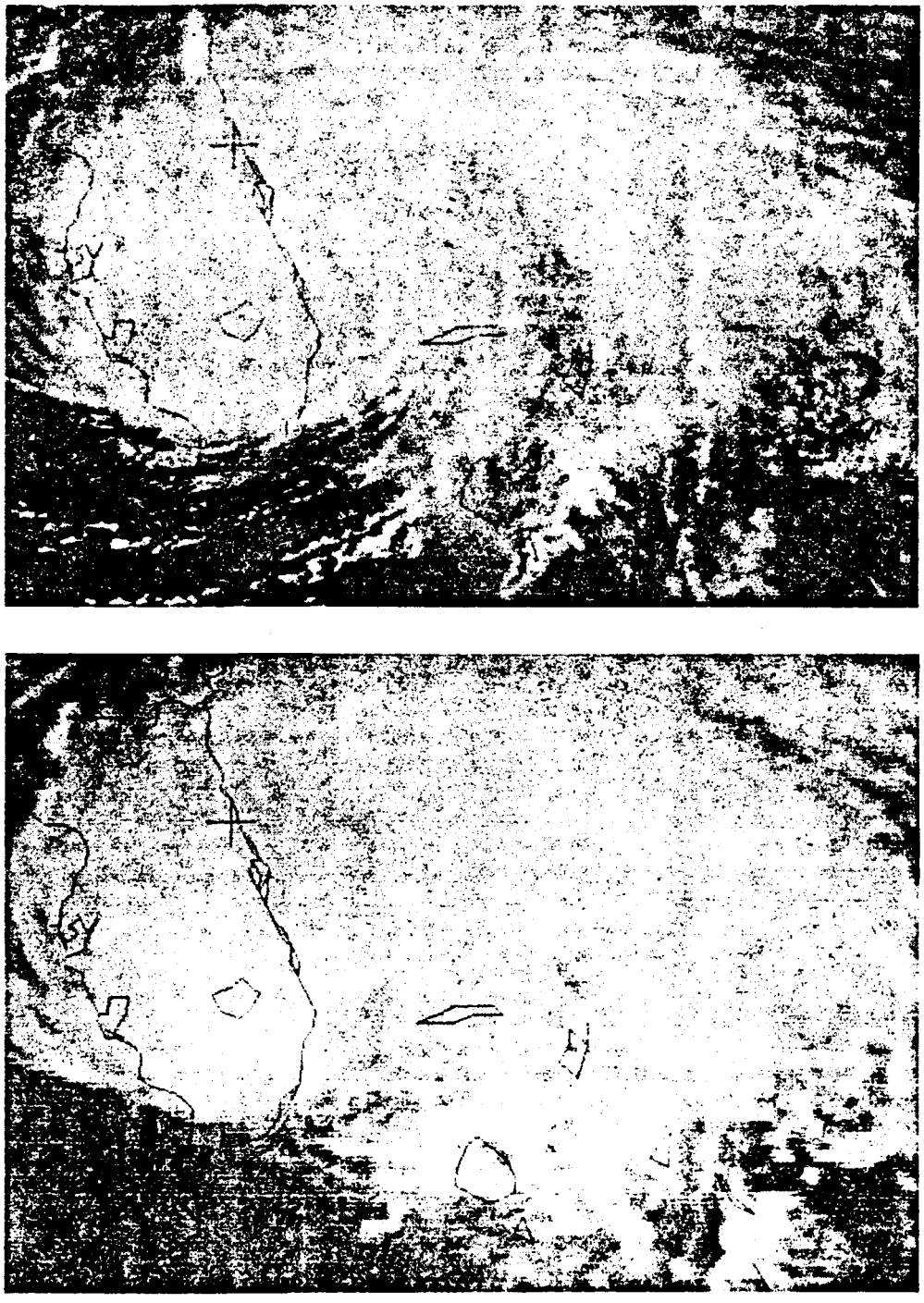


FIG. 6. (a) Visible image obtained from the SMS-2 satellite on 3 September 1979 at 1800 GMT which shows Hurricane Debbie near Daytona Beach, FL. (b) As in 6(a) except that the infrared image is shown.

between rainfall rates were derived for such isolated cells.

5. Summary

This study has shown that single pairs of visible and infrared geostationary satellite images can be objectively analyzed with pattern recognition techniques to determine rainfall rates in three operational radar rainfall classes. It also showed that radiance features provide some separation of rainfall classes in given grids; however, a greater skill score was obtained when texture features were incorporated into the analysis. Specifically, the addition of texture features along with

ORIGINAL PAGE IS
OF POOR QUALITY

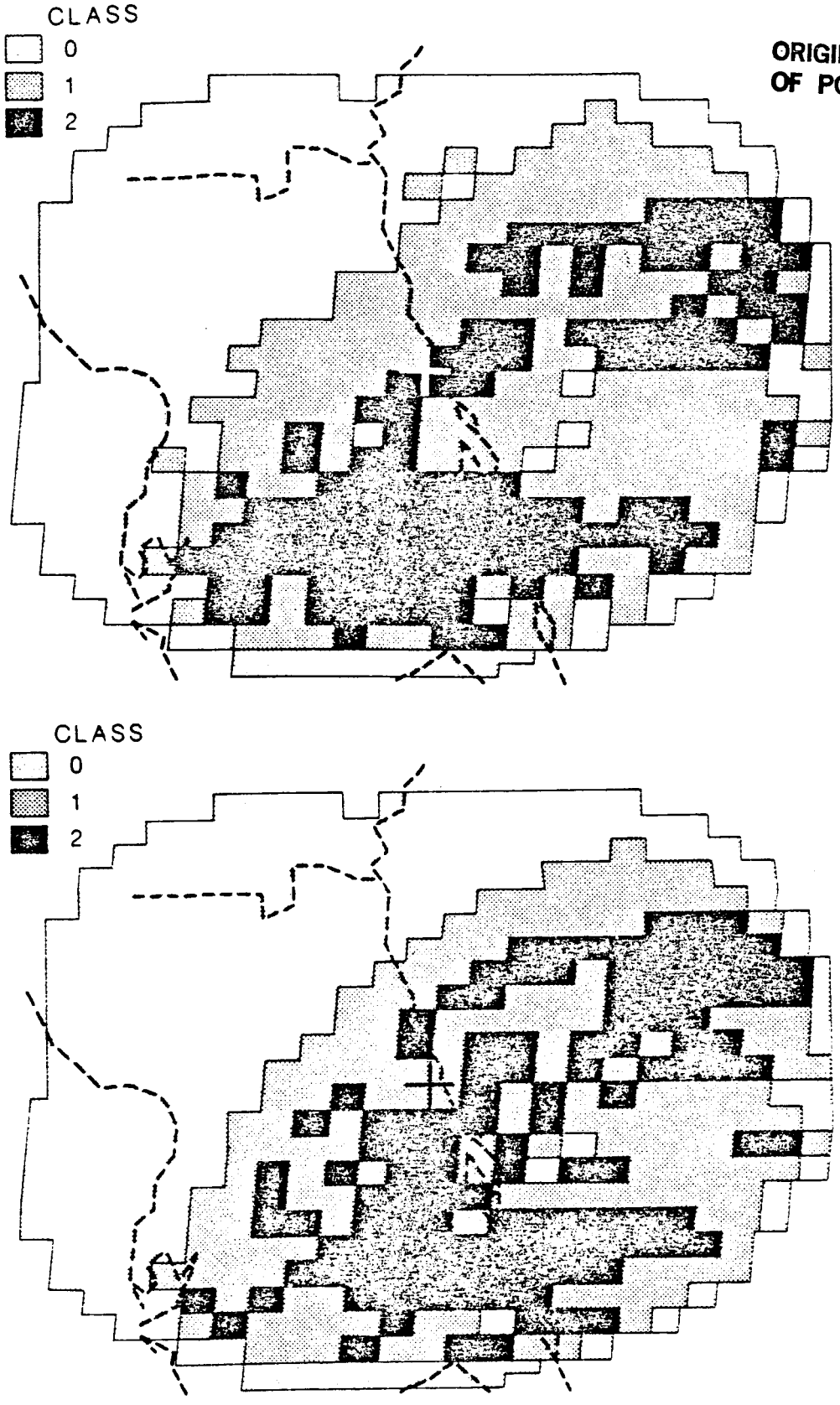


FIG. 6. (c) Derived rainfall category distribution: white = no data, light grey = 0, grey = 1 and black = 2. (d) Radar image obtained from the Daytona Beach radar. The grey scale is the same as for 6(c).

radiance features raised the skill score in identifying rain from 56 to 83%. Moreover, the classification into three classes could be achieved with a skill score of ~66%. The best results were obtained from images with high spatial resolution which revealed texture on a scale of a few kilometers.

The results of this study are still preliminary. More work is required to determine how well the rain rate classification technique works in other regions and at other seasons. Better pattern recognition algorithms may be developed as more experience is gained.

Acknowledgments. We wish to thank Ms. Bonita Lee for providing us with the algorithm that she employed in her rainfall study, Dr. D. W. Martin for providing meteorological insights regarding the satellite imagery, Dr. R. W. Spencer for providing some of the radar data used in this study, and Messrs. M. R. Howland and D. A. Santek for providing assistance in the use of the McIDAS.

Support for this research was obtained from National Science Foundation Grant ATM 8212424.

REFERENCES

Adler, R. F., and E. B. Rodgers, 1977: Satellite observed latent heat release in a tropical cyclone. *Mon. Wea. Rev.*, **105**, 956–963.

Anthes, R. A., 1982: *Tropical Cyclones, Their Evolution, Structure and Effects. Meteor. Monogr.*, No. 19, Amer. Meteor. Soc., 208 pp.

Atlas, D., and O. W. Thiele, Eds., 1981: Precipitation measurements from space. Workshop Rep., Goddard Space Flight Center, Greenbelt, MD, 358 pp.

Barrett, E. C., and D. W. Martin, 1981: *The Use of Satellite Data in Rainfall Monitoring*. Academic Press, 340 pp.

Follansbee, W. A., and V. J. Oliver, 1975: A comparison of infrared imagery and video pictures in the estimation of daily rainfall from satellite data. NOAA/NESS Tech. Memo. NESS 62, 14 pp.

Griffith, C. G., W. L. Woodley, P. G. Grube, D. W. Martin, J. Stout and D. N. Sikdar, 1978: Rain estimation from geosynchronous satellite imagery—visible and infrared studies. *Mon. Wea. Rev.*, **106**, 1153–1171.

Lee, B. G., and R. T. Chin, 1983: Classification of rain cells in satellite imagery. *IEEE Conf. on Computer Vision and Pattern Recognition*, Washington, DC, 405–406.

Lovejoy, S., and G. L. Austin, 1979: The delineation of rain areas from visible and IR satellite data for GATE and mid-latitudes. *Atmos. Ocean*, **17**, 77–92.

Muench, H. S., 1981: Calibration of geosynchronous satellite video sensors. AFGL-TR-81-0050, Air Force Geophysics Laboratory, Hanscom A.F.B., MA, 25 pp.

Negri, A. J., R. F. Adler and P. J. Wetzel, 1984: Rain estimation from satellites: An examination of the Griffith-Woodley technique. *J. Climate Appl. Meteor.*, **23**, 102–116.

Panofsky, H. A., and G. W. Brier, 1968: *Some Applications of Statistics to Meteorology*, Pennsylvania State University, 224 pp.

Parikh, J., 1977: A comparative study of cloud classification techniques. *Remote Sens. Environ.*, **6**, 67–81.

Raschke, E., and W. R. Bandeen, 1968: Beobachtungen der reflexions eigenschaften des systems erde-atmosphäre und der bewolkung über dem äquatorialen Pazifik von einem synchronen satelliten aus. *Ann. Meteor.*, **4**, 200–205.

Smith, W. L., L. D. Herman, T. Schreiner, H. B. Howell and P. Menzel, 1981: Radiation budget characteristics of the onset of the Summer Monsoon. *Int. Conf. on Early Results of FGGE and Large Scale Aspects of the Monsoon Experiment*, Tallahassee, (6-16)–(6-26) pp.

Suomi, V. E., R. J. Fox, S. S. Limaye and W. L. Smith, 1983: McIDAS III: A modern interactive data access and analysis system. *J. Climate Appl. Meteor.*, **22**, 766–778.

Swain, P. H., and S. M. Davis, 1982: *Remote Sensing, The Quantitative Approach*, McGraw-Hill, 396 pp.

Weszka, J. S., C. R. Dyer and A. Rosenfeld, 1976: A comparative study of texture measures for terrain classification. *IEEE Trans. Syst. Man Cybern.*, **SMC-6**, 269–285.

Yau, M. K., and R. R. Rogers, 1984: An inversion problem on inferring the size distribution of precipitation areas from raingauge measurements. *J. Atmos. Sci.*, **41**, 429–447.

ORIGINAL PAGE IS
OF POOR QUALITY

2

AUTOMATED RECOGNITION OF OCEANIC CLOUD PATTERNS. PART 1: METHODOLOGY AND APPLICATION TO CLOUD CLIMATOLOGY.

by

LOUIS GARAND

Recherche en Prevision Numerique,

Dorval, P. of Quebec, H9P1J3

January 1987

ABSTRACT

A scheme is presented for the automated classification of oceanic cloud patterns. The twenty classes reflect the rich variety of morphologies that are detectable from space. A training set is defined by 2000 samples of size 128 X128 km taken over the Western Atlantic in February 1984. The method uses visible and infrared images from a geostationary satellite. Class discrimination is obtained from thirteen features representing height, albedo, shape and multilayering characteristics of the cloud fields. Two features derived from the two-dimensional power spectrum of the visible images proved essential for the detection of directional patterns (cloud "streets", rolls) and open cells. Based on the assumption of multinormal distributions of the features, a simple classification algorithm is developed. From 1020 independent samples, the consensus of two out of three expert nephanalysts agreeing or not with the machine result suggests an overall accuracy of 79% with the machine answer at least second best 89% of the time. The cloud climatology in twenty classes for January and February 1984 are compared. Retrieved cloud fraction maps are also compared with the observed fields from ships. The scheme is proposed as a candidate for the International Satellite Cloud Climatology Project.

1. INTRODUCTION

In this first of two articles, the design of an automated and efficient cloud classification scheme is presented. The twenty classes reflect the rich variety of morphologies that are detectable from space. The cloud patterns are quantified with measures extracted from visible and infrared images. These measures, or features, describe the cloud fraction, height, albedo, shape and multilayering characteristics of the cloud fields. The vector of features permits an objective classification. Class-dependent relationships between cloud features and meteorological parameters of interest are developed in the second article (Garand et al., 1987, hereafter Part 2).

Various cloud classification schemes have been proposed in the past. Scientists responsible for the International Satellite Cloud Climatology Project (ISCCP, see Rossow et al., 1985), have conducted a comparison between the existing techniques in order to decide which one should be used for a global five year climatology. One of their conclusions is that "all methods, which work well for some cloud types or climate regions, do poorly for other situations". The number of classes for most algorithms is notably low. The cloud fields or individual pixels are typically assigned one of three height classes: low, middle and high. The ISCCP requirements presently include a fourth class: deep convective. In addition, cloud optical depth and cloud size distribution are also mentioned as desired parameters. This is an implied admission that a more detailed classification, that includes morphological considerations, is desirable.

A notable exception with regard to the number of classes is the work of Shenk et al. (1976) who designed a 10-class scheme. Their four-channel method was successful in detecting cirrus and multilayered systems but the coarse resolution, 55 km at nadir, did not allow the detection of much morphological detail in boundary layer cloud fields. Parikh (1976) presented a review of various cloud classification techniques. Basic concepts on tree structures, extraction of features and the use of discriminant functions applied to the cloud classification problem are described. Among the new approaches that have been tried, clustering in multispectral space (Desbois et al, 1982) is one that has shown skill in segmenting cloud pictures into homogeneous areas associated with cumulonimbus, cirrus or mixed cloud types. A drawback of that method however, and of pixel by pixel methods in general, is that by nature they are not suited for the detection of mesoscale cloud patterns. The differentiation between open versus closed cells, cloud "streets" versus ordinary cumulus fields or stratus versus stratocumulus cannot be achieved satisfactorily from scrutinizing multispectral histograms. The effect of cloud shape on visible-infrared signatures (Platt, 1983, Schmetz, 1984) has been investigated with limited practical success. For realistic cloud fields, multilayered systems in particular, several possible interpretations of the signatures is the rule rather than the exception. The basic problem of discriminating between broken cloud fields and overcast ones with variable optical depth still remains. In short, for the purpose of detailed cloud classification, it appears that a set of

features specifically designed to 'see' the morphology is required. Such features are in the realm of pattern recognition in the literal sense of the term.

The work of Rochard (1978) and Brard (1980) represents a rare effort aimed at the recognition of cloud field morphologies in detail. Their scheme discriminates 13 classes from 8 features. The boundary layer classes included open and closed cells, stratus and cumulus. Directional patterns were however not considered.

Preferably, the scale of the analysis should be compatible with numerical weather prediction models or general circulation models. The ideal scale for cloud pattern analysis, as it turns out, is similar to that of those models. In their work on image modeling of cloud fields, Garand and Weinman (1986), found that scale to be between 100 and 250 km. Such a scale (mesoscale) is large enough for the patterns to be recognizable, the texture primitive of the patterns being of smaller dimensions, yet small enough to insure a high probability of homogeneity of the cloud pattern and its associated weather conditions.

One incentive to proceed with the development of this classification scheme was the realization from the aforementioned work, that two simple power spectrum features provided reliable means to detect directionality and therefore cloud streets and rolls and to detect, in addition, the presence of open cellular patterns. It remained to be shown however that these features could permit the discrimination of mesoscale cellular patterns from all other cloud types. A general cloud classifier was therefore developed.

This study is limited to oceanic regions only. We limit our attention to the winter season in the Northern Atlantic. We make use of a large data set covering an area of 20 degrees latitude by 20 degrees longitude for the sixty days of January and February 1984. Chapter 2 defines the twenty classes to be recognized. In Chapter 3, following the description of the features for classification, the pattern recognition algorithm is presented along with the results on a training set of 2000 samples and on an independent test set of 1020 samples. Monthly and seasonal maps of cloud fraction are shown in Chapter 4 along with a comparison between satellite-derived and observed fields (from ships) of total cloud fraction. Also, the climatologies in twenty cloud classes for January and February 1984 are compared.

2. DEFINITION OF THE CLOUD CLASSES

The nominal scale of analysis employed in this study is 128 X 128 km; the nominal resolution of the visible sensor is 1 km. Power spectrum analysis, using fast Fourier transforms, is more efficient with sizes that are powers of two; this is the reason for choosing the particular number 128. This scale is too small to assign synoptic scale classes such as cyclone vortices or fronts but it is large enough to include several multilayered classes. With the inclusion of these multilayered classes, there is actually no need to search for homogeneous areas and the analysis can be performed on a fixed grid of

contiguous areas. Also we emphasize that the classes are defined from the viewpoint of a geostationary satellite. Thus, when compared to ground observations, both the scale and the classes may be different. For example, ground observers cannot report open cells or cloud streets, two cloud types that are among those investigated. Invoking this argument, human interpretation of the satellite pictures rather than shipboard observations of cloud type will serve as "truth". Three expert nephanalysts were assigned to the verification of the classification scheme on independent samples. The definition of the classes and the assignment of a class number to the training set samples were accomplished by the author.

The classes were first selected by experience from a series of images: the samples of each scene were labeled into as many classes as the cloud fields could be discriminated. The analyst (the author) sought the mesoscale cellular patterns mentioned above, the discrimination between cumulus and statocumulus, the detection of thin cirrus, multilayered systems and cumulonimbus clouds. Once a total of 20 classes was reached, the analyst felt hard pressed to define more classes without encountering a large number of ambiguous cases. The thresholds in height and albedo were defined during the analysis process. A formal definition of the classes implies the description of the discriminating functions. At this stage of the presentation however, in order to clarify the goal of this study, it is appropriate to describe the various morphologies to be recognized in words and images, rather than by equations. The number ordering from from 1 to

20 closely follows the mean cloud top height from lowest to highest. Class names are generic, except for mesoscale cellular convection classes 7 to 11. The names streets, rolls, open and closed cells are, however, pervasive in meteorological literature, occasionally mentioned by name in cloud atlases such as those of Scorer (1972) or the World Meteorological Organization (WMO, 1969), although these books are concerned with cloud patterns as seen from the ground. Scorer's (1986) book on cloud patterns as seen from satellite is closer to the needs of this study. An entire chapter (six) is devoted to mesoscale cellular patterns; these cloud patterns were also the scientific object of two recent field experiments, the Air Mass Transformation Experiment (AMTEX, 1975, East China Sea region, see Sheu and Agee (1977)) and the Convection and Turbulence Experiment (KONTUR, 1981, North Sea region, see Bakan (1985), Hoeber (1982)).

In the proposed classification scheme, the generic name cirrus corresponds to any cirriform class (cirrus, cirrostratus, cirrocumulus) and the generic name altocumulus corresponds to either altocumulus or altostratus. Cumulus, stratocumulus, stratus, nimbostratus and cumulonimbus are, however, recognized specifically.

The abreviations VIS and IR are used to designate the visible and infrared pictures, respectively. The algorithms for the estimation of cloud fraction, height and albedo are described in Chapter 3. Fig. 2.1 provides one example for each class of visible-infrared pairs. The reader is invited to examine these examples while reading the description of the cloud classes.

Class 1. CLEAR

The cloud fraction is less than 1%. When clouds are present at such a low cloud fraction, they are usually small cumuli. VIS: dark. IR: dark.

Class 2. STRATUS

Low cloud deck with smooth surface, usually one cloud entity without holes.

VIS: Albedo typically moderately bright (50 to 80%).

IR: Quite dark, sometimes clouds are not discernable from background. Mean height is 1.4 km and does not exceed 2.5 km. Above that height, this morphology belongs to class 12 (nimbostratus).

Class 3. SCATTERED CUMULUS

Low clouds with grainy texture. Cloud cover less than 50%.

VIS: Albedo relatively low, 30 to 45% although the middle of the cloud elements may be bright. The individual clouds are usually small and numerous.

IR: Dark or grey, depending on height, and fairly uniform. The typical height is 1.8 km and can reach 3.5 km.

Class 4. BROKEN CUMULUS

Very grainy texture with cloud fraction higher than 50%. The clouds seem packed against one another resulting in numerous small background areas.

VIS: Grey to semi-bright, mean albedo 43%.

IR: Grey, fairly uniform except for some towering cumulus not exceeding 5 km. Typical height: 2.5 km.

Class 5. SCATTERED STRATOCUMULUS

Low cloud deck with cloud fraction less than 50%. The clouds tend to be connected in sizeable blobs so that most of the cloud fraction is made up of a few clouds only, as opposed to the cumulus class.

VIS: Average brightness 40%. When brighter than 60%, the class becomes 11 (bright closed cells).

IR: Dark to grey. Mean height of 2.4 km, not exceeding 3.5 km.

Class 6. BROKEN TO OVERCAST STRATOCUMULUS

Same as class 5 but with cloud fraction higher than 50%.

VIS: Average brightness of 46%, not exceeding 60%.

IR: Mean height of 2.7 km.

Class 7. CLOUD STREETS

Low cloud pattern with obvious directionality. Typical cloud fraction of 58% but may vary from 15% to 90%. The 'streets' normally appear made up of cumulus clouds and the texture is grainy.

VIS: Mean albedo of 43%. When compared to class 8 (rolls), the directional pattern usually has a shorter wavelength and the albedo is less.

IR: Fairly uniform height, 2.3 km on the average.

Class 8. ROLLS

This obviously directional pattern is at mid level. Fairly thick, large

roll clouds are aligned usually with little spacing between them. Some open cells may be embedded in the field.

VIS: Bright, mean albedo 75%. Mean cloud fraction of 93% and usually not less than 60%.

IR: Grey to whitish, typical height: 4 km, less than 6 km.

Class 9. POLYGONAL OPEN CELLS

Open cells presenting a honeycomb or polygonal texture with sizeable holes or internal cavities in the middle of the cells. Small cumuli are also often present. Differentiated from class 10 by a lower cloud fraction and larger holes. The most convective cloud elements are individual towering cumuli as opposed to the entire doughnut shape cloud pattern in class 10. The cloud ring surrounding the hole may be incomplete whereas it is typically complete for class 10.

VIS: Moderately bright, average albedo 55%.

IR: Greyish brightness, darker in regions of small cumuli and brighter for the more convective cells which may reach 5.5 km. Typical height 3.5 km.

Class 10. STRONGLY CONVECTIVE OPEN CELLS

Bright mid level cloud field characterized by doughnut shaped cloud elements with holes a few km in diameter.

VIS: Bright, typical albedo 63%. Mean cloud fraction 93% and rarely lower than 60%. The texture appears lumpy.

IR: Greyish to whitish with the holes usually perceivable. Mean height of 4.4 km, may reach 6 km.

Class 11. BRIGHT CLOSED CELLS

Bright mid level cloud field with large blobs. May appear lumpy indicating towering cumulus. This class also encompasses the edge of class 12. VIS: Bright, mean albedo 63%. Typical cloud fraction 80% but may vary between 30 and 95% if the texture is lumpy and between 30 and 85% if the texture is smooth (edge of class 12). Above these upper limits in cloud fraction, the sample belongs to class 12.

IR: Greyish , typical height 3.4 km.

Class 12. NIMBOSTRATUS

Overcast bright stratum at mid level. The texture is usually smooth but a somewhat more lumpy texture with cloud fraction higher than 95% will also be labelled 12.

VIS: Very bright. Typical albedo 77%. Typical cloud fraction of 98% and never less than 85%.

IR: Greyish to whitish, smooth. Mean height 4 km, may vary from 2.5 to 6 km.

Class 13. ALTOCUMULUS

Greyish mid level cloud deck, apparently single-layered.

VIS: Usually quite grey, typical albedo 34%. Typical cloud fraction 45% but may vary from 1 to 100%.

IR: Greyish to whitish. Fairly uniform. Typical height of 4.2 km and may vary from 3.5 to 6 km.

Class 14. CUMULUS WITH ALTOCUMULUS

This cloud field consists of a lower cloud deck of cumulus type and of a mid level cloud deck (between 2-6 km).

VIS: Typical albedo 47%. Higher deck made up of sizeable patches whereas lower deck is typically grainy (cumulus).

IR: The lower deck is dark, the mid level deck is greyish to whitish. Mean height of 4.8 km, not exceeding 6 km.

Class 15. STRATOCUMULUS WITH ALTOCUMULUS

Cloud field with apparent multilayering occuring between 2 and 6km, with lower cloud deck typically stratocumulus.

VIS: Semi-bright, typical albedo 47%. Typical cloud fraction 72%.

IR: Varying tones between greyish and whitish. Mean top height 5.5 km, not exceeding 6 km.

Class 16. THIN CIRRUS

Fibrous texture, semi-transparent.

VIS: Low albedo, 25% on the average and less than 35%. Presence detected from milky veil and sometimes not detected at all. Lower cloud deck may be present.

IR: Whitish, often with considerable structure. Mean apparent height of 6 km with most of the cirrus field typically appearing in the infrared image at lower heights.

Class 17. MULTILAYERS WITH CIRRUS

High clouds are obviously present from the infrared image and most often lower level clouds as well and the visible image is greyish.

VIS: Typical albedo 41%, covers the range 35-55%. The typical cloud fraction is 87% but it is sufficient that 5% of high clouds (above 6km) be present for the field to be classified 17. The overcast version of this class will be classified 19 only if the percentage of high clouds is greater than 85%.

IR: Considerable structure from greyish to white. Mean cloud top height of 8.7 km.

Class 18. BRIGHT MULTILAYERS WITH CIRRUS/CUMULONIMBUS

General description as for class 17 except that the visible picture is moderately to very bright (albedo greater than 55%). This class encompasses isolated cumulonimbus or edges of cumulonimbus.

VIS: Bright, typical albedo 72%. Typical cloud fraction 94% but 5% or more high cloud fraction is sufficient for the field to be classsified 18. The overcast version will be classified 20 only if the percentage of high clouds is greater than 85%.

IR: Same as 17. Mean height 8.9 km.

Class 19. DENSE CIRROSTRATUS

Overcast field of high clouds with less than 15% of the pixels at height below 6 km.

VIS: Grey, typical albedo 50%. Typical cloud fraction 97% and no less than 90% (classified 17 in that case).

IR: White, possibly a small greyish region, indicating some mid-level cloud deck. Mean height 10.3 km.

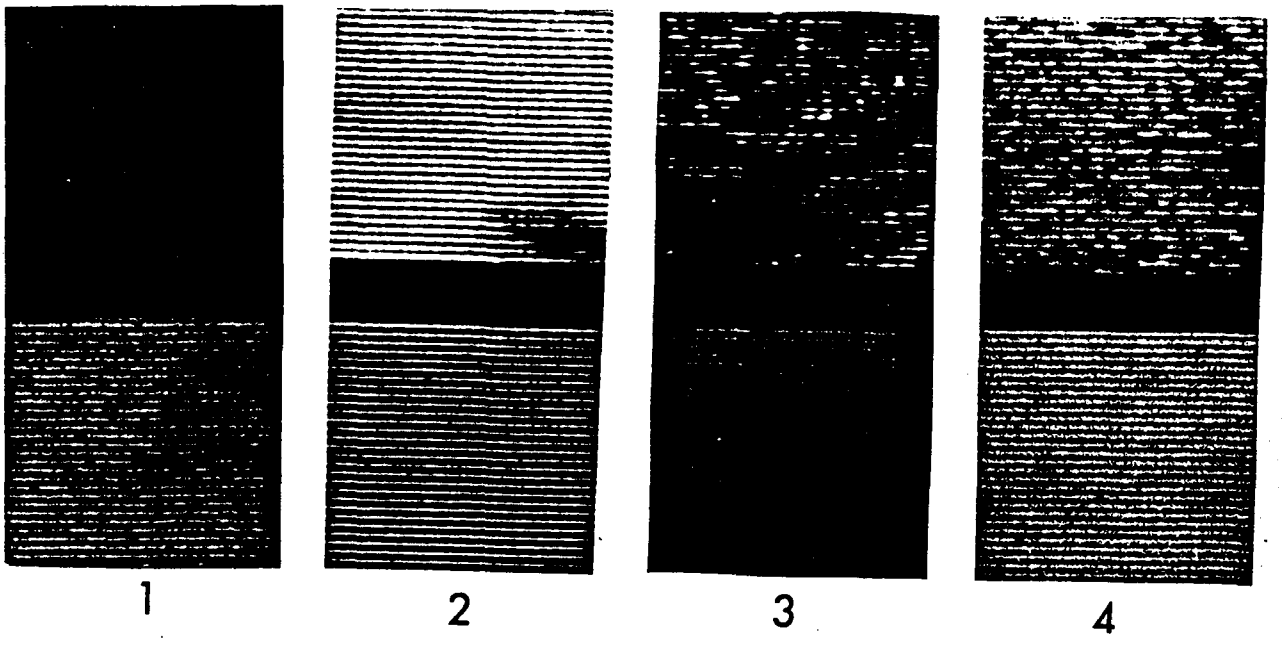
Class 20. OVERCAST CUMULONIMBUS

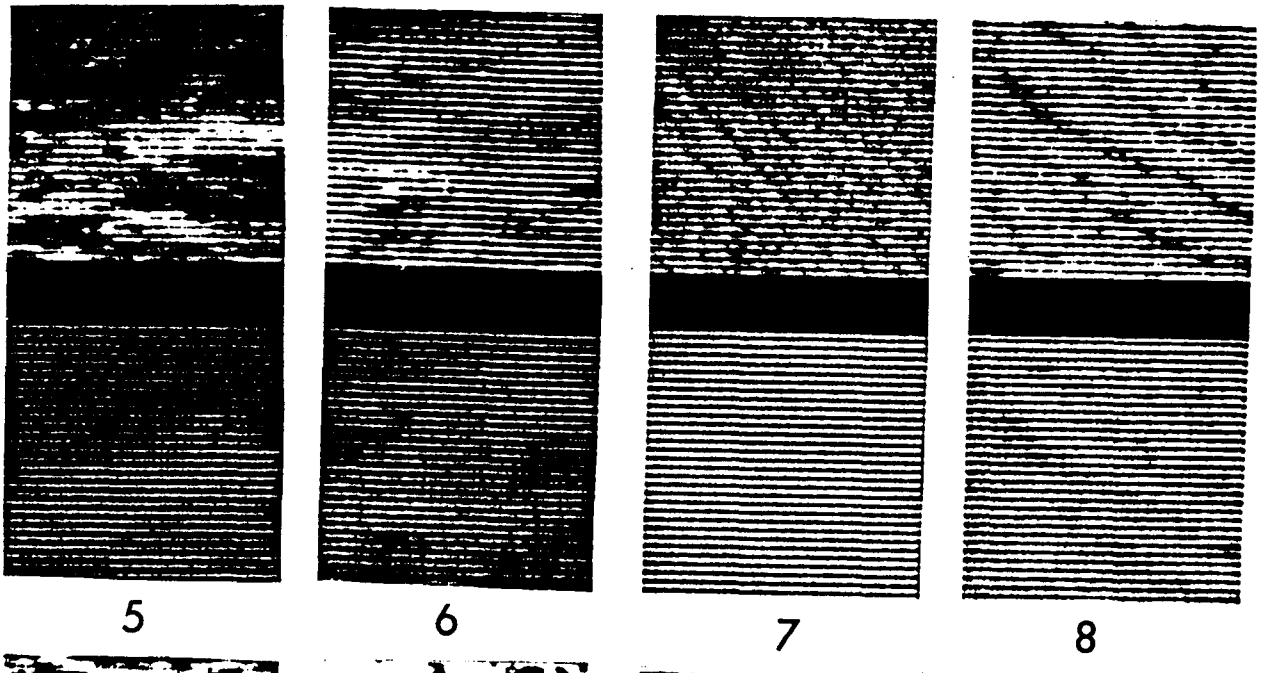
High and bright overcast cloud field. Usually represents deep cumulonimbus in the core of a vigorous cyclonic system or cold front. Less than 15% of the pixels are below 6 km.

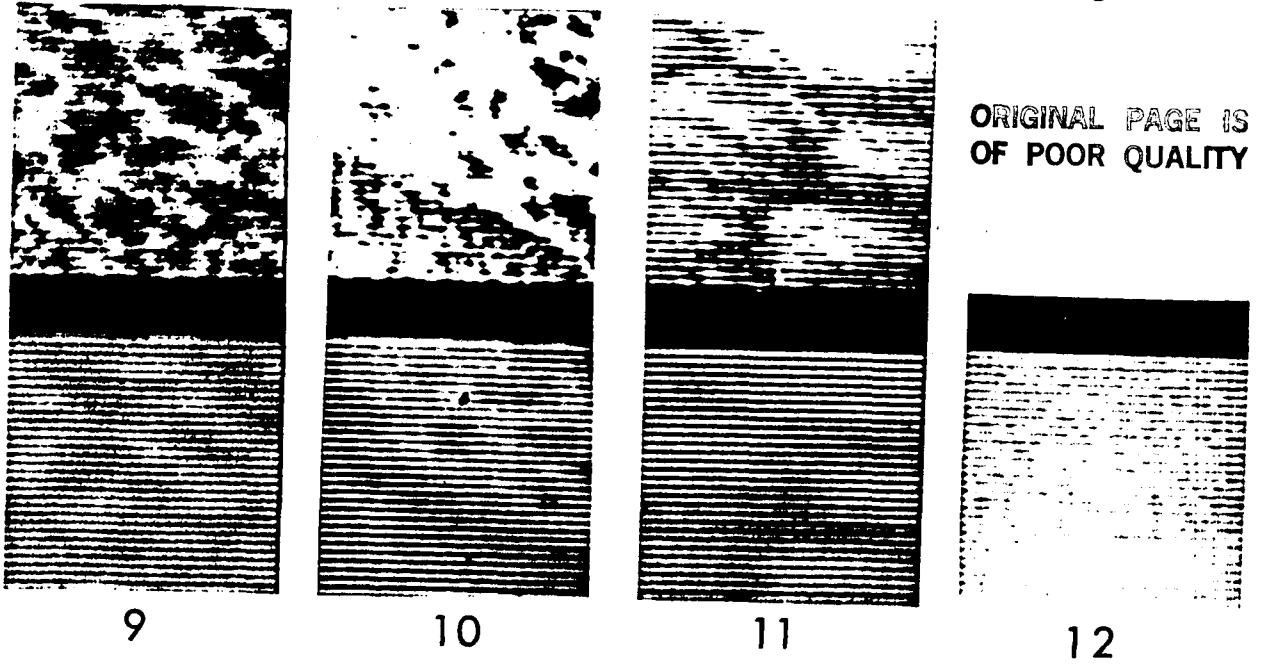
VIS: Very bright; typical albedo 87%. Typical cloud fraction 100% and no less than 90% (classified 18 then).

IR : White. Typical height 10.7 km.

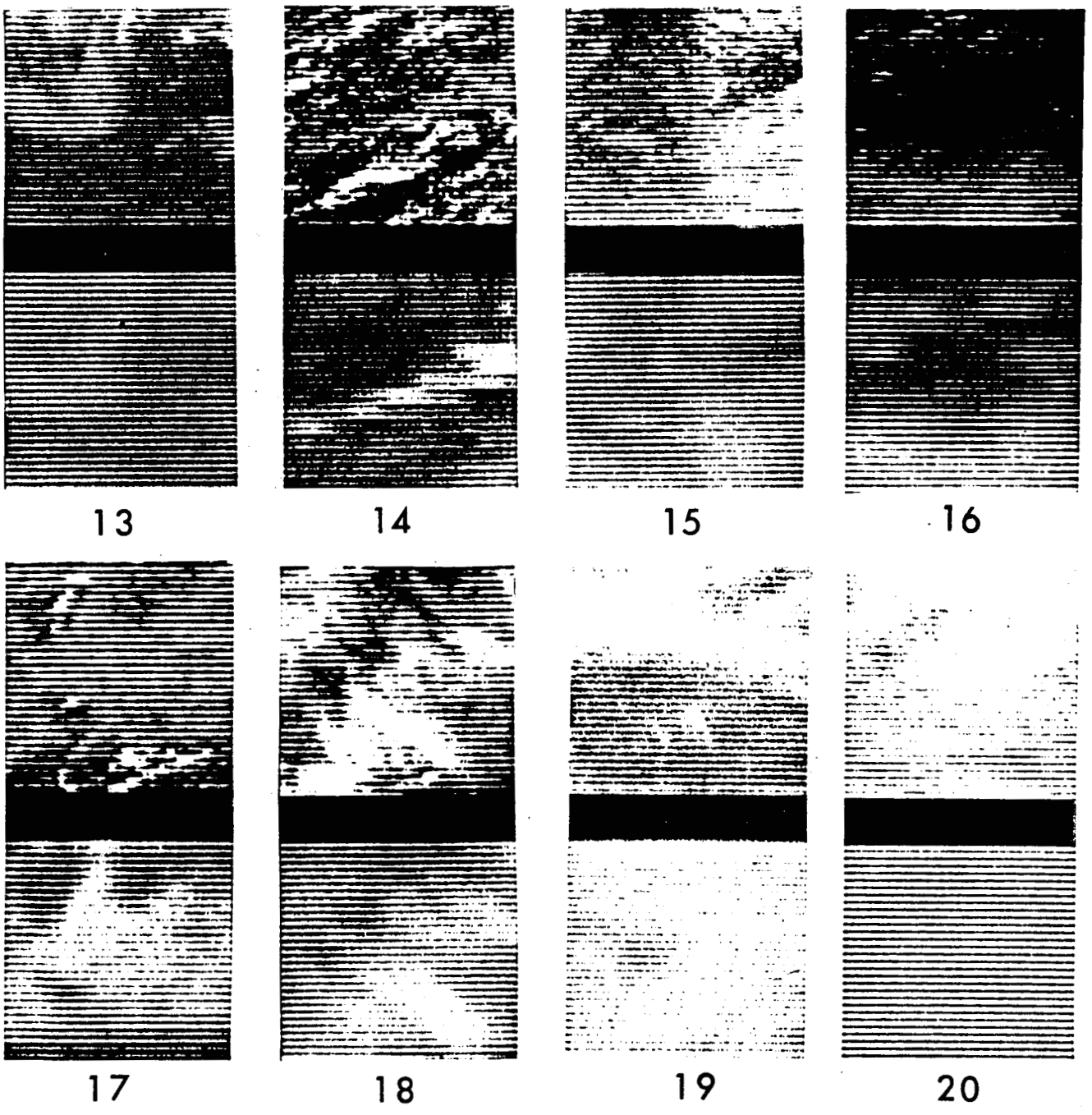
Fig. 2.2 summarizes the thresholds in height and albedo mentioned in the description of the classes. The standard deviations are also shown. The plot is an anticipation of the results obtained in Chapter 3 with a large training set of cloud patterns. It should be kept in mind that the natural limits of height and albedo are about twice the standard deviations presented on the graph. The figure indicates that although some classes (e.g. 1 and 2) are relatively well separated, it is obvious that the discrimination cannot be accomplished from albedo-height characteristics only. Boundary layer classes 3-7 form a closely packed group as well the higher albedo mid-level classes 8-12 and the altocumulus classes 13-15. Features describing the morphology and the state of multilayering are essential to separate those classes.







ORIGINAL PAGE IS
OF POOR QUALITY



ORIGINAL PAGE IS
OF POOR QUALITY

Fig. 2.1 Example of a visible and infrared pair of images for each cloud class, indicated by its number. The visible image is on top of the corresponding infrared image. Image size: 128 X 128 km.

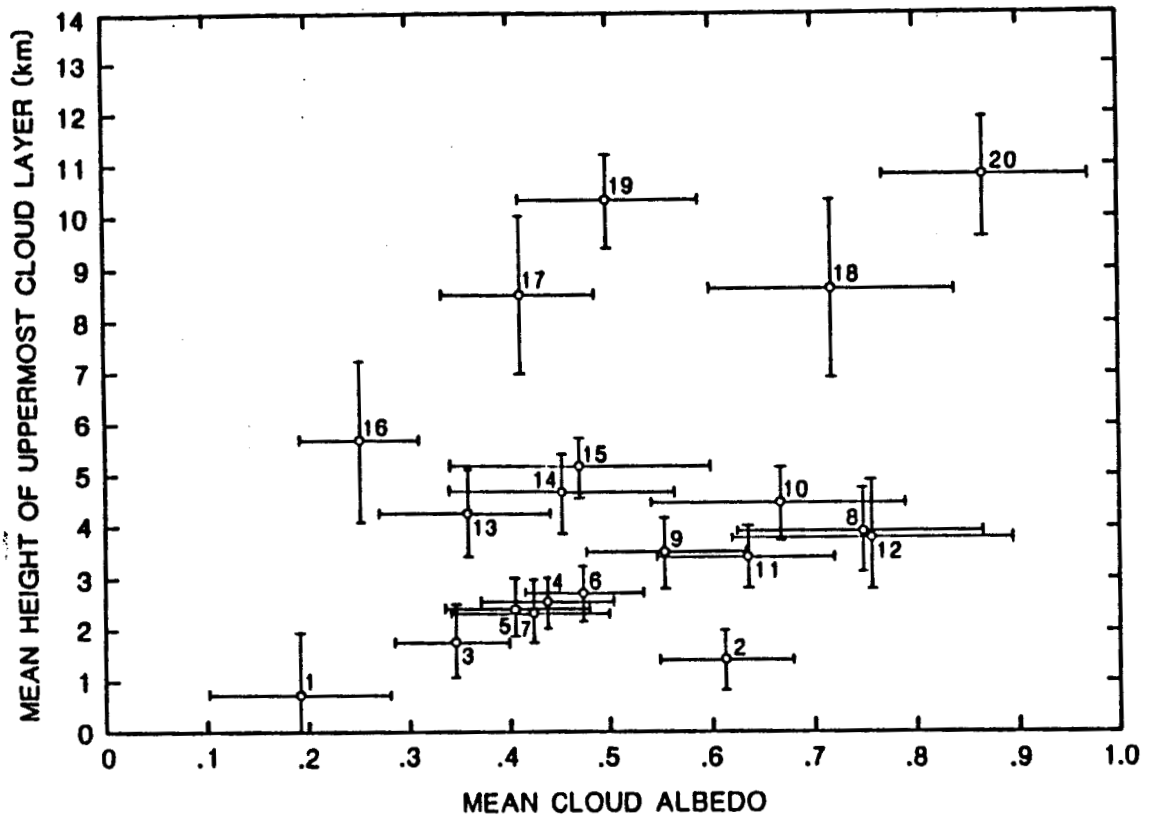


Fig. 2.2 Mean height of uppermost cloud layer (km) versus mean cloud albedo for each cloud class, indicated by its number. Associated standard deviations shown by bars.

3. DESIGN OF A CLASSIFIER

3.1 Data set

In order to recognize all of the twenty classes just defined, a large data set was required. Twenty nine images were analyzed, one per day for the 29 days of February 1984 at 16 GMT, about 11-12 AM local time, for the Western Atlantic region defined in Fig. 3.1. The region is between 26 and 45 degrees latitude north and 60 to 80 degrees longitude west; the west side of the domain is defined by the east coast of the United States.

This region and time of the year were chosen after the hard copy archives were examined (Space Science and Engineering Center Library, University of Wisconsin). Winter brings several cold air outbreaks in this area; these systems produce a significant number of occurrences of mesoscale cellular patterns. February 1984 was particularly interesting from that perspective. A secondary goal was to produce the cloud climatology for that month, in order to illustrate both real time and climatological applications of the method.

Exactly 204 contiguous boxes were analyzed for each scene (one per day), as indicated in Fig.3.1, except for 3 days where small parts of the images were missing. In all, 5845 samples were analyzed for a coverage of 98.8% for the month (completeness implies 29 X 204 = 5916 samples). Analysis here refers to the extraction of features for classification, a topic to be discussed in the following section. With such a data base, all twenty cloud classes were represented a

ORIGINAL PAGE IS
OF POOR QUALITY

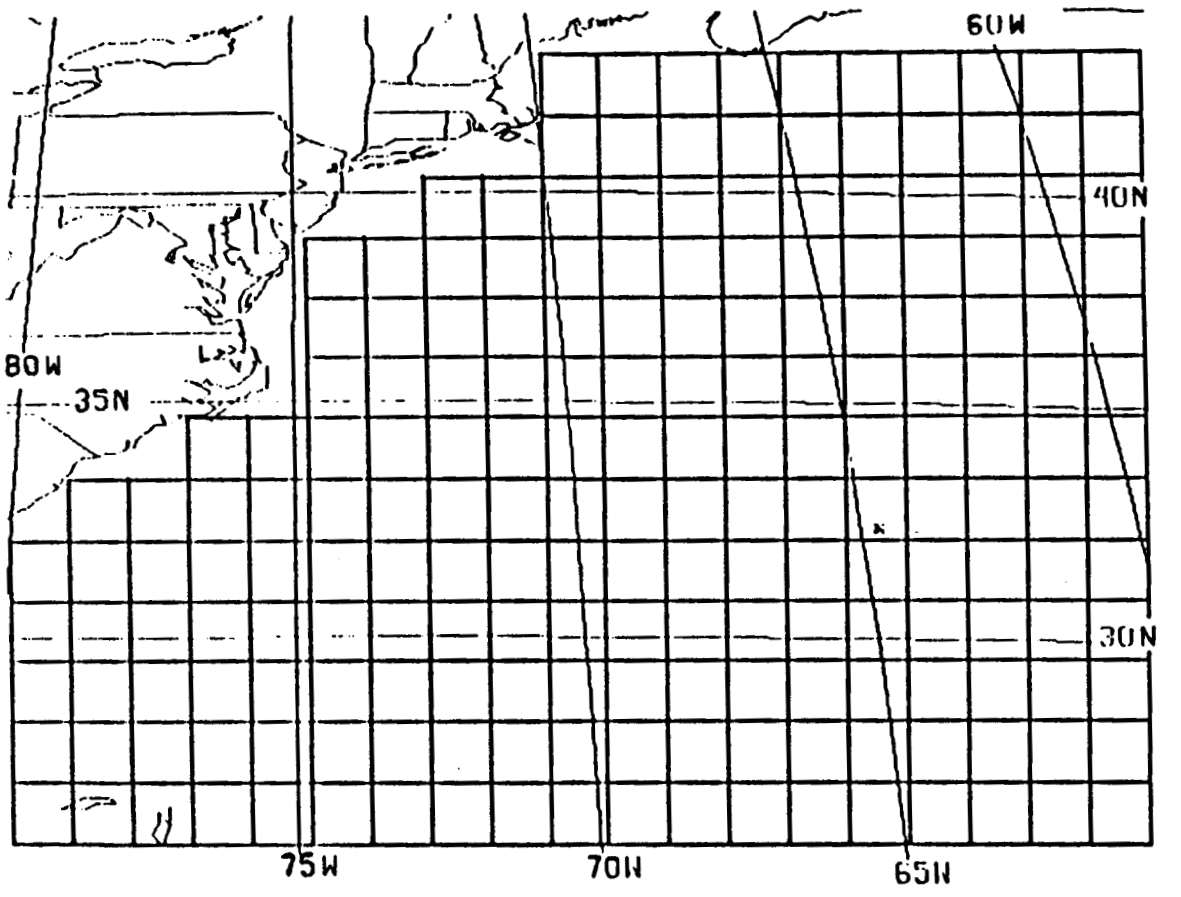


Fig. 3.1 Region of analysis seen in satellite projection. Asterisk indicates Bermuda. The grid shows the 204 contiguous areas to be analysed. Size of areas: 128 X 128 visible pixels at nominal 1km resolution.

significant number of times. A grid was superimposed on the satellite image and a sample number was placed in the bottom of each box. The author then subjectively assigned a class number to each sample identified by its number and keyed in that information in the record of the features just extracted. The decision on the class was taken after switching back and forth between the visible and infrared pictures. A hard copy image of each scene was taken for both the visible and infrared images and the record of the features was also printed. Thus the analyst had all material for further analysis in hand.

Each visible image consists of m = 64 X 64 = 4096 pixels at 2 km resolution and each infrared image consists of n = 32 X 32 = 1024 pixels at 4 km resolution, the nominal resolution of the infrared sensor (the actual footprint is 4 X 8 km with the same digital count assigned to two 4 X 4 km pixels). It was deemed appropriate not to degrade the visible resolution to that of the infrared in order to preserve information on morphology. On the other hand, the full 1 km resolution was not kept for computer time considerations. A philosophy applied throughout in the feature extraction process is not to rely on collocated visible and infrared pixels but rather to match cloud fraction thresholds in both histograms. The visible image was reduced to 2 km resolution by sampling every other line and row, a method preferable to averaging to preserve cloud properties. Eight visible sensors are disposed vertically to scan eight lines at a time as the optical system scans from the left to the right side of the planet. It was found by expanding full resolution visible images several times

that horizontal stripes were often present at eight line intervals indicating that one of the eight sensors was in error by a few digital counts. That sensor turned out to be associated with odd lines; this problem was then eliminated simply by sampling over even lines.

Each infrared grey level count corresponds to a radiance which can be transformed into a temperature via the Planck function. This temperature is called the brightness temperature. This transformation implies the assumption that the emitting surface is radiatively black, i.e. its emissivity is unity.

3.2 Extraction of features for classification

Thirteen features are used to classify the cloud fields in this study. About three times that number were initially defined as we could not know beforehand which features would provide best results. A classification algorithm should use as few features as possible in order to simplify the decision process and to shorten the computer time devoted to feature extraction. In addition, the number of samples necessary for reliable statistics increases rapidly with the number of features as well as the number of classes. The variety of features finally selected reflected a balance of information on height (cloud top, multilayering), shape (directionality, size distribution) and albedo.

In choosing the features, obvious physical significance is a desirable asset. Cloud fraction at low, middle and high altitude, cloud top height and mean cloud albedo are among the features selected. In

Table 3.1 Designation of the features used for classification in this study with associated 2-letter identification code. Image source in parenthesis: IR: infrared, VIS: visible, B&W: binary corresponding to visible cloud fraction, PS: power spectrum. D, DC*, m defined in text.

Code	Description	Limits
CF	Total cloud fraction (IR, VIS)	0-1
LO	Low cloud fraction (IR)	0-1
MI	Middle cloud fraction (IR)	0-1
HI	High cloud fraction (IR)	0-1
HT	Cloud height of uppermost layer (IR)	0-14km
LR	Fraction of cloudy pixels with D < Dc* (VIS)	0-1
AL	Mean albedo of cloudy pixels (VIS)	0-1
NC	Number of clouds (B&W)	0-m/2
ML	Multilayer index (IR)	0-1
BC	Background connectivity (B&W)	0-1
CC	Cloud connectivity (B&W)	0-1
ST	Streakiness factor (PS)	0-1
SE	Fraction of spectral intensity associated with wavelengths between 20-40km (PS)	0-1

addition, less conventional cloud field descriptors are employed such as a multilayer index, a streakiness factor and connectivity indices that are easy to relate to the visual appearance of the images. This is an advantage over features that represent moments taken over pictures, (see Haralick, 1976) as these features are often difficult to interpret.

Every feature is identified with a 2-letter code for further reference. Table 3.1 presents those features, along with their physical limits.

3.2.1 Cloud fraction and height features (LO, MI, HI, CF, HT)

Because a good algorithm to define cloud fraction is essential, considerable attention was devoted to this problem. A basic requirement is that the scheme should be usable throughout the day, from shortly after sunrise to shortly before sunset. Therefore, the geometry of the system has to be considered appropriately. Fortunately, this problem is well understood and a good treatment of it can be found in the series of three papers by Minnis and Harrison (1984, hereafter MHA-a, b, c). Three angles define the geometry: the solar zenith angle (ς), the satellite-viewing zenith angle (θ) and the viewing azimuth angle (ψ) (see MHA-a, Fig.3). The three angles are obtained from knowledge of day of the year, time of the day, satellite position and field of view location. Considering those angular factors, the visible brightness (or digital count) corresponding to a reflectivity t at nadir is (MHA-a, Eq.6):

$$D_t = \{\delta_\nu(\zeta)\chi_\nu(\zeta,\theta,\Psi)\cos(\zeta)\ B(0^\circ,t)\pi^{-1} + D_o^2\}^{\frac{1}{2}} \qquad (3.1)$$

where $\delta_\nu(\zeta)$ is the visible normalized directional reflectance and $\chi_\nu(\zeta,\theta,\psi)$ is the visible, anisotropic reflectance correction factor; ν refers to the spectral band. Both δ_ν and χ_ν values for water were obtained empirically from a large data set of GOES images to gather statistics from all possible angular combinations. A reasonable value for t is 7% for water. The existence of this model, defined by its tables of δ_ν and χ_ν, was a decisive incentive to design our scheme to be used with the natural satellite projection. The tabulated values of δ_ν and χ_ν for water were provided by the authors of MHA a-c. The constant B(0,t) is the hemispherically integrated brightness count at $\zeta = 0$. D_o, on the other hand, is the dark current constant. Its meaning will become explicit below. In MHA-c, the average clear-sky albedo (ocean plus atmosphere) over our region of interest (their Fig.10, derived in November 1978) is 15%. Therefore, we shall use the constant t = 0.15. So, Eq.(3.1) simply answers the question: given the three relevant angles, what is the digital count that the satellite would register corresponding to a clear-sky reflectivity of 15% at nadir? The visible calibration is defined by the relation:

$$E = a'D^2 + b' \qquad (3.2)$$

where E is in W/m^2 and D is the satellite-observed digital count with range 0-255. For GOES-EAST in early 1984 (subsatellite point: equator, 75 W, height of 36,000 km), the values suggested for a' and b' are 0.005393 and -2.67 W/m^2 respectively. The value of D_o^2 is thus 496.

The reflectivity is obtained from:

$$R = E/(I_o \mathrm{Cos}(\zeta)) \qquad (3.3)$$

where I_o = 336.43 W/m^2 is the fraction of the solar constant within the spectral bandwidth of the visible sensor. A reflectivity of 15% corresponds to 50.46 W/m^2 from (3.3) which in turn corresponds to a digital count of 99.26 from (3.2). Using this value in (3.1), one gets the value of B(0,15%) = 29408. Eq.(3.1) is universal and can be applied over all oceans uncovered by ice. Only the satellite related constants, D_o and B(0,t) need to be adjusted. The tables of and are much more complicated over land as they depend on the reflective characteristics of each type of surface.

As in MHA-a, the boundaries between low, middle and high clouds are 2 km and 6 km and the height assignment is based on an assumed vertical temperature lapse rate of 6.5 deg/km with the sea surface temperature, Ts, as the lower boundary. The sea surface temperature is found in the following manner:

1) The percentage of pixels in the visible image below D_t (with t = 0.15), f(t), is calculated. If f(t) is greater than 5%, the average brightness temperature of the warmest f(t) pixels in the infrared histogram, $\overline{T(t)}$, is calculated and Ts is estimated through Ts = $\overline{T(t)}$ + 4. The offset of 4 K approximates the atmospheric correction; it was obtained from comparisons of ship measurements of Ts versus infrared brightness temperatures in clear areas observed in several images. In Part 2, the accuracy of this technique for single retrievals is

evaluated at 2.69 K (rms) but may be improved to 2.2 K upon subtracting a class-dependent bias after classification. If the inferred value of Ts is off by 5 K or more from the monthly climatology, the climatological value is assigned. More accurate and physically based methods of sea surface estimation exist. For example, Bates and Smith (1985) claim errors of less than 1 K. However, images from three infrared channels are required; these were not always available. Also, it must be kept in mind that, in our region of interest, for about 50% of the time, the climalogical value of Ts is used due to excessive cloudiness. In those cases, it is not possible to use infrared methods such as that of Bates and Smith (1985).

2) If the percentage of totally clear pixels, f(t) is smaller than 5%, we assumed that there are no holes sufficiently large in the cloud field for an accurate surface temperature assignment. Therefore, in that case, the climatological value for the month of February was assigned (one degree scale). The mean of Ts for a particular month is usually within 1.5 K from the all-time climatology for that same month (see the National Oceanic and Atmospheric Administration (NOAA) publication: Monthly Oceanographic Summary for one-degree grids of Ts and deviation of Ts from climatology for our region of interest). NOAA polar orbiting satellites continuously monitor the sea surface temperature globally; available values for Ts are usually less than a week old. When possible, one may prefer to use this product as opposed to a climatological value in overcast conditions. In any event, for the purpose of cloud classification, the accuracy on Ts obtained by the

present method is sufficient.

Two modes are used to find the cloud fraction: a visible mode based on an albedo threshold and an infrared mode based on a height threshold. We define Dc as the cloud-no cloud threshold in the visible histogram and Tb as the cloud-no cloud temperature threshold from the infrared histogram. The usual mode (83% on the February data set of 5845 samples) is the visible mode.

1) Visible mode

In the visible mode, the digital count threshold, Dc* is obtained from:

$$Dc^* = D_t + Dm \qquad (3.4)$$

where Dm is an offset equal to 20 counts. This corresponds to an albedo threshold of 22% (for utilization with other platforms, it is suggested to use B(0, 22%) in Eq. (3.2) and Dm = 0 in Eq. (3.4)). Corresponding to Dc*, one gets the cloud fraction CF = CF(VIS). The offset was obtained from extensive experiments with cloud fields of all types with various viewing geometries. Images consisting of 64 X 64 pixels at 2 km resolution were thresholded to binary images (black and white) based on Dc*. Both the real image and the binary images were enlarged to fill the entire video screen of the MCIDAS system (Suomi et al., 1983). Then the analyst would switch back and forth between the two images, collocated on the screen, to subjectively estimate the quality of the thresholding procedure. It was found that Dm = 20 counts systematically provided a satisfactory threshold. Between D_t and Dc*,

it is admitted that clouds may be present but the assumption is that the field of view of pixels with such grey counts is less than 50% cloud covered. No attempt was made to calculate the cloud fraction of a single field of view within the limits 0 and 1. Thus, the cloud fraction defined here may be termed "effective". We assume that, to a large extent, possible errors due to underestimation of cloud fraction within a field of view when the pixel is assumed completely clear are compensated equally by possible errors of overestimation when the pixel is assumed completely cloud filled.

2) Infrared mode

The visible threshold Dc* fails for low-albedo pixels which may be completely cloud filled with semi-transparent clouds. Cirrus fields often present such characteristics: a low albedo (lower than Dc*) in the visible matched by the appearance of a veil of variable brightness in the infrared. Thus, a second mode is necessary.

In the infrared mode, any pixel corresponding to a height of 1 km or more is assumed cloudy. We then find the infrared cloud fraction CF(IR). If CF(IR) is greater than CF(VIS) by 5% or more, then the infrared mode is chosen. The value of Dc (equal to Dc* up to now) is lowered so that CF(VIS) = CF(IR). Since errors on sea surface temperature are typically much less than 6.5 K, 1 km is a safe margin for such errors resulting in errors on height (recall that a lapse rate of 6.5 K/km is assumed for height estimation). On the other hand, pixels of albedo lower than Dc* and of apparent height below 1 km can

safely be assumed clear in most cases.

The cloud top temperature, TT, is obtained from the brightness temperature corresponding to the 97th percentile in the infrared histogram. For clear skies, TT = Ts. The cloud top height, HT is obtained through HT= (Ts - TT)/6.5. It is understood that the true height may differ from HT. The temperature lapse rate for boundary layer cloud fields is often close to 10 K/km (dry adiabatic), as opposed to 6.5 K/km, and the surface air temperature is more appropriate than Ts as lower boundary. As a classification feature however, HT is not required to represent the true height and a unique, robust definition of each feature is desirable. After classification, one may estimate the true height from an assumed class-dependent temperature lapse rate. In addition, it should be noted that feature HT is not designed to obtain the representative cloud top height of the entire cloud field but that of the uppermost layer.

When there are large sea surface temperature gradients, such as in the midst of the Gulf Stream, the infrared mode may be selected even in clear conditions. To avoid this problem, if the sea surface temperature difference from climatology across the box is greater than 6.5 K (thus apparent cloudy pixels above 1 km height may be registered) and if HT < 2 km, the infrared mode is skipped; sea surface temperature differences acoss a box will never reach the 13 degrees corresponding to a 2 km apparent height.

From knowledge of the cloud fraction, CF, an important physical parameter is the apparent cloud base temperature, Tb, which is the

temperature corresponding to CF in the infrared histogram; pixels of brightness temperature higher than Tb are assumed clear. Having extracted Ts and Tb, the formal definitions of the low cloud amount (LO), the middle cloud amount (MI) and the high cloud amount (HI) follow:

i) LO is the percentage of pixels with brightness temperature T such that $Tb < T \leq Ts - 13$ with LO = 0 if $Tb < Ts - 13$.

ii) MI is the percentage of pixels such that $2 \text{ km} < HT \leq 6 \text{ km}$.

iii) HI is the percentage of pixels with $HT > 6$ km.

From the above definitions, it is clear that CF = LO + MI + HI. To avoid redundancy, all four cloud fraction features were never used together.

3.2.2 Visible reflectance features (AL, LR)

The mean cloud albedo, AL, is computed over the cloudy pixels (not the entire scene). The mean value of the digital count squared over all cloudy pixels, Gs, is first calculated (Eq. 3.5 below). Then the value of AL is obtained from Eq. 3.6. Designating the number of pixels in the visible histogram with grey count i by hv(i), we can state formally that:

$$Gs = \sum_{i=Dc,255} i^2 \, hv(i) \; / \sum_{i=Dc,255} hv(i) \qquad (3.5)$$

$$AL = (a'Gs + b')/(Io \cos(\zeta)) \qquad (3.6)$$

A second albedo related feature used in this study is the percen-

tage of the cloud fraction for which the pixels have a reflectance below Dc*. Obviously this number, LR (for low reflectance) is zero if the visible mode is taken since in this case Dc = Dc*. Formally, for Dc < Dc*:

$$LR = \sum_{i=Dc,Dc^*} \{i\ hv(i)\} \ / \ \sum_{i=Dc,255} \{i\ hv(i)\} \qquad (3.7)$$

The feature LR is most useful in detecting thin cirrus clouds.

3.2.3 Multilayer index (ML)

A simple multilayer index feature, ML, proved very useful for quantifying the degree of multilayering in a cloud field. As will be shown in section 3.4, mutilayered systems are present about 40% of the time and this importance is reflected in our classification by several multilayered classes (14 to 18).

The multilayer index is defined as the percentage of the cloud field with height 2 km or less below the cloud top height HT. Defining g(z) as the grey level corresponding to height z and hir(i) as the number of pixels with grey level i in the IR histogram, ML is defined as:

$$ML = \sum_{i=g_1,255} hir(i) \ / \ \sum_{i=g_2,255} hir(i) \qquad (3.8)$$

$$g_1 = g(HT-2km) \ ; \quad g_2 = g(z(Tb))$$

Thus a single layer cloud field, by definition, is one with all of its cloudy elements within a 2 km thickness slab in the atmosphere with an upper limit approximately at the cloud top (in fact the upper limit is the coldest pixel, we recall that 3% of the pixels correspond to an

apparent height above HT). Cloud fields with ML < 0.7 correspond to infrared images with significant structure. ML is a good descriptor of the variability of grey tones that one can perceive in the infrared picture. A similar index, defined from z(Tb) and upwards as opposed to HT and downwards could also have been defined. We preferred however to give emphasis to the presence of upper level decks than to lower level decks in our definition of multilayering. For example, a cloud field with CF = 50%, HI= 5% and LO = 45% will have a very low value of ML, ML = HI/(HI+LO) = 0.1, even though 90% of the field belongs to the lower layer.

3.2.4 Connectivity features (NC, CC, BE)

These features are derived from binary images, the black and white pictures corresponding to CF. Pixels with the same color connected only diagonally belong to a different cloud (background) entity whereas pixels with the same color connected to the east, west, north or south neighbors belong to the same cloud (background) entity. The number of clouds, NC, and the number of background areas, NB, are defined in this manner. We then obtain the cloud size distribution as well as the background size distribution. Let us define by hc(i) and hb(j) the number of pixels associated with cloud or background entity i and j, respectively; i = 1, 2...NC and j = 1, 2,...NB. Further let all clouds and background areas be ordered from smallest to largest. Then the cloud connectivity, CC, is defined as:

$$CC = \begin{cases} hc(k)/(mCF) & CF \neq 0 \\ 1 & CF = 0 \end{cases} \qquad (3.9)$$

where k is the cloud entity such that the inequality:

$$\sum_{i=1,k} hc(i) \geq mCF/2$$

is satisfied from the summation of the cloud entities ordered in size. Similarly, the background connectivity, BC, is defined as :

$$BC = \begin{cases} hb(k')/(m(1-CF)) & CF \neq 1 \\ 1 & CF = 1 \end{cases} \qquad (3.10)$$

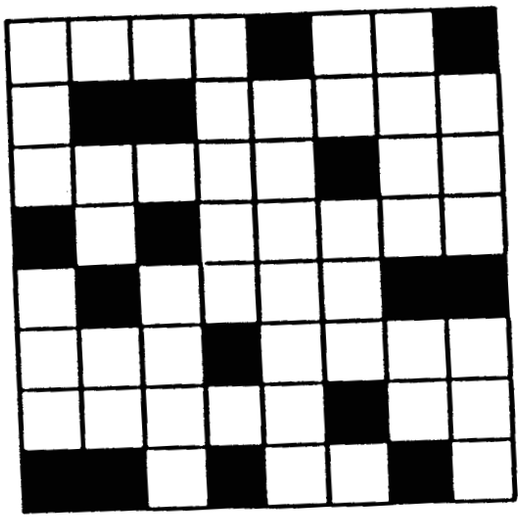
where k' designates the background entity for which the inequality:

$$\sum_{j=1,k'} hb(j) \geq m(1-CF)/2$$

is satisfied from the summation of the background entities ordered in size. Thus in the above equations, hc(k) and hb(k') are the median sizes of the NC clouds and NB backgroud areas, respectively. Fig. 3.2 illustrates the extraction of the connectivity features.

Theoretically, NC (or NB) may reach a maximum value of m/2 (checkerboard pattern). In the present case with m = 4096 and 2 km resolution, the maximum number of clouds encountered was 340. The reader interested in vertical retrievals will find it useful to know the location and size (hb(NB)) of the largest hole in the cloud field obtained here. CC is most useful for differentiating cumulus and stratocumulus with CC smaller for cumulus (highly disconnected elements) and higher for stratocumulus (clouds more highly connected into a few entities). For stratus decks, CC is normally near unity. BC turns out to be a good detector of holes and is notably low for open cells.

a



b

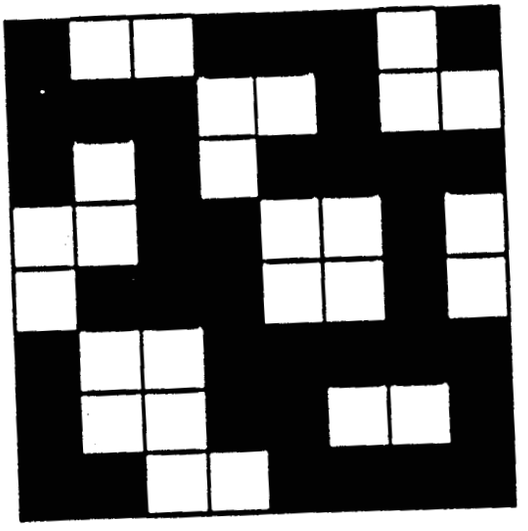


Fig. 3.2 Examples of connectivity indices on an 8 X 8 pixels grid. Clouds are black. a) Simulated cumulus with NC = 13, NB = 1, CC = 1/16 = .063, BC = 1. b) Simulated open cells with NC = 3, NB = 8, CC = 33/38 = .868, BC = 4/26 = .154.

3.2.5 Power spectrum features (ST, SE)

Two-dimensional power spectra are very useful to obtain information on the extended structure of a cloud field, that is on the dominant wavelengths and orientations characterizing it. Garand and Weinman (1986) have provided examples of two-dimensional power spectra taken over cloud areas. Utilizing the same notation as in their paper, the Fourier transform of the image f(k,l) is:

$$Q(u,v) = 1/KL \sum_{k=0}^{K-1} \sum_{l=0}^{L-1} f(k,l)\exp\{-2i\pi(ku/K + lv/L)\} \qquad (3.11)$$

$$u=0,1,\ldots,K-1 \quad ; \quad v=0,1,\ldots,L-1$$

with K,L as spatial dimensions. The power spectrum intensity $PS(u,v) = |Q(u,v)|^2$, is defined as the sum of the squared values of the real and imaginary parts of the Fourier transform (Rosenfeld and Kak (1982)). The orientation, ϕ and wavelength λ associated with any (u,v) component are readily obtained from:

$$\phi = \tan^{-1}(u/v) \qquad (-\pi/2 \leq \phi \leq \pi/2, \text{ off x axis}) \qquad (3.12)$$

and

$$\lambda = S\rho(u^2+v^2)^{-\frac{1}{2}} \qquad (3.13)$$

with ρ the unit resolution of the pixels and S = K = L is the linear dimension in pixels of the scene, assumed square. The power spectrum is symmetric with respect to the origin. It is clear that streaky patterns have streaky power spectra and circular patterns, such as those of open cells, tend to have their dominant components all around the origin. Overcast or clear fields will tend to have all the energy at or near the origin (infinite wavelength). From this experience, a

streakiness factor is defined in the following manner:

i) Find the maximum value, PSm of PS(u,v), $(u,v) \neq (0,0)$.

ii) Threshold all values of PS(u,v) below 20% of PSm to zero. This eliminates the influence of high frequency components which are irrelevant to the appearance of the mesoscale morphologies and contribute only to local grey tone variability. To eliminate a possible false peak due to having one of the eight sensors off (producing horizontal stripes), the component corresponding to such 8 km periodicity (the (0, 16) in our case as derived from (3.13)) is set to zero.

iii) From this thresholded power spectrum, estimate the absolute value of the correlation coefficient, weighted by PS(u,v), as a measure of streakiness:

$$ST = |Sxy| \; / \; (SxSy)^{\frac{1}{2}} \tag{3.14}$$

with: $Sy = \sum_u \sum_v v^2 PS(u,v)$, $Sxy = \sum_u \sum_v uv PS(u,v)$, $Sx = \sum_u \sum_v u^2 PS(u,v)$,

$$u=0,1,\ldots S-1 \; ; \; v=0,1,\ldots S-1 \; ; \; (u,v) \neq (0,0) \; .$$

Recognizing that if the pattern is oriented in the north-south or east-west direction, the measure is misleading as ST = 0, ST is also evaluated from a set of axis rotated 45 degrees from the nominal set and the maximum of the two estimates of ST is retained. ST is an essential feature for the detection of directional patterns: classes 7 and 8.

Observation of open cellular patterns have shown that the typical size of open cells is 30 km (Agee and Dowel (1976), Beniston (1985)). Considering this, we designed our second power spectrum feature, SE for

spectrum energy or intensity, to be the fraction of intensity in the power spectrum characterized by wavelengths between 20 and 40km. Let the radius rd in the power spectrum be defined as:

$$rd = (u^2 + v^2)^{\frac{1}{2}} \tag{3.15}$$

then, defining TE as the total intensity in the power spectrum, excluding the (0,0) component (which represents the mean grey level) SE is defined as:

$$SE = \sum_{u'} \sum_{v'} PS(u'v')/TE \tag{3.16}$$

with (u',v') such that: $rd_1 < rd(u',v') < rd_2$

The thresholds that we used in rd are 3.1 and 6.1 corresponding to wavelengths of 41.3 km and 21.0 km, respectively, from Eq. (3.13). The value of SE turned out to be clearly higher for open cellular patterns, classes 9 and 10, as opposed to all other classes.

Bunting and Fournier (1980) were among the first to test spectral classifiers. Their results were somewhat disappointing: an accuracy of 46% for a 6-class scheme. Later, their work was pursued by Logan et al. (1983). Our experience reveals that power spectra do reveal unique information on the mesoscale organization; however, it is not a good idea to rely uniquely on such features. In near overcast situations, power spectra reveal little information.

3.2.6 Feature extraction example

ORIGINAL PAGE IS
OF POOR QUALITY

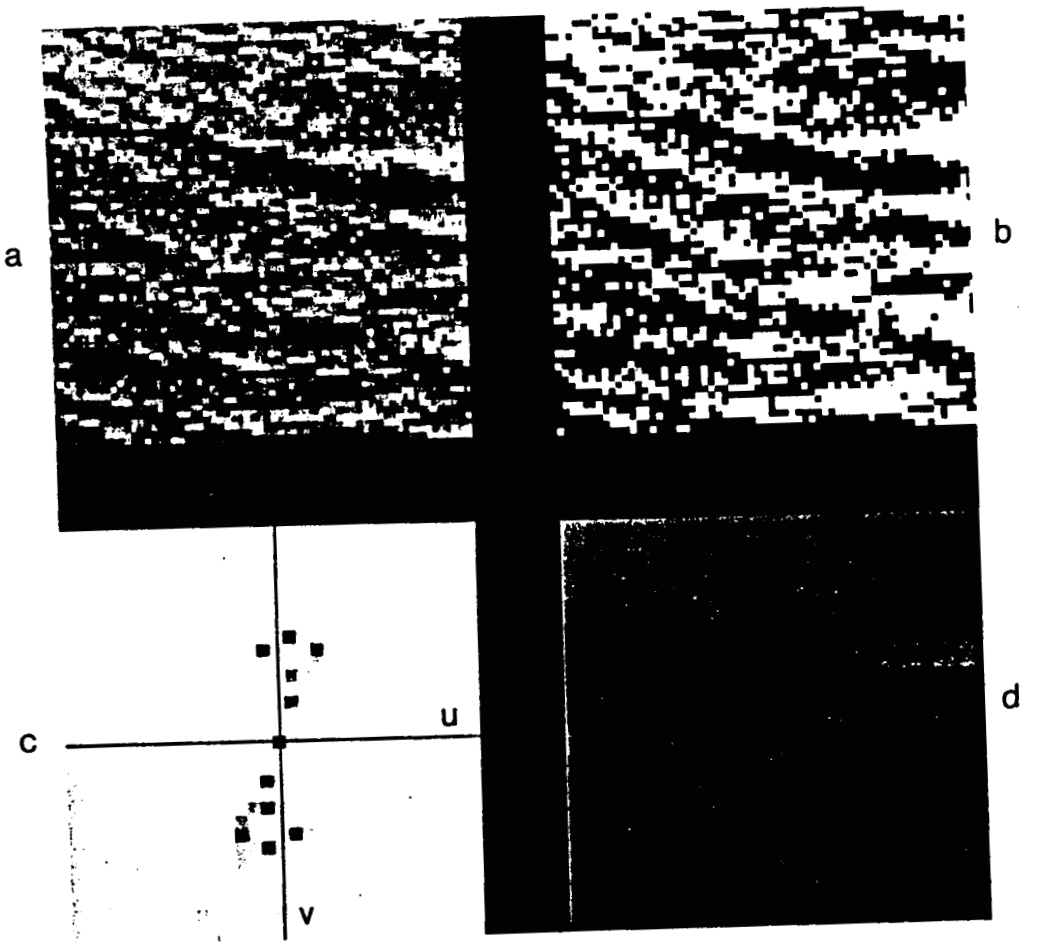


Fig. 3.3 Example of a cloud field belonging to class 7 (cloud streets) with parameters: CF = .363, LO = .320, MI = .043, HI = 0, HT = 2.33 km, LR = 0, AL = .581, NC = 179, ML = 1, BC = .208, CC =. 036, ST = .915, SE = .228, Tb = 280.5 K Ts = 288.2 K. The four images are : a) visible, b) binary, C) power spectrum of the visible image (only the 32 X 32 center portion of the 64 X 64 spectrum is shown) and d) infrared.

Fig. (3.3) shows an example of the visible, infrared, binary and power spectrum images for a cloud field along with the 13 features (see Table 3.1) extracted from those images. The sample is a typical class 7 field (cloud streets). The field is single layered, has a high streakiness factor and correspondingly a streaky power spectrum and numerous small clouds which result in a low cloud connectivity.

The quality of the thresholding procedure to obtain the cloud fraction can be appreciated by comparing the visible and binary images. The major component at (1, 8) in the power spectrum corresponds to an orientation of -7 degrees off the x axis and a wavelength of 16 km from Eqs. (3.12) and (3.13), in agreement with the hard copy image.

Except for CF = 0 indicating class 1, no one feature, alone is decisive in inferring a class. Together however, this set of features is very powerful, as we are about to demonstrate.

3.3 Classification methodology and results

3.3.1 Multivariate Gaussian discriminant function

A sample is defined by its features. Let x represent the vector of features and c the number of classes. A common way to design a classifier (Duda and Hart, 1973) is to opt for some discriminant function $g_i(x)$, i=1,...c and to assign the sample to class i if

$$g_i(\vec{x}) > g_j(\vec{x}) \quad \text{for all } j \neq i \tag{3.17}$$

Due to its analytical tractability, the multivariate normal (or Gaussian) density is the most widely used discriminant function. The

general multivariate normal density is written as:

$$p_i(\vec{x}) = \frac{1}{(2\pi)^{d/2}\,|\Sigma_i|^{\frac{1}{2}}} \exp\{-\tfrac{1}{2}(\vec{x}-\vec{\mu}_i)^T\,\Sigma_i^{-1}(\vec{x}-\vec{\mu}_i)\} \qquad (3.18)$$

where $\vec{\mu}_i = \underset{\vec{x}\,\epsilon\,X_i}{E}(\vec{x})$ and $\Sigma_i = \underset{\vec{x}\,\epsilon\,X_i}{E}[(\vec{x}-\vec{\mu}_i)(\vec{x}-\vec{\mu}_i)^T]$

with E the expected value operator and X_i the ensemble of samples belonging to class i. In Eq. (3.18), d is the number of features or dimensionality, μ_i is the d-dimensional mean vector of the features and Σ_i is the d X d covariance matrix. Σ_i is symmetric and positive definite. Thus, such a classifier is completely defined by μ_i and Σ_i for each class i with $g_i(x) = p_i(x)$ used in Eq. (3.17). The notation $Y = N(\mu_i, \Sigma_i)$ indicates that the vector Y belongs to a multivariate normal population characterized by μ_i and Σ_i. This type of classifier is the basis of our classification algorithm to be described in section 3.3.3.

3.3.2 Theoretical separability estimates from Monte Carlo simulations

A very useful tool to test the theoretical separability of the data is to generate artificial samples, that is, sample populations for each class having the same mean and covariance matrix as the real data. These artificial samples are then classified by using Eq. (3.18) in Eq. (3.17). The result is an upper limit to the separability of the classifier. If this limit increases as we change the features, it means that the new choice of features is more appropriate. If on the

other hand the theoretical limit decreases while the apparent separability of the real data increases, this is an indication of 'overfitting' and results on independent data are prone to be poorer than those claimed from the training set. If we decompose the covariance matrix Σ_i into the lower triangular matrix A such that $AA^T = \Sigma_i$ (Martin et al., 1965), a vector Y belonging to the desired distribution $N(\mu_i, \Sigma_i)$ is generated from:

$$Y = A\vec{r} + \vec{\mu_i} \qquad (3.\text{13})$$

(Scheur and Stoller, 1962) with each of the d components of $\vec{r}$ obtained from an ordinary univariate Gaussian random generator belonging to N(0,1). We used the Box-Muller method (see Forsythe et al, 1973, chapter 10).

3.3.3 Classification algorithm and results on a dependent data set

The classification process was supervised in this study. In supervised classification, the analyst labels each sample with a class number and trains the classifier to assign the proper class. The algorithm is built in two stages, as shown in Fig. 3.4. In Stage 1, the sample is assigned a temporary class using a multivariate normal discriminant function. Thus, Stage 1 is a one-step method as opposed to a hierarchical method. For that reason, it is very efficient as well as simple. Stage 2 has an error-correcting function only, that is, the result of Stage 1 is checked according to some simple criteria based on

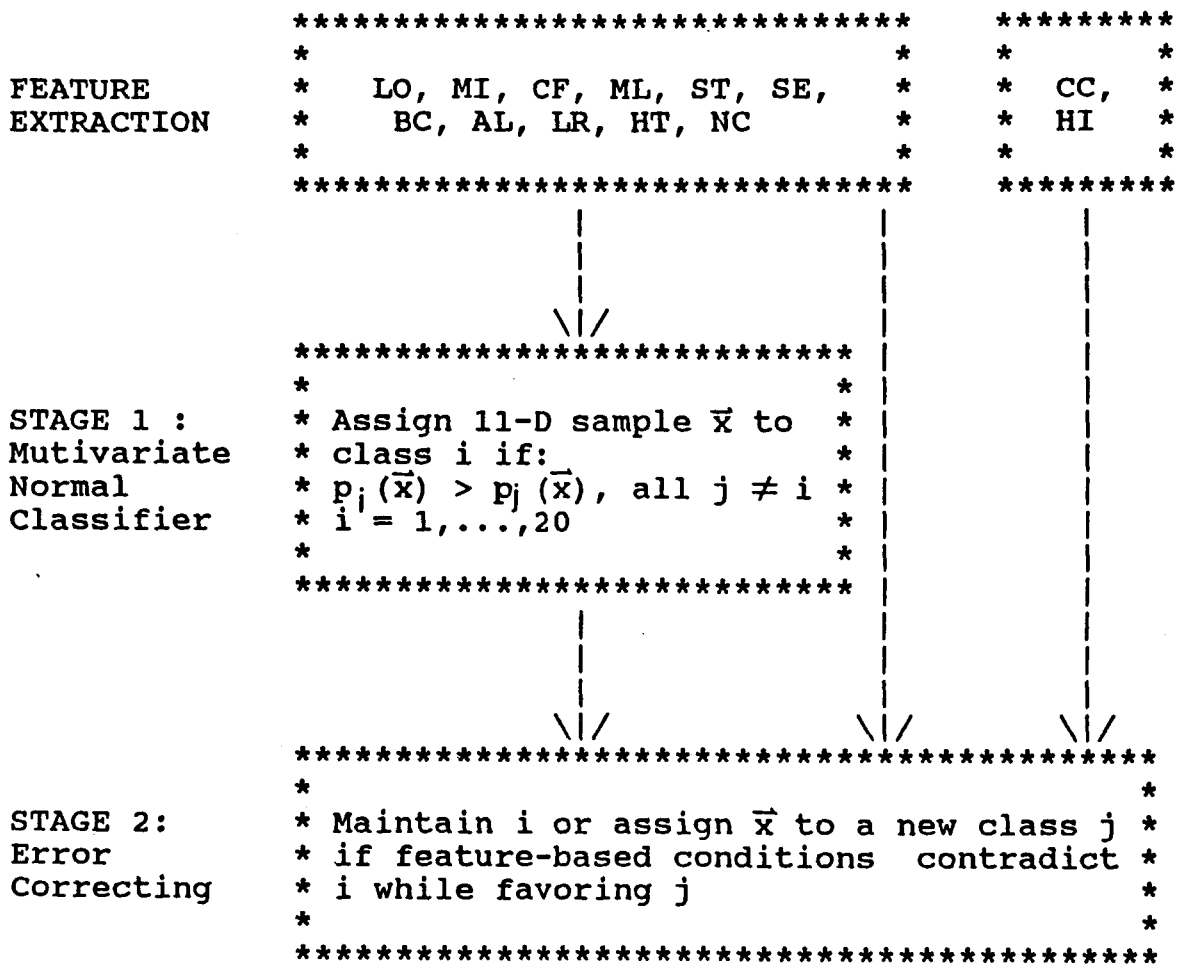


Fig. 3.4 Supervised classification scheme designed for this study.

the most discriminatory feature(s) between the class found in Stage 1 and the class that was selected second best. Stage 2 was designed after it was realized that the vast majority of errors were samples that belonged to the second best choice from Eq. (3.17). This was fortunate for it saved much effort in trying to find the ultimate tree structure. With 13 features and 20 classes, the number of possible combinations is enormous. A revealing example of this situation is the work of Mui and Fu (1980) on automated classification of nucleated blood cells in 17 classes.

a) Stage 1

A summary of the classes assigned to the 5845 samples extracted from February 1984 pictures revealed that most classes had at least 100 samples. From images taken in January 1984 over the same region, a small set (96) of extra samples were taken so that each class now had over 100 samples. Then, exactly 100 samples per class were randomly selected to define a training set of 2000 samples.

In order for all the features to have similar weight, they were normalized to zero mean and unit variance. The means of the features and their standard deviations over all the 2000 samples are given in Table 3.2. The feature vector x is transformed to x, its normalized version, through:

$$\vec{x} = (\vec{x} - \vec{\mu}^*)/\vec{\sigma}^* \qquad (3.20)$$

with $\vec{\mu}^*$ and $\vec{\sigma}^*$ being the means and standard deviations listed in Table 3.2. For the remaining part of this study, the feature vector $\vec{x}$,

Table 3.2 Means and standard deviations of the 13 features for the ensemble of 2000 samples forming the dependent data set.

Feature	Mean	Stand. dev.
ST	.5595	.2684
SE	.1821	.1571
AL	.5165	.1977
HT	4.7470	2.9740
BC	.5781	.3665
LO	.1600	.2258
MI	.3843	.3394
ML	.8127	.2776
CF	.6760	.3222
NC	30.58	41.08
LR	.0479	.1361
CC	.7944	.3147
HI	.1317	.2842

refers to the normalized feature vector and the circumflex accent is dropped. Table 3.2 was obtained following the final labeling of the samples (not the initial one with 100 samples per class). The features are not normally distributed over the ensemble of the data. This is not a problem since the only concern is that the assumption of normal distributions holds for the features within each class.

Extensive tests were made to find out the optimum set of features to be used collectively in Eq. (3.18). A useful criterion is the divergence D_{ijk} between two classes i and j for feature k:

$$D_{ijk} = \frac{|\mu_{ik} - \mu_{jk}|}{\sigma_{ik} + \sigma_{jk}} \tag{3.21}$$

It is easy to see (from the overlap of circular areas centered at μ_{ik} and μ_{jk} and of radius σ_{ik} and σ_{jk}, respectively) that a feature with $D_{ijk} > 1$ has discriminatory skill whereas one with $D_{ijk} < 0.5$ has poor separating power. Another useful tool in selecting the features is their correlation coefficient between themselves over the ensemble of data, as shown in Table 3.3. Only one out of two or more highly correlated features ($r > 0.7$) is retained. Using the divergence criterion, the information from Table 3.3 (and similar information from other features being investigated) along with Monte Carlo testing of the separability, we ultimately found an optimal set of features to be used in Stage 1. The number of features in the set is 11; they are ST, SE, AL, HT, BC, LO, MI, ML, CF, NC and LR. The other two features defined in chapter 2, CC and HI, will be used in Stage 2 only. One can see from Table 3.3 that the maximum correlation between any two features among the eleven selected for Stage 1 is 0.63 only. Most

	ST	SE	AL	HT	BC	LO	MI	ML	CF	NC	LR	CC
SE	-0.01											
AL	-0.03	-0.04										
HT	-0.11	-0.16	0.31									
BC	0.03	-0.23	-0.14	-0.11								
LO	0.09	-0.01	0.01	-0.44	-0.04							
MI	-0.08	0.09	0.38	0.15	-0.54	-0.35						
ML	0.09	0.04	0.06	-0.47	0.17	0.15	-0.32					
CF	-0.07	-0.10	0.63	0.57	-0.49	0.05	0.58	-0.26				
NC	0.10	0.13	-0.36	-0.36	0.18	0.20	-0.37	0.14	-0.50			
LR	-0.01	-0.03	-0.41	0.14	-0.11	-0.13	0.18	-0.37	0.06	-0.02		
CC	-0.10	-0.14	0.46	0.43	-0.46	-0.04	0.50	-0.21	0.76	-0.68	0.07	
HI	-0.05	-0.21	0.26	0.81	0.12	-0.31	-0.25	-0.03	0.40	-0.29	-0.05	0.29

Table 33 Correlation coefficient between the features over the ensemble of 2000 samples of the training set. CC and HI are used in Stage 2 only.

correlation coefficients are very low indicating minimal redundancy.

For the boundary layer classes, numerical instability may occur when inverting the feature covariance matrix as CF = LO + MI exactly for all the samples of the class (HI = 0). This problem is easily solved by adding Gaussian noise in the proportion of one tenth of a percent to CF. In this manner, all covariance matrices are invertible. In addition, for some classes, a particular feature may be a constant resulting in a zero element on the diagonal of the covariance matrix. For example, ML = 1 for all samples of classes 1 to 7. Again, this is easily solved by not allowing the diagonal elements of the covariance matrix to be below a preset minimum value; the value selected is 0.005. This is equivalent to adding noise to that feature in the proportion of 0.7% of one standard deviation (recall that all features have unit standard deviation over the ensemble of data) and therefore this procedure does not affect the separability.

The first result was a separability of 54%. This was disappointing as we knew from unsupervised classification testing (where the computer defines classes with means as separated as possible, see Garand (1986, Appendix A) or Duda and Hart (1973, section 6.9)) that 97% separability could be achieved from the selected set of 11 features. We found that the cause of the low separability was simply imperfect labeling of the samples. Indeed, with twenty classes, many border-line cases are to be expected and subjective decisions based on height and albedo characteristics are subject to error. Thus a good "truth" set is difficult to build from the subjective judgement of

nephanalysts alone. Therefore, we adopted the following man-computer interactive relabeling procedure, a methodology where the human still supervises the labeling process, but is helped in his task by objective measures extracted by the computer:

i) Print the identification number of all incorrectly classified samples, their actual class number and in which class they are apparently misclassified. From the hard copy images, decide if relabeling is desirable. Examine the printout of the features to understand the logic of the classifier.

ii) Resubmit. If the separability still increases, both from the actual data and from Monte Carlo simulations based on the updated means and covariance matrices, go back to i.

The first iterations represent long hours of work as each of the few hundreds misclassified samples was considered individually. Examination of the features often proves useful since each feature provides a different way of considering the sample. The first iterations rapidly increases the separability. As the iterations progressed, the analyst was training himself in defining precisely what was previously all subjective, clarifying all the decision thresholds. Theoretical separability topped at about 95% while actual separability topped near 83%. It was realized that trying to go beyond that result led to overfitting.

As was previously mentioned, it turned out that 85% of the misclassified samples were the second choice of the classifier. This led to the error-correcting Stage 2.

2) Stage 2

The second and final stage was appended to Stage 1 resulting in a new series of iterations. Let C1 be the first choice of the normal density classifier, in other words the result of Stage 1 and let C2 be the second best choice. Based on at most two features, a decision is made to change or not or not to change the result to C2. In Stage 1, using all 11 features together led to some errors because for most pairs of classes, only 1 to a few features are required. The others are irrelevant. We opted for a simple decision rule that did not require new storage of constants: assign the sample belonging to class i = C1 to class j = C2 if:

$$\sum_{k=1,kmax} \frac{(x_k - \mu_{ik})^2}{\sigma_{ik}^2} > \sum_{k=1,kmax} \frac{(x_k - \mu_{jk})^2}{\sigma_{jk}^2} \qquad (3.22)$$

where k is a feature identifier and kmax is either 1 or 2. Table 3.4 shows the features used in Stage 2 for all pairs (C1, C2) to decide between C1 and C2. Where there is no entry, Eq. (3.22) is skipped. This is based on experience that either the ambiguity C1 versus C2 never occurs or that no improvement in their separability can be achieved from Eq. (3.22). Where the entry in Table 3.4 is symmetric, only one feature is used (kmax = 1) and where it is not symmetric, two features are used (kmax = 2). For example, an ambiguity between classes 2 and 12 is resolved from features HT and LO. The reader may appreciate that the feature(s) selected in Table 3.4 are the most relevant to the pair (C1,C2) considered. Note that Eq. (3.22) is executed regardless of how large the ratio $p_{C1}(\vec{x})/p_{C2}(\vec{x})$ may be from

	1	2	3	4	5	6	7	8	9	10	11	12	13	14	15	16	17	18	19	20
1	--	--	CF	--	CF	--	--	--	--	--	--	--	--	--	--	--	--	--	--	--
2	--	--	--	--	--	--	--	--	--	--	LO	LO	--	--	--	--	--	--	--	--
3	CF	--	--	CF	CC	--	ST	--	BC	--	--	--	MI	--	--	--	--	--	--	--
4	--	--	CF	--	--	--	--	--	--	--	--	--	MI	MI	--	--	--	--	--	--
5	CF	--	CC	--	--	CF	--	--	SE	--	--	--	HT	HT	HT	--	--	--	--	--
6	--	--	--	--	CF	--	ST	ST	--	BC	HT	AL	HT	HT	HT	--	--	--	--	--
7	--	--	ST	--	--	MI	--	AL	SE	--	--	--	--	--	--	LO	--	--	--	--
8	--	--	--	--	--	AL	MI	--	--	ST	ST	--	--	--	--	--	--	--	--	--
9	--	--	BC	--	SE	--	ST	--	--	BC	--	--	--	--	--	--	--	--	--	--
10	--	--	--	--	--	BC	--	BC	MI	--	BC	--	--	--	SE	AL	--	--	--	--
11	--	CC	--	--	--	AL	--	BC	--	SE	--	CF	AL	--	--	--	--	--	--	--
12	--	HT	--	--	--	NC	--	--	--	--	CF	--	HT	--	ML	--	--	--	--	--
13	--	--	MI	MI	HT	HT	--	--	--	--	AL	AL	--	--	ML	--	HI	HI	--	--
14	--	--	--	MI	HT	HT	--	--	--	--	--	--	--	--	LO	HT	HT	HI	--	--
15	--	--	--	--	HT	HT	--	--	--	SE	--	ML	ML	LO	--	--	HT	HI	--	--
16	--	--	--	--	--	--	ST	--	--	AL	--	--	--	LR	--	--	AL	AL	--	--
17	--	--	--	--	--	--	--	--	--	--	--	--	HI	HI	HI	HT	--	AL	ML	AL
18	--	--	--	--	--	--	--	--	--	--	--	--	HI	HT	HI	AL	AL	--	HI	ML
19	--	--	--	--	--	--	--	--	--	--	--	--	--	--	--	--	HI	AL	--	AL
20	--	--	--	--	--	--	--	--	--	--	--	--	--	--	--	--	HI	HI	AL	--

Table 3.4 Features used in Eq. (3.22) of Stage 2 for pairs of classes C1 and C2. No entry: Eq. (3.22) is skipped; symmetric entry: one feature is used; non symmetric entry: two features are used.

Table 3.5 Sequence of conditional statements defining Stage 2. The decision on the right is executed if the statement is satisfied. C: class, C1: class chosen from Stage 1; C2: 2nd best class from Stage 1; E: exit Stage 2.

nb	Conditional statement	Decision
1	C1 = 1, CF > 0.01	C = C2, E
2	CF < 0.01	C = 1, E
3	C1 = 4, C2 = 7, ST > 0.5	C = 7, E
4	C1 = 9, C2 = 14 or 15, SE < 0.1	C = C2, E
5	Eq. (3.26) satisfied	C = C2
6	C = 9, ST > 0.9	C = 8, E
7	C = 7, ST < 0.5	C = 3, go to 19
8	C = 5, 6 or 11, BC > 0.9, CC > .85 and HT < 2km	C = 2, E
9	C = 5 or 6, AL > 0.6	C = 11, E
10	C = 5 or 6, HT > 3.5km	C = 13, E
11	C = 14 or 15, HT > 6km, AL > .55	C = 18, go to 23
12	C = 14 or 15, HT > 6km, AL < .55	C = 17, go to 22
13	C = 6 or 13, HT < 3km, BC < 0.1	C = 4, go to 20
14	C = 10, AL < 0.3	C = 9
15	C = 9, CF < 0.2	C = 5, E
16	C = 5, CF > 0.5	C = 6
17	C = 6, NC > 80	C = 4, go to 20
18	C = 6, CF < 0.5	C = 5, E
19	C = 3, CF > 0.5	C = 4, E
20	C = 4, CF < 0.5	C = 3, E
21	C = 4, ST > 0.5	C = 7, E
22	C = 17, AL > 0.55	C = 18, E
23	C = 18, AL < 0.55	C = 17, E
24	C = 11 or 12, HT < 1.5km	C = 2, E
25	C = 12, CF < 0.85	C = 11, E
26	C = 11, CF > 0.95	C = 12
27	C = 12, HT > 6km	C = 18
28	C = 18, HI > 0.9, ML > 0.9	C = 20, E
29	C = 17, AL < 0.25	C = 16, E

Stage 1; attempts to improve the results using that ratio failed.

For the sake of elegance and simplicity, it was planned to use only Eq. (3.22) in Stage 2. We found however that by adding simple conditional statements, the result could still be improved. Eq. (3.22) sets decision thresholds. Most of these thresholds are satisfactory. We may however insist on a specified threshold. Usual practice separates scattered from broken fields with a threshold on CF of 50%. Thus we have set that threshold exactly using a conditional statement for pairs of classes (3,4) and (5,6). Similarly we specifically force the clear class to have less than 1% cloud cover. Other statements arise from experience that Eq. (3.22) is not successful with only two features. Note that the sample may be relabeled in a class different than C2. In all, 29 such conditional statements were implemented in Stage 2. There is no room here to comment on each of them but the reader will find the reasoning behind most of these statements fairly obvious. The entire Stage 2 is provided in Table 3.5. The fifth statement corresponds to Eq. (3.22); it is the most important statement since it applies for all C1 values whereas other statements apply for a particular value of C1.

Table 3.6 shows the results after Stage 1 and Table 3.7 provides the final result following Stage 2. An improvement of 11% is gained from the 83% obtained from Stage 1. Stage 2 is particularly beneficial in correcting errors between class pair (3,5) using the new feature CC and errors associated with class 17 using the new feature HI with AL and ML. Errors between pairs (6,7) and (3,7) are corrected by using ST

and the discrimination of open cells from rolls is solved through the combination of their most characteristic feature, namely BC and ST respectively. Comparing the entries on the diagonals of Tables 3.6 and 3.7 reveals that all classes benefit from Stage 2 except a loss of 1 sample for classes 4 and 14 and a loss of 2 samples for class 6. Note that systematic errors have disappeared. In the course of the iterations that led to the development of Stage 2, the theoretical separability increased only marginally, from 95% to 97%, whereas the practical separability inceased to 95%. At that point, we considered that our pattern recognition algorithm was final. As depicted in Fig. (3.4), a dominant asset of the classifier is its simplicity. The model is entirely defined by the feature means and covariance matrices for each class presented in Appendix, the definition of Stage 2 from Tables 3.4 and 3.5 and the normalization constants of Table 3.2.

From Table 3.7, the new number of samples in each class varies from 28 in class 4 to 184 in class 17. This represents a substantial change from the initial partition of 100 samples per class. These changes are due not only to labeling errors but also to redefinition of some classes during the analysis process.

Tables 3.8 and 3.9 provide the non-normalized means and standard deviations of the features for each class. Fig. 2.2, the plot of HT versus AL, was based on these tables. Table 3.8 reveals the quality of the features chosen. One to a few features are maximized or minimized in each class. The reader will notice, for example, that the

MACHINE LABELING

HUMAN LABELING	1	2	3	4	5	6	7	8	9	10	11	12	13	14	15	16	17	18	19	20
1	60	0	6	0	0	0	0	0	0	0	0	0	0	0	0	0	0	0	0	0
2	0	54	1	0	2	0	0	0	0	0	0	2	0	0	0	0	0	0	0	0
3	4	0	138	0	12	0	3	0	0	0	0	0	0	0	0	0	0	0	0	0
4	0	0	1	25	0	2	0	0	0	0	0	0	0	0	0	0	0	0	0	0
5	1	0	29	0	96	5	0	0	0	0	0	0	0	0	0	0	0	0	0	0
6	0	0	0	1	1	58	0	0	0	0	1	0	0	0	0	0	0	0	0	0
7	0	1	14	0	3	16	82	1	2	0	1	0	1	0	0	0	0	0	0	0
8	0	0	0	0	1	0	1	75	0	3	6	4	0	0	0	0	0	0	0	0
9	0	0	1	1	9	3	4	2	112	0	1	0	0	2	0	0	0	0	0	0
10	0	0	0	0	0	0	0	4	4	71	5	3	0	0	0	0	0	0	0	0
11	0	0	0	0	0	7	0	7	3	0	114	3	0	1	0	0	0	0	0	0
12	0	1	0	0	0	1	0	1	0	1	13	104	0	0	0	0	0	2	0	0
13	0	0	4	0	5	1	0	0	0	1	2	1	38	1	4	0	0	0	0	0
14	0	0	0	0	0	0	0	0	2	0	0	0	0	55	0	0	0	0	0	0
15	0	0	0	0	0	0	0	0	1	2	0	5	0	6	54	0	0	2	0	0
16	0	0	0	0	0	0	0	0	0	0	0	0	4	2	2	117	6	0	0	0
17	0	0	0	0	0	0	0	0	0	0	0	0	1	3	2	8	121	37	11	1
18	0	0	0	0	0	0	0	0	0	0	0	1	0	1	1	0	1	156	1	4
19	0	0	0	0	0	0	0	0	0	0	0	0	0	0	0	0	0	0	67	1
20	0	0	0	0	0	0	0	0	0	0	0	0	0	0	0	0	0	1	5	69

Table 36 Human versus machine distribution of the 2000 samples of the training set in twenty classes after Stage 1. The diagonal indicates 83.3% correct classification.

MACHINE LABELING

HUMAN LABELING	1	2	3	4	5	6	7	8	9	10	11	12	13	14	15	16	17	18	19	20
1	66	0	0	0	0	0	0	0	0	0	0	0	0	0	0	0	0	0	0	0
2	0	59	0	0	0	0	0	0	0	0	0	0	0	0	0	0	0	0	0	0
3	0	0	152	0	3	0	1	0	0	0	0	0	1	0	0	0	0	0	0	0
4	0	0	0	24	0	2	2	0	0	0	0	0	0	0	0	0	0	0	0	0
5	0	0	5	0	126	0	0	0	0	0	0	0	0	0	0	0	0	0	0	0
6	0	0	0	2	0	56	3	0	0	0	0	0	0	0	0	0	0	0	0	0
7	0	1	0	0	1	0	113	2	2	0	1	0	1	0	0	0	0	0	0	0
8	0	0	0	0	0	0	1	80	0	1	2	6	0	0	0	0	0	0	0	0
9	0	0	1	0	2	1	1	2	121	0	2	0	0	5	0	0	0	0	0	0
10	0	0	0	0	0	0	0	4	1	78	0	4	0	0	0	0	0	0	0	0
11	0	0	0	0	0	2	0	3	3	0	123	3	0	1	0	0	0	0	0	0
12	0	0	0	0	0	1	1	1	0	2	1	115	0	0	0	0	0	2	0	0
13	0	0	3	0	0	0	0	0	0	1	0	1	48	1	3	0	0	0	0	0
14	0	0	0	0	0	0	0	0	0	0	0	0	0	54	3	0	0	0	0	0
15	0	0	0	0	0	0	0	0	0	1	0	0	0	3	66	0	0	0	0	0
16	0	0	0	0	0	0	0	0	0	0	0	0	4	1	2	122	2	0	0	0
17	0	0	0	0	0	0	0	0	0	0	0	0	0	0	0	3	181	0	0	0
18	0	0	0	0	0	0	0	0	0	0	0	0	0	0	0	0	0	165	0	0
19	0	0	0	0	0	0	0	0	0	0	0	0	0	0	0	0	0	0	68	0
20	0	0	0	0	0	0	0	0	0	0	0	0	0	0	0	0	0	0	0	75

Table 3.7 Human versus machine distribution of the 2000 samples of the training set in twenty classes after Stage 2. The diagonal indicates 94.6% correct classification.

	ST	SE	AL	HT	BC	LO	MI	ML	CF	NC	LR	CC	HI
1	0.525	0.152	0.191	0.730	1.000	0.001	0.001	1.000	0.002	2.848	0.000	0.750	0.000
2	0.691	0.094	0.614	1.403	0.743	0.890	0.009	1.000	0.899	4.254	0.000	0.990	0.000
3	0.592	0.219	0.346	1.745	0.968	0.134	0.021	1.000	0.156	76.968	0.000	0.118	0.000
4	0.314	0.192	0.437	2.543	0.318	0.445	0.256	1.000	0.701	71.214	0.016	0.776	0.000
5	0.572	0.157	0.406	2.419	0.903	0.168	0.084	1.000	0.252	42.298	0.000	0.598	0.000
6	0.452	0.166	0.473	2.704	0.516	0.362	0.326	1.000	0.688	32.246	0.000	0.842	0.000
7	0.832	0.200	0.422	2.325	0.426	0.446	0.144	0.998	0.591	90.140	0.023	0.613	0.000
8	0.838	0.249	0.745	3.940	0.262	0.060	0.846	0.978	0.906	12.456	0.000	0.975	0.000
9	0.422	0.361	0.555	3.476	0.353	0.238	0.352	0.877	0.590	56.489	0.000	0.752	0.000
10	0.484	0.422	0.666	4.454	0.065	0.038	0.837	0.895	0.875	8.713	0.043	0.997	0.000
11	0.495	0.129	0.635	3.435	0.475	0.142	0.660	0.980	0.802	16.911	0.000	0.923	0.000
12	0.559	0.108	0.757	3.826	0.591	0.267	0.709	0.829	0.977	2.724	0.000	0.999	0.001
13	0.567	0.155	0.358	4.255	0.757	0.032	0.371	0.965	0.405	39.368	0.066	0.590	0.002
14	0.561	0.207	0.452	4.650	0.568	0.253	0.332	0.421	0.588	59.526	0.000	0.658	0.002
15	0.501	0.128	0.470	5.180	0.477	0.043	0.648	0.545	0.694	21.629	0.072	0.860	0.003
16	0.534	0.171	0.252	5.675	0.558	0.078	0.516	0.459	0.644	37.305	0.455	0.784	0.051
17	0.529	0.142	0.411	8.508	0.417	0.036	0.485	0.492	0.865	14.522	0.111	0.939	0.345
18	0.531	0.146	0.721	8.601	0.590	0.041	0.542	0.470	0.927	6.442	0.000	0.992	0.344
19	0.518	0.115	0.499	10.331	0.633	0.000	0.031	0.972	0.968	3.441	0.000	0.997	0.937
20	0.519	0.071	0.868	10.763	0.953	0.000	0.034	0.970	0.999	1.227	0.000	1.000	0.965

Table 38 Means of the features for each class from the final labeling of the 2000 samples of the training set. Units as in Table 3.1.

	ST	SE	AL	HT	BC	LO	MI	ML	CF	NC	LR	CC	HI
1	0.337	0.157	0.089	0.968	0.000	0.003	0.002	0.000	0.003	4.530	0.000	0.353	0.000
2	0.241	0.099	0.114	0.553	0.319	0.201	0.023	0.000	0.202	5.510	0.000	0.026	0.000
3	0.250	0.147	0.065	0.657	0.062	0.107	0.040	0.000	0.120	52.981	0.000	0.116	0.000
4	0.150	0.116	0.067	0.459	0.307	0.150	0.248	0.000	0.137	53.271	0.062	0.292	0.000
5	0.234	0.126	0.072	0.568	0.142	0.113	0.090	0.000	0.149	24.568	0.000	0.215	0.000
6	0.161	0.116	0.060	0.505	0.268	0.224	0.255	0.000	0.110	18.814	0.000	0.183	0.000
7	0.263	0.149	0.079	0.603	0.327	0.182	0.203	0.015	0.211	66.791	0.084	0.350	0.000
8	0.122	0.191	0.119	0.812	0.276	0.103	0.196	0.050	0.112	23.274	0.000	0.072	0.000
9	0.201	0.150	0.078	0.681	0.287	0.111	0.171	0.161	0.128	32.551	0.000	0.252	0.000
10	0.207	0.163	0.125	0.683	0.038	0.049	0.133	0.130	0.107	6.865	0.103	0.005	0.000
11	0.214	0.119	0.085	0.525	0.309	0.153	0.215	0.042	0.137	13.121	0.000	0.147	0.000
12	0.356	0.115	0.138	1.048	0.365	0.322	0.320	0.279	0.034	2.651	0.000	0.003	0.003
13	0.248	0.131	0.085	0.850	0.326	0.056	0.306	0.064	0.333	34.182	0.132	0.362	0.008
14	0.221	0.141	0.114	0.787	0.315	0.170	0.183	0.230	0.207	50.946	0.000	0.332	0.004
15	0.262	0.121	0.130	0.539	0.335	0.048	0.254	0.188	0.262	17.778	0.131	0.237	0.005
16	0.241	0.125	0.059	1.590	0.352	0.073	0.246	0.282	0.274	32.446	0.167	0.280	0.081
17	0.228	0.114	0.076	1.534	0.289	0.069	0.239	0.247	0.145	20.515	0.142	0.161	0.264
18	0.248	0.130	0.118	1.707	0.328	0.099	0.254	0.234	0.087	8.196	0.000	0.022	0.258
19	0.247	0.105	0.087	0.909	0.323	0.000	0.038	0.036	0.048	4.268	0.000	0.007	0.061
20	0.299	0.104	0.102	1.153	0.150	0.000	0.044	0.038	0.008	1.271	0.000	0.001	0.045

Table 3.9 Standard deviations of the features for each class, corresponding to the means of Table 3.8.

streakiness factor is clearly higher for the directional classes 7 and 8 while SE is also distinctly higher for open cellular patterns, i.e. classes 9 and 10. The background connectivity, BC, is minimized in classes 8, 9 and 10 revealing the presence of holes in those cloud fields. The multilayer index is low in multilayered classes 14 to 18. The cloud connectivity permits ready separation of cumulus and stratocumulus. The detection of thin cirrus is greatly facilitated from feature LR in conjunction with HT. Tables 3.8 and 3.9 are a compact objective description of the classes presented subjectively in Chapter 2.

3.3.4 Results on independent data

In order to test the validity of the pattern recognition algorithm, an independent data set made of 5 images with 204 samples per scene was assembled. Thus, the independent set has a total of 1020 samples, all taken at 18 GMT in 1984. The actual dates are January 8 and 22 and February 7, 8 and 12.

An example of machine classification for January 8, 1984 at 18GMT is provided in Figs. 3.5a,b. We had the data for all days of January at 18 GMT and February at 16 GMT and 18 GMT on tape. Since the dependent set was derived from February, 16 GMT data, it was desirable to consider January data for the independent data set. Three of the days were, however, taken in February 1984 but those scenes differ in time by two hours from those of the training set. The reason for not taking all images of the test set in January was to provide a good representation of all cloud classes from only 5 images. For example, there were

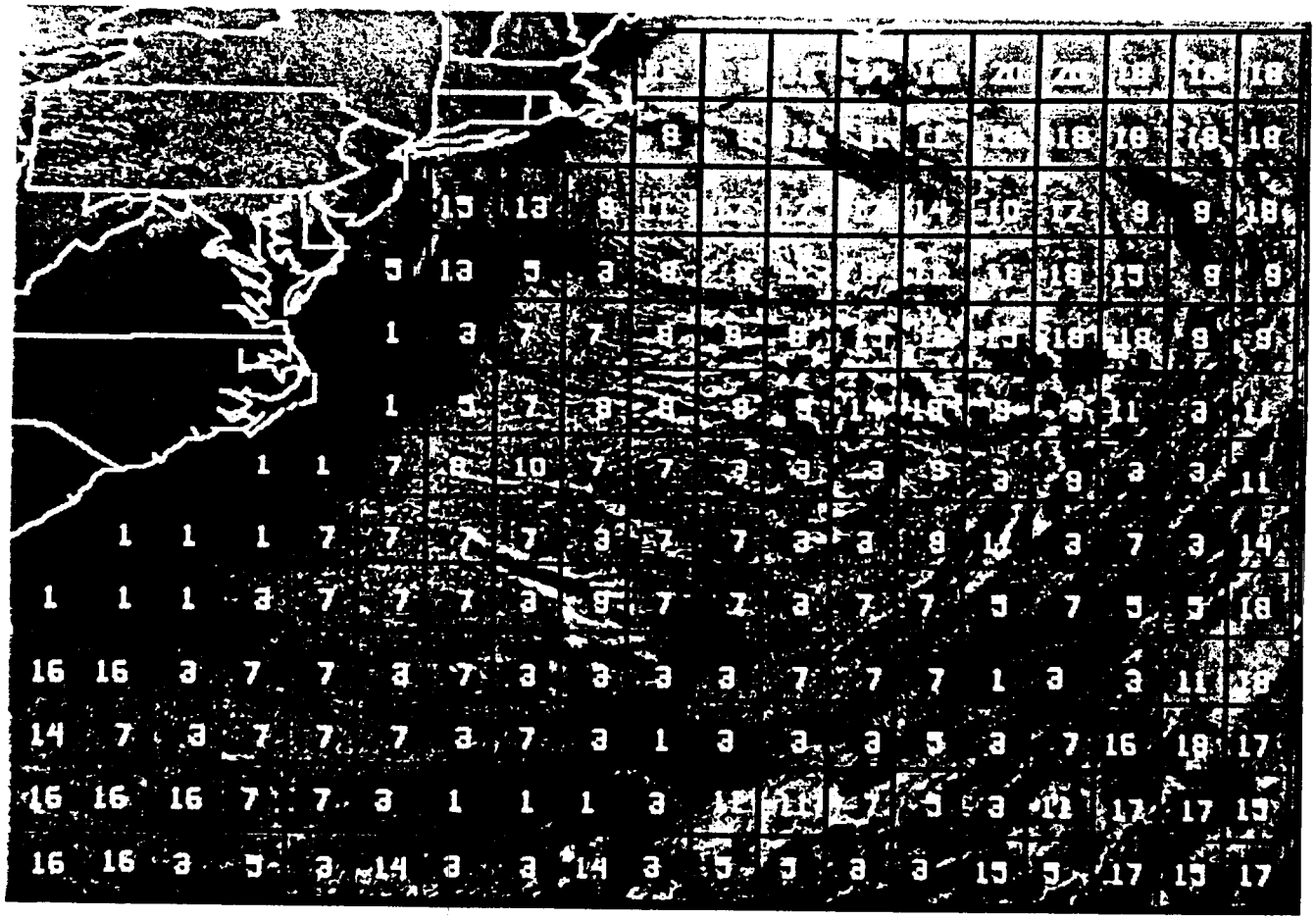


Fig. 3.5a Visible image for January 8, 1984 at 18 GMT with grid of analysis and machine cloud classification number superimposed.

ORIGINAL PAGE IS
OF POOR QUALITY

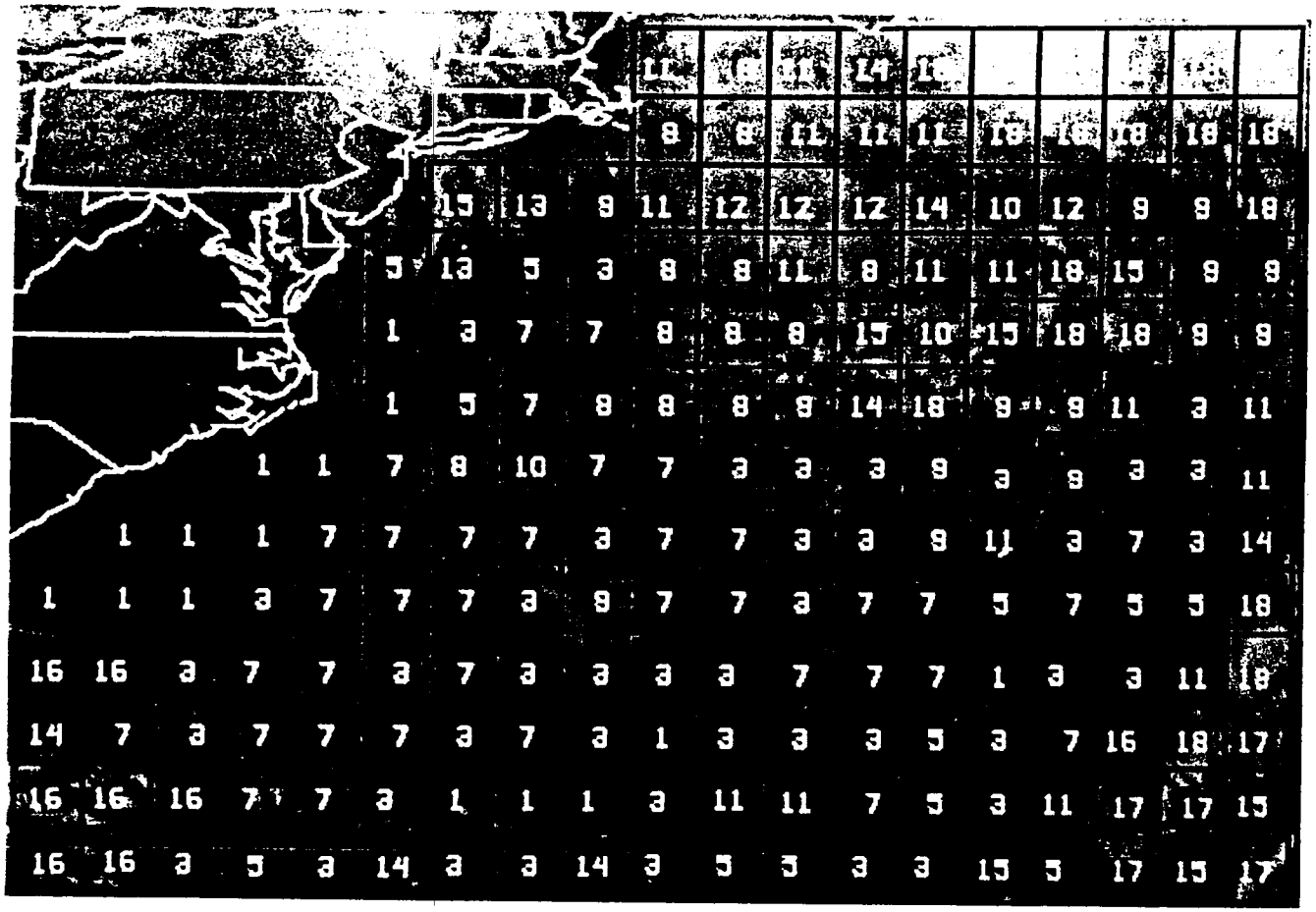


Fig. 3.5b Same as 3.5a, but showing the infrared image.

ORIGINAL PAGE IS
OF POOR QUALITY

no extensive areas of stratus in January (class 2 for which February 12 is a good case) and no extensive areas of open cells (classes 9 and 10 for which February 7 and 8 are good cases). In addition, we recall that only about one third of each image was selected for the training set. Considering those factors, the test set is considered to be at least 80% independent of the training set and all 1020 samples differ from those used in the training set.

In addition to the author, two senior meteorologists worked on the verification to be presented here. Among other credentials, both researchers have had many years of experience analyzing digital visible and infrared GOES imagery. We refer to these consulting analysts as Analyst 1 and Analyst 2. Each analyst worked separately, following the procedure outlined here:

1) The visible and infrared images are displayed on the video screen of MCIDAS. The grid of analysis with 204 grid boxes is superimposed on the images.

2) The analysts have a hard copy of each of the 5 grids with the machine class number assigned by the algorithm in the middle of the box. They also have the worded description of the 20 classes and the examples presented in Section 2. The task is to examine both visible and infrared images for each sample and to correct the computer answer if need be. If they do find an error, the analysts are asked to provide two numbers: the corrected class number and the class number that they feel is second best. The purpose of the second number is to find out how many times the computer has selected the second best

choice.

3) The information provided by each analyst is keyed in the computer to derive statistics.

The results are presented in Tables 3.10 to 3.13. Table 3.10 shows the overall accuracy inferred from each analyst. These results indicate that while the two consulting analysts agreed with an overall accuracy of about 73%, the author was estimating that same statistic considerably higher at 87%. Having designed the classifier, the author certainly had more experience with the particular choice of classes selected while the consulting analysts may have had a different view of what each class is or should be. It may be argued that the author is biassed towards agreeing with the machine result. This argument is partially dismissed upon noting that the author flagged the samples as incorrectly classified while the consulting analysts flagged them as correctly classified for 3.0% of the data set with respect to Analyst 1 and for 5.3% of the data set with respect to Analyst 2. More importanly, Table 3.11 indicates that the consulting analysts agreed on 75.2% of the samples to be either right or wrong. Thus for 24.8% of the samples, one of them flagged the result as right while the other flagged it faulty. Obviously, this means that the machine result for those samples is either right or fairly close; if it is ultimately considered right, the accuracy inferred from the consulting analysts would rise to 83.8%.

The indication that the machine result is virtually always close is provided by Table 3.12. For only 2.9% of the time, all 3 analysts

Table 3.10 Overall accuracy (%) estimated by different analysts for the 1020 samples of the independent data set, with and without considering cases where the machine selects the second best choice.

Analyst	Strictly correct	At least 2nd best
AUTHOR	87.1	95.6
ANALYST 1	73.1	82.5
ANALYST 2	72.3	81.3

Table 3.11 Percentage of agreement between analysts on samples being correctly or incorrectly classified.

	agree correct	agree incorrect	overall agreement
AUTHOR/ANALYST 1	68.1	9.9	78.0
AUTHOR/ANALYST 2	65.0	7.6	72.6
ANALYSTS 1 and 2	59.0	16.2	75.2

Table 3.12 Percentage of the samples for which none, one, two or all three analysts agree that the machine result is right. Results given for strictly correct and for machine result at least second best among twenty classes.

Number of analysts agreeing	0	1	2	3
Stricly correct	6.1	14.8	24.2	54.9
at least 2nd best	2.9	8.2	20.6	68.3

Consensus: at least two analysts agree:

Stricly correct: 79.1
at least 2nd best: 88.9

Table 3.13 Consensus of correct classification for each class. Machine number of samples for each class given next to the number of those samples for which at least two out of three analysts agree with the machine result. Resulting percentage of agreement is shown in right column.

Class	Machine number of samples	Number for which consensus agrees	Percentage of of agreement
1	22	22	100.0
2	20	20	100.0
3	90	89	98.9
4	14	12	85.7
5	41	39	95.1
6	17	17	100.0
7	78	72	92.3
8	79	74	93.7
9	78	60	76.9
10	56	36	64.3
11	102	77	75.5
12	40	30	75.0
13	9	4	44.4
14	30	19	63.3
15	24	19	79.2
16	61	61	100.0
17	72	71	98.6
18	123	122	99.2
19	22	22	100.0
20	42	41	97.6

agree that a sample is incorrectly classified and does not qualify as second best. This results matches the 97% theoretical separability obtained from Monte Carlo simulations. Table 3.12 describes a consensus that we present as our final estimate of the classifier accuracy: two out of three analysts agree that the overall accuracy is 79.1%. If second best choices are considered as correct, the overall accuracy rises to 88.9%. It was previously admitted that the test set could have partial dependence with the training set. The results for the two January days (408 samples which are totally independent from the training set) were very similar to the numbers quoted above: 77.4% stricly correct and 86.7% at least second best. Thus, the results presented in Tables 3.10 to 3.13 are in all likelihood representative.

Table 3.13 presents, class by class, the results of the classification based on this consensus adopted as a method of verification. It is seen that 12 of the 20 classes scored above 90%. Boundary layer classes, including stratus, streets and rolls are particularly well classified as well as high-level cloud classes; in particular, all thin cirrus (class 16) samples detected by the machine were confirmed by the analysts. The result for class 13 (44%) is not representative, being derived from only 9 samples (the result was 85% correct on the dependent set); most of the errors in class 13 are actual cirrus seen as single layered clouds at mid-level. There is a problem in overselecting class 10, convective open cells, when some small holes are present in a mid level overcast. For multilayered classes 14 and 15, an acknowledged problem is their selection when thin

cirrus overrides cumulus or stratocumulus. The machine interprets the higher deck as altocumulus because the apparent height is below 6 km and because the cloud albedo is higher due to the presence of the lower deck. The solution to this problem would probably require an additional spectral channel sensitive to the presence of ice crystals.

The need for an objective method of classification is confirmed by examination of the agreement between the three analysts which is below 79%. We stressed that this agreement is on a single number to be selected as right or wrong. In an experiment prior to the verification experiment described above, Analyst 1 and Analyst 2 were asked, for the same 1020 samples, to label the samples with a class number from 1 to 20, without having the machine result as information (only the description of the classes and the catalog of four examples for each class shown in Garand (1986)). The agreement was surprisingly low: 37% on a strict basis (as opposed to 75% when they were given the machine answer), raising to 55% if their second choice was considered. This result shows once again, this time without leaving any doubt, that objective classification provides results that are more reproducible, less ambiguous than the subjective techniques used in the past.

3.3.5 Computer time

We now examine the computer time required to use the proposed feature extraction and classification scheme. It requires 2.5 s per box on a medium size computer (IBM 4381). Virtually all the time is devoted to feature extraction, the classification taking less than 0.1 s. The most time consuming part, about 1.2 s (it varies with

morphology), goes into the estimation of the connectivity indices as each cloud or background element is catalogued individually. The algorithm is not optimized for efficiency; the author gave only reasonable attention to this aspect. Yet, the 204 boxes of our 20 X 20 degree domain can be classified in about 8.5 minutes. At the scale of $(128\ km)^2$, the entire planet, land and ocean areas included (31130 boxes), could be analyzed in 21 hours with the same computer, if the scheme was generalized for usage over land masses and for all seasons. Optimizing the code and using a larger computer, we hypothesize that a factor of 2 could be gained. Daytime only application leads to another reduction factor of two. Further, a gain by a factor of 3 to 4 would be obtained if it was shown that the results of the classification are not significantly deteriorated from using a resolution of 4 km in the visible as opposed to 2 km. Still, the task is costly for a single computer as maps are desirable every three hours. However, this task is perfectly suited for parallel processors since each box is considered independently from the others. We conclude that, with vectorized machines or cooperation between various satellite data centers, the method could satisfy the time requirements of ISCCP.

4. CLIMATOLOGICAL APPLICATIONS

4.1 Cloud type climatology for January and February 1984 in twenty classes.

Table 4.1 provides the number of occurrences of each cloud type for January and February 1984. Table 4.2 gives the means of conventional cloud parameters for the same period. Although the cloud fraction for the two months was virtually the same, 63%, January was characterized by a value of HI 6.9% higher, compensated by a LO value 5.4% lower than in February. As a consequence, the mean value of HT is higher in January by 700 meters. The mean albedo is similar for the two months. Cumulonimbus cloud classes, 18 and 20, account for 25.1% of the samples in January whereas they account for only 16.5% in February. February was characterized by several cold air outbreaks, including a spectacular event that lasted four days between the 7th and the 10th. As a result, mesoscale cellular patterns (classes 8, 9, 10) are more numerous in February. Stratus, class 2, tend to occur extensively or not at all; extensive stratus occurred February 12 and 13 but no such cases happened in January resulting in a marked discrepancy for that class. Another remarkable result, which applies to both months, is that broken cumulus occurs less than 1% of the time as opposed to 11% for scattered cumulus.

As will be shown in Part 2, each cloud class is associated with a different probability of precipitation. Having a scheme as detailed as this one permits more accuracy than using only global statistics such as those provided in Table 4.2.

Table 4.1 Number of occurrences of each cloud type for January and February 1984, and resulting percentage of occurrence.

	January		February	
Class	nb	%	nb	%
1	325	5.49	289	4.94
2	20	0.34	141	2.41
3	638	10.78	641	10.97
4	29	0.49	50	0.86
5	296	5.00	473	8.09
6	48	0.81	184	3.15
7	190	3.21	166	2.84
8	123	2.08	141	2.41
9	126	2.13	193	3.30
10	53	0.90	112	1.92
11	304	5.14	315	5.39
12	182	3.08	295	5.05
13	113	1.91	149	2.55
14	195	3.30	210	3.59
15	192	3.25	210	3.59
16	662	11.19	412	7.05
17	681	11.51	729	12.47
18	906	15.31	601	10.28
19	257	4.34	170	2.91
20	576	9.74	364	6.23
Total	5916		5845	

Table 4.2 Cloud parameter means for January and February 1984 over the entire domain.

Feature	January	February
CF	0.638	0.630
LO	0.073	0.127
MI	0.327	0.337
HI	0.239	0.170
HT (km)	5.8	5.1
AL	0.526	0.503

Table 4.3a Given a cloud type observed from ship, probability of presence of other cloud types in winter (Dec., Jan., Feb), for the oceanic region bounded by 30-45N latitude and 60-90W longitude (after Hahn et al., 1982). Ac: altocumulus, As: altostratus, Ci: cirrus, Sc: stratocumulus, Cb: cumulonimbus, St: stratus, Cu: cumulus, Ns: nimbostratus. A X indicates a pair of types that are never reported together by observers.

Given	Probability of cooccurrence					
	As/Ac	Ns	Cu	Sc	Cb	None
Cs	60	12	22	44	6	18
As/Ac		0.4	21	58	8	12
Ns			1	63	2	23
Cu				X	X	57
Sc/St					X	40
Cb						48

Table 4.3b Probability of occurrence of each cloud type for same time period and region as in Table 4.3a, and percentage of occurrence alone or not (after Hahn at al., 1982).

Type	% of occurrence	alone	multilayers
Clear	8		
Ci	29	5.2	23.8
As/Ac	39	4.7	34.3
Ns	9	2.1	6.9
Cu	26	14.8	11.2
St/Sc	50	20.0	30.0
Cb	5	2.4	2.6

An attempt was made to compare our results to statistics of cloud type obtained from ships. Hahn et al. (1982) provided a comprehensive study of cooccurrence of cloud types over the ocean, based on twelve years of observations. Fortunately, one of their grid boxes represents the same region as the one studied here. Their results are condensed in Table 4.3. Among other questions, we are interested in knowing the percentage of multilayered systems. According to Table 4.3b, that percentage is 42.8% since single layered cloud fields, including clear sky, occur 57.2% of the time. We assume that cloud classes 1 to 11 and 13 are single layered. From Table 4.3a, if we further assume that cirrus associated classes 16, 17 and 19 are multilayered 82% of the time, nimbostratus (class 12), 77% of the time and cumulonimbus classes (18 and 20) 52% of the time, then, by pooling the data for January and February together, we obtain that 41.1% of the cloud systems are multilayered. This result compares well with the climatological estimate of 42.8% based on ship observations.

Other comparisons are directly possible. The clear class occurred 5% of the time versus 8% from ship climatology. Perhaps, the difference is the result of the scale of analysis, which is much larger from satellite (128 X 128 km) than from the ground (about 40 X 40 km). As another example, Hahn's data suggest that cumulus alone happens 14.8% of the time whereas our limited data yield 14.5%, if classes 3, 4 and 7 are pooled as cumulus-alone classes. A more relevant exercise would be to compare directly coincident satellite versus ship-observed cloud classes, especially multilayered systems. For example, the data

for classes 14 and 15 suggest that altocumulus (Ac) occurs the same proportion of the time with either cumulus (Cu) or stratocumulus (Sc) whereas Table 4.3a reveals that the pair Ac/Sc occurs almost three times more often than the pair Ac/Cu. From such studies, one could fill in, statistically, what the satellite cannot see, namely what is underneath the higher cloud deck.

4.2 Monthly , seasonal maps of cloud fraction

4.2.1 Monthly maps

Figs. 4.1a and 4.1b show the mean cloud fraction for January and February 1984. The interpolation procedure is that of Hibbard and Wylie (1985) and the computer system used is MCIDAS (see Suomi et al., 1983). The maps are produced from 29 satellite measurements for each of the contiguous 204 grid boxes. As seen in the previous section, the overall cloud fraction for the two months was the same. The detail shows noticeable differences, however. January is characterized by a marked north-south gradient, south of latitude 35 N, whereas no such feature occurs in February except in the south-east part of the domain. Both months have a strong maximum (above 80%) in the latitudinal belt 37-40 N south of Nova Scotia. January shows a second maximum of 83% off Cape Hatteras. The extended region of high cloud fraction in January indicates the mean track of the frontal systems that frequently occurred in that month. The lack of gradient of cloud fraction towards the tropics in February may be explained by the few cold air outbreak episodes that penetrated far south.

4.2.2 Seasonal maps and comparison with ship data

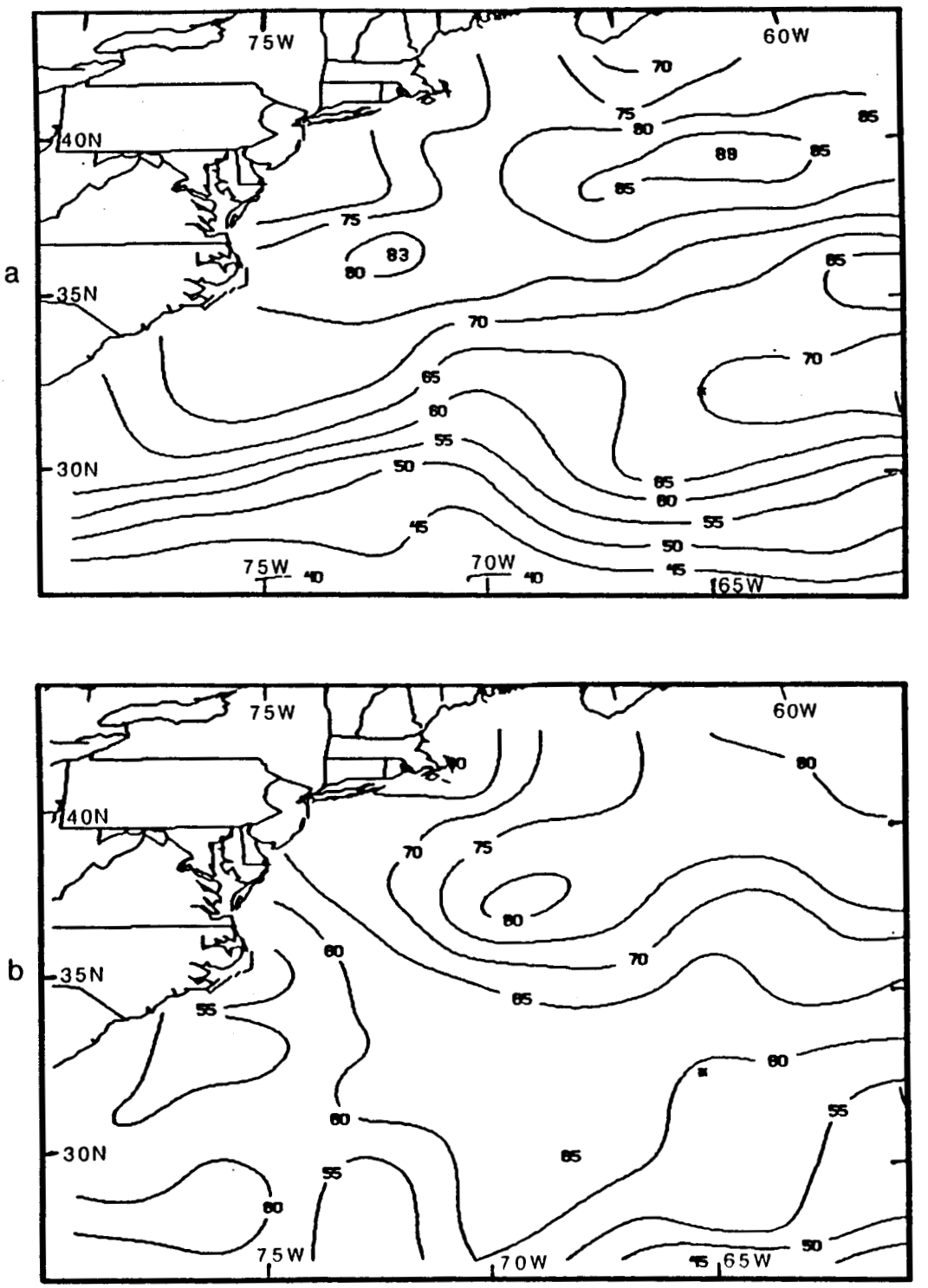


Fig. 4.1 Satellite retrieved mean cloud fraction for: a) January 1984 (N = 5916) and b) February 1984 (N = 5845).

We have compared our estimates of cloud fraction with ship observations. Figs. 4.2a and 4.2b are seasonal maps, with January and February pooled together, of cloud fraction obtained from ships and satellite respectively. These maps are produced from 1275 coincident ship reports and satellite retrievals at 18 GMT. The matching procedure is explained in Part 2. We recall that ground observers report the cloud cover in octas, that is with increments of 0.125. The results show good agreement in the general pattern and its details. However, the cloud fraction observed from ships is often 10 to 20% higher than the satellite estimate. It is a known fact that ground observers overestimate (often by one to two octas) cloud fraction due to angular perspective, especially for low cloud fields with true cloud fraction in the range 30-70%. Minnis and Harrison (1984a) reported similar findings (see also references herein).

Fig. 4.2c presents the satellite retrieved cloud fraction for the two months using all the data (11,761 retrievals). While Figs 4.2b and 4.2c used the same method for the estimation of cloud fraction, Fig. 4.2c was produced with complete sampling: 9.2 times more data samples. The result is a smoother pattern where, in particular, the closed low near Bermuda vanishes. This result emphasizes the need for good sampling and resolution for a geophysical field as variable as cloud fraction. We have presented maps of cloud fraction (CF). Maps of other parameters of interest, such as LO, MI, HI, HT, Ts, Tb and AL are also available from the present method.

C-2

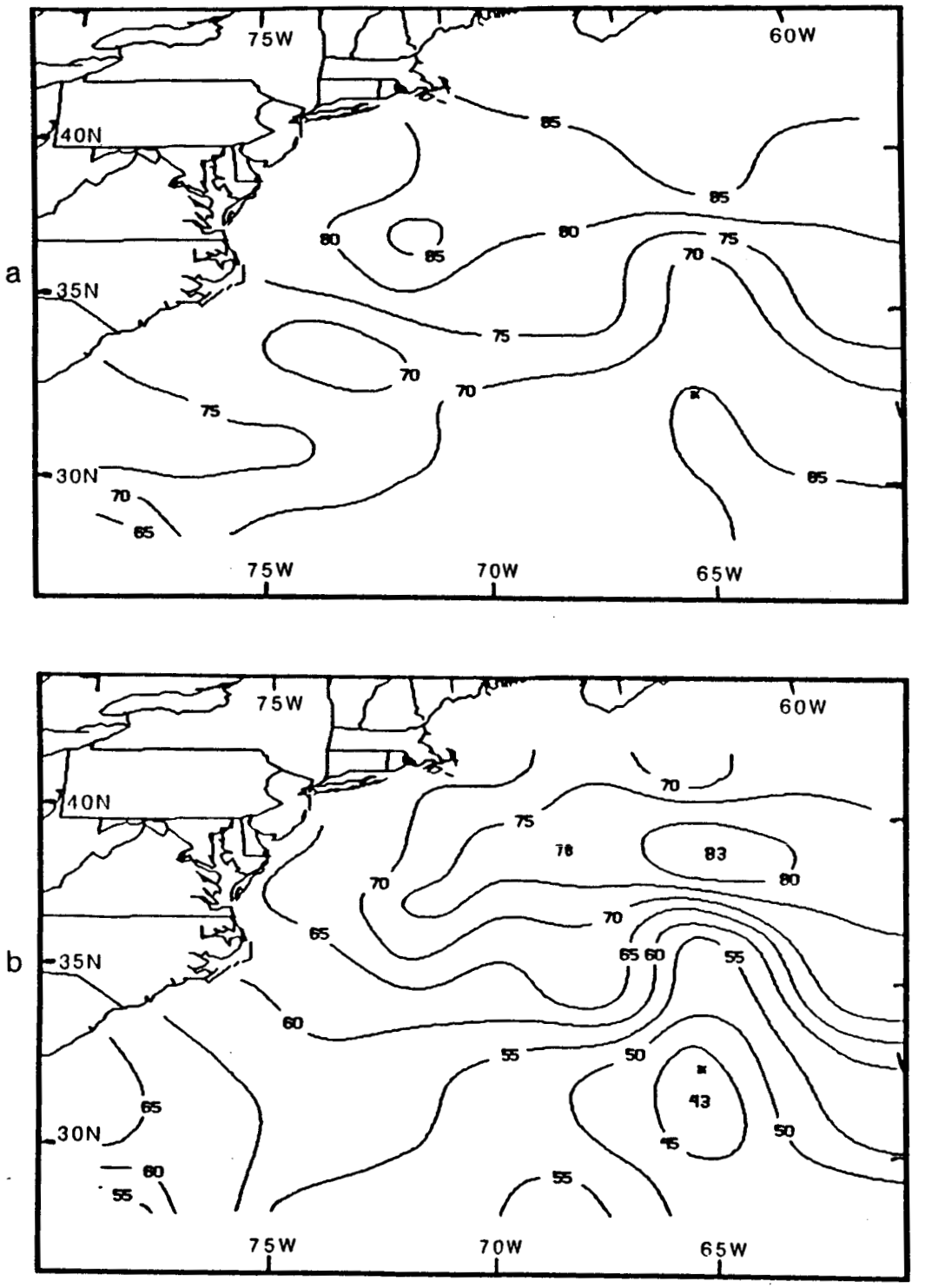


Fig. 4.2 Mean cloud fraction for January + February 1984. a) Observed from ships b) retrieved at the location of the ships (N = 1275, distributed over 32 grid points).

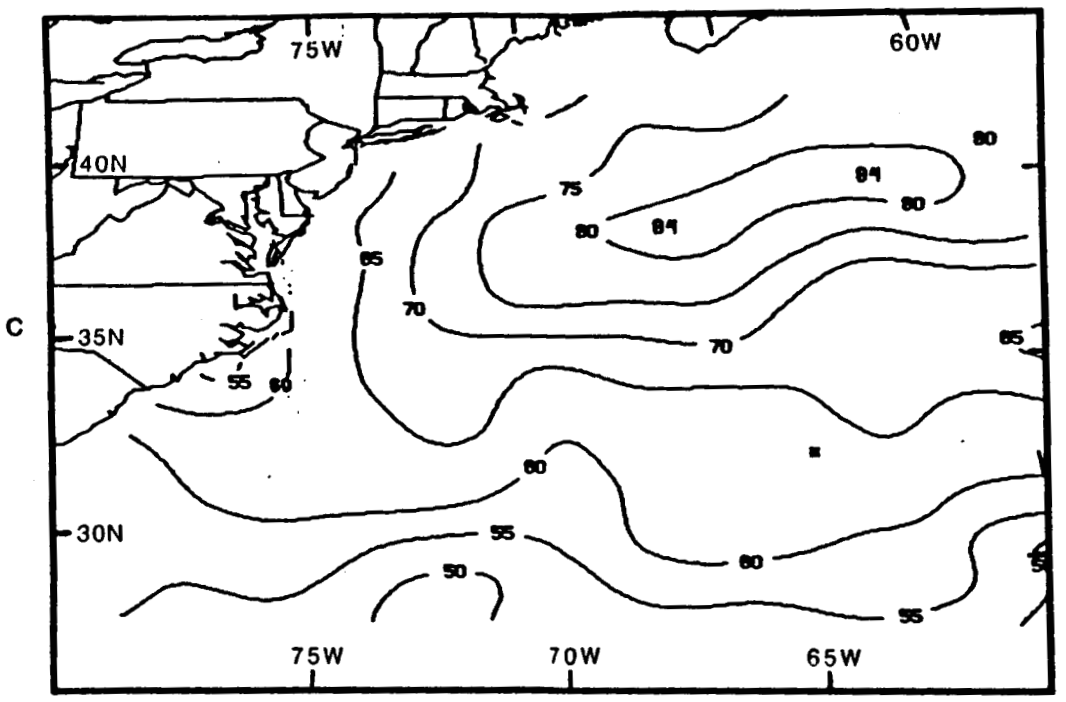


Fig. 4.2 Continued. c) Satellite retrieved mean cloud fraction for January + February 1984 using complete sampling (N = 11761, distributed over 204 grid points).

5. SUMMARY AND CONCLUSION

An automated algorithm to classify clouds in twenty classes has been presented. A novel aspect is the attention given to mesoscale cellular patterns: directional patterns such as cloud streets and rolls are detected (we believe for the first time) as well as open cells from features derived from the two-dimensional power spectrum of the visible images. Multilayered systems, including thin cirrus, are separated into several classes. In addition, cumulus, stratocumulus and stratus are specifically recognized. A consensus of three expert nephanalysts estimated the accuracy of the scheme at 79% with the machine answer at least second best among twenty classes 89% of the time. The classifier itself is very simple. A first stage tentatively assigns a class from a one-step decision rule that finds the class with highest probability of existence, given an eleven-dimensional vector of features. The second and last stage merely corrects possible errors of the first stage based on a small subset of features most relevant to the class selected in the first stage. All the features bear physical meaning, can easily be interpreted with what can be seen from the hard copies. The features provide a detailed description of the cloud field in terms of effective cloud fraction and albedo, height, multilayering, size distribution, shape, directionality strength, existence of holes, connectivity etc... Thus, the classification is quantitative, that is, it does not merely provide a class number but it also provides a set a physical descriptors that can be further utilized.

A comparison was made of the climatologies of twenty cloud classes

for January and February 1984. Significant differences in the distribution of the cloud classes were found in the two months even though the mean cloud fraction and mean albedo were virtually identical. Moreover, the cloud fraction maps for the two months were significantly different despite, as mentioned, the same overall mean cloud fraction.

The cloud classification algorithm should be applicable over all oceans uncovered by ice. Perhaps the classification is too detailed for use over the tropics where, for example, rolls and open cells are rare, but having too many classes is not a problem since related classes can be merged.

The computer time, 2.5 s per 128 X 128 km box (on a medium size computer: IBM 4381) or 8.5 minutes for the 200 boxes of a 20 X 20 degree region, may satisfy the requirements of ISCCP, especially if vectorized machines are used.

The scheme will be used in the First ISCCP Regional Experiment (project FIRE, in 1987) to quantify marine stratocumulus fields off the coast of California. It is also intented to generalize the scheme for use over land. This will require regularly updated maps of surface albedo and knowledge of the surface temperature.

The quantification of cloud fields in terms of fractional coverage, height and albedo is fundamental to the understanding of climate mechanisms. But cloud fields are also spatially organized in recognizable mesoscale morphologies which may be revealing of the physical state of the atmosphere. This aspect is the object of Part 2.

ACKNOWLEDGEMENTS

The author thanks Dr. J. A. Weinman for countless scientific discussions and for revising this text. Drs. Don Wylie and David Martin were very helpful in their quality of expert nephanalysts. The Atmospheric Environment Service of Canada and NASA grant NAG5-580 provided the necessary funding for this work. I thank the staff of the Space Science and Engineering Center (Madison, Wisconsin) and especially its director, Professor Verner Suomi, for all the resources which I had access. The material presented here was developed as a part of the author's Ph.D. dissertation (University of Wisconsin).

APPENDIX. Covariance matrices of the features.

Table A.1 provides the normalized variances of features HI and CC, which may be used in Stage 2 of the classifier. Table A.2 provides the normalized covariance matrices of the 11 features used in Stage 1. The normalized means can be derived from Table 3.8 using Eq. (3.20) and the normalization constants of Table 3.2.

Table A.1 Normalized variances for CC and HI. Some of these are used in Stage 2, with minimum value set to 0.005.

Class	CC	HI
1	1.257	0.0000
2	0.007	0.0000
3	0.137	0.0000
4	0.861	0.0000
5	0.465	0.0000
6	0.340	0.0000
7	1.239	0.0000
8	0.053	0.0000
9	0.638	0.0000
10	0.000	0.0000
11	0.219	0.0000
12	0.005	0.0000
13	1.325	0.0001
14	1.113	0.0002
15	0.567	0.0002
16	0.793	0.0812
17	0.262	0.8612
18	0.004	0.8244
19	0.000	0.0467
20	0.000	0.0253

COVARIANCE MATRIX OF THE FEATURES FOR CLASS 1

	ST	SE	AL	HT	BC	LO	MI	ML	CF	NC	LR
ST	1.5755										
SE	0.3344	1.0027									
AL	0.0572	0.2677	0.2029								
HT	0.0236	0.2088	0.1238	0.1059							
BC	0.0000	0.0000	0.0000	0.0000	0.0050						
LO	0.0026	0.0041	0.0036	0.0011	0.0000	0.0050					
MI	-0.0015	0.0026	0.0012	0.0014	0.0000	0.0000	0.0050				
ML	0.0000	0.0000	0.0000	0.0000	0.0000	0.0000	0.0000	0.0050			
CF	-0.0002	0.0055	0.0036	0.0022	0.0000	0.0001	0.0000	0.0000	0.0050		
NC	0.0003	0.0442	0.0368	0.0230	0.0000	0.0009	0.0003	0.0000	0.0009	0.0122	
LR	0.0000	0.0000	0.0000	0.0000	0.0000	0.0000	0.0000	0.0000	0.0000	0.0000	0.0050

COVARIANCE MATRIX OF THE FEATURES FOR CLASS 2

	ST	SE	AL	HT	BC	LO	MI	ML	CF	NC	LR
ST	0.8051										
SE	0.0292	0.4007									
AL	0.1039	0.1022	0.3312								
HT	0.0139	-0.0145	0.0224	0.0346							
BC	-0.0640	-0.1118	0.0247	-0.0101	0.7598						
LO	0.1084	0.1110	0.2069	-0.0400	-0.1440	0.7945					
MI	-0.0037	-0.0007	0.0092	0.0075	-0.0001	-0.0008	0.0050				
ML	0.0000	0.0000	0.0000	0.0000	0.0000	0.0000	0.0000	0.0050			
CF	0.0718	0.0767	0.1546	-0.0202	-0.1012	0.5559	0.0043	0.0000	0.3941		
NC	0.0032	-0.0140	-0.0373	0.0079	-0.0060	-0.0808	0.0011	0.0000	-0.0554	0.0180	
LR	0.0000	0.0000	0.0000	0.0000	0.0000	0.0000	0.0000	0.0000	0.0000	0.0000	0.0050

Table A.2 Normalized covariance matrices of the features for each class. The matrices are symmetric.

COVARIANCE MATRIX OF THE FEATURES FOR CLASS 3

	ST	SE	AL	HT	BC	LO	MI	ML	CF	NC	LR
ST	0.8651										
SE	-0.0268	0.8781									
AL	-0.0520	-0.0273	0.1094								
HT	-0.0483	-0.0266	0.0337	0.0489							
BC	0.0349	-0.0029	-0.0192	-0.0132	0.0285						
LO	-0.0745	-0.0561	0.0665	0.0304	-0.0587	0.2240					
MI	-0.0200	-0.0052	0.0161	0.0208	-0.0067	0.0096	0.0139				
ML	0.0000	0.0000	0.0000	0.0000	0.0000	0.0000	0.0000	0.0050			
CF	-0.0733	-0.0445	0.0634	0.0432	-0.0483	0.1673	0.0214	0.0000	0.1398		
NC	-0.3112	-0.1401	0.1536	0.0766	-0.1172	0.4191	0.0267	0.0000	0.3218	1.6630	
LR	0.0000	0.0000	0.0000	0.0000	0.0000	0.0000	0.0000	0.0000	0.0000	0.0000	0.0050

COVARIANCE MATRIX OF THE FEATURES FOR CLASS 4

	ST	SE	AL	HT	BC	LO	MI	ML	CF	NC	LR
ST	0.3136										
SE	-0.0101	0.5490									
AL	-0.0678	-0.0168	0.1164								
HT	-0.0327	-0.0122	0.0224	0.0239							
BC	-0.0170	0.0854	-0.1181	-0.0407	0.7016						
LO	0.1193	-0.0707	-0.0900	-0.0852	0.1041	0.4395					
MI	-0.1919	0.0797	0.1312	0.0950	-0.2451	-0.4262	0.5358				
ML	0.0000	0.0000	0.0000	0.0000	0.0000	0.0000	0.0000	0.0050			
CF	-0.1182	0.0338	0.0753	0.0404	-0.1849	-0.1411	0.2656	0.0000	0.1808		
NC	0.2258	-0.0083	-0.1666	-0.1340	0.8108	0.3591	-0.6910	0.0000	-0.4758	1.6813	
LR	-0.0693	0.0667	-0.0081	0.0280	0.0902	-0.0859	0.1478	0.0000	0.0953	-0.1957	0.2077

Table A.2 Continued

COVARIANCE MATRIX OF THE FEATURES FOR CLASS 5

	ST	SE	AL	HT	BC	LO	MI	ML	CF	NC	LR
ST	0.7611										
SE	0.1541	0.6434									
AL	-0.0197	-0.0332	0.1311								
HT	-0.0242	-0.0248	0.0277	0.0364							
BC	-0.0014	0.0069	-0.0549	-0.0224	0.1492						
LO	-0.0706	-0.0295	0.0448	-0.0045	-0.0911	0.2521					
MI	-0.0719	-0.0311	0.0419	0.0387	-0.0393	0.0077	0.0711				
ML	0.0000	0.0000	0.0000	0.0000	0.0000	0.0000	0.0000	0.0050			
CF	-0.1257	-0.0537	0.0754	0.0376	-0.1052	0.1846	0.0803	0.0000	0.2137		
NC	-0.0122	0.0266	0.0645	0.0344	-0.0848	0.1225	0.0674	0.0000	0.1564	0.3576	
LR	0.0000	0.0000	0.0000	0.0000	0.0000	0.0000	0.0000	0.0000	0.0000	0.0000	0.0050

COVARIANCE MATRIX OF THE FEATURES FOR CLASS 6

	ST	SE	AL	HT	BC	LO	MI	ML	CF	NC	LR
ST	0.3585										
SE	-0.0653	0.5479									
AL	0.0079	-0.0052	0.0914								
HT	-0.0061	0.0052	0.0061	0.0289							
BC	0.0094	-0.0832	-0.0245	-0.0272	0.5351						
LO	0.0251	-0.0759	0.0091	-0.1397	0.1223	0.9849					
MI	0.0066	0.0624	0.0196	0.0997	-0.2043	-0.6727	0.5642				
ML	0.0000	0.0000	0.0000	0.0000	0.0000	0.0000	0.0000	0.0050			
CF	0.0248	0.0127	0.0270	0.0071	-0.1293	-0.0186	0.1229	0.0000	0.1164		
NC	-0.0029	0.0209	0.0154	0.0084	0.1039	-0.0180	-0.0692	0.0000	-0.0852	0.2097	
LR	0.0000	0.0000	0.0000	0.0000	0.0000	0.0000	0.0000	0.0000	0.0000	0.0000	0.0050

Table A.2 Continued

COVARIANCE MATRIX OF THE FEATURES FOR CLASS 7

	ST	SE	AL	HT	BC	LO	MI	ML	CF	NC	LR
ST	0.9574										
SE	-0.1173	0.8995									
AL	-0.0902	-0.0390	0.1600								
HT	-0.0464	-0.0089	0.0367	0.0412							
BC	0.1623	0.1169	-0.1213	-0.0574	0.7961						
LO	-0.1618	-0.0089	0.0914	-0.0395	-0.3616	0.6504					
MI	-0.0585	-0.0823	0.0903	0.0945	-0.1621	-0.1922	0.3567				
ML	0.0023	0.0040	-0.0015	-0.0033	0.0084	0.0068	-0.0112	0.0050			
CF	-0.1744	-0.0927	0.1591	0.0718	-0.4238	0.2528	0.2409	-0.0070	0.4305		
NC	0.6684	-0.0400	-0.3945	-0.1792	0.8824	-0.4968	-0.4941	0.0107	-0.8675	2.6430	
LR	0.0020	-0.0720	-0.0329	0.0514	-0.0973	-0.1419	0.2459	-0.0071	0.1595	-0.3130	0.3783

COVARIANCE MATRIX OF THE FEATURES FOR CLASS 8

	ST	SE	AL	HT	BC	LO	MI	ML	CF	NC	LR
ST	0.2072										
SE	-0.0410	1.4821									
AL	-0.0272	-0.0944	0.3608								
HT	0.0063	0.0493	0.0942	0.0746							
BC	-0.0004	-0.1892	0.0396	-0.0743	0.5688						
LO	0.0097	-0.0967	-0.1581	-0.0804	0.0916	0.2071					
MI	-0.0352	0.0643	0.2327	0.0882	-0.1284	-0.2374	0.3327				
ML	-0.0046	-0.0369	0.0004	-0.0175	0.0185	-0.0011	0.0097	0.0319			
CF	-0.0302	-0.0002	0.1343	0.0365	-0.0709	-0.1047	0.1838	0.0095	0.1202		
NC	0.0407	-0.1046	-0.2019	-0.0679	0.1191	0.1726	-0.2488	0.0009	-0.1410	0.3209	
LR	0.0000	0.0000	0.0000	0.0000	0.0000	0.0000	0.0000	0.0000	0.0000	0.0000	0.0050

Table A.2 Continued

COVARIANCE MATRIX OF THE FEATURES FOR CLASS 9

	ST	SE	AL	HT	BC	LO	MI	ML	CF	NC	LR
ST	0.5584										
SE	0.0197	0.9163									
AL	0.0179	-0.1104	0.1538								
HT	0.0167	-0.0887	0.0706	0.0524							
BC	-0.0329	-0.1106	-0.1319	-0.0507	0.6112						
LO	-0.0132	0.1840	-0.1149	-0.0823	-0.0255	0.2408					
MI	0.0151	-0.1273	0.1577	0.0876	-0.1824	-0.1648	0.2551				
ML	-0.0339	0.1626	-0.1023	-0.1044	0.0537	0.0957	-0.0953	0.3373			
CF	0.0064	-0.0049	0.0856	0.0346	-0.2102	-0.0046	0.1531	-0.0335	0.1580		
NC	-0.0089	0.0164	-0.0658	-0.0531	0.2033	0.1188	-0.2420	-0.0034	-0.1716	0.6278	
LR	0.0000	0.0000	0.0000	0.0000	0.0000	0.0000	0.0000	0.0000	0.0000	0.0000	0.0050

COVARIANCE MATRIX OF THE FEATURES FOR CLASS 10

	ST	SE	AL	HT	BC	LO	MI	ML	CF	NC	LR
ST	0.5933										
SE	0.1180	1.0768									
AL	-0.0025	0.0704	0.4030								
HT	0.0011	0.0022	0.0558	0.0528							
BC	-0.0154	-0.0202	0.0033	0.0048	0.0108						
LO	0.0114	0.0278	-0.0821	-0.0067	0.0000	0.0467					
MI	0.0049	-0.0490	0.1031	0.0070	0.0059	-0.0554	0.1531				
ML	0.0252	-0.0537	0.0257	-0.0603	-0.0085	-0.0490	0.0885	0.2191			
CF	0.0133	-0.0319	0.0508	0.0026	0.0062	-0.0257	0.1225	0.0591	0.1111		
NC	-0.0118	0.0177	-0.0275	0.0043	-0.0012	0.0206	-0.0456	-0.0376	-0.0336	0.0279	
LR	0.0603	-0.0617	-0.3771	-0.0612	-0.0043	0.0923	-0.0272	0.0259	0.0364	0.0042	0.5719

Table A.2 Continued

COVARIANCE MATRIX OF THE FEATURES FOR CLASS 11

	ST	SE	AL	HT	BC	LO	MI	ML	CF	NC	LR
ST	0.6338										
SE	-0.1174	0.5764									
AL	-0.0344	-0.0189	0.1842								
HT	-0.0226	0.0046	0.0087	0.0312							
BC	0.0538	-0.2249	0.0624	-0.0232	0.7090						
LO	0.0520	-0.0100	-0.0036	-0.0681	0.1183	0.4595					
MI	-0.0809	0.0531	0.0750	0.0576	-0.1958	-0.3324	0.4017				
ML	-0.0010	0.0002	-0.0106	-0.0152	0.0092	0.0018	-0.0035	0.0227			
CF	-0.0486	0.0490	0.0765	0.0129	-0.1229	-0.0284	0.1900	-0.0024	0.1800		
NC	0.0497	-0.0482	-0.0323	-0.0080	0.0674	0.0479	-0.1141	-0.0045	-0.0867	0.1020	
LR	0.0000	0.0000	0.0000	0.0000	0.0000	0.0000	0.0000	0.0000	0.0000	0.0000	0.0050

COVARIANCE MATRIX OF THE FEATURES FOR CLASS 12

	ST	SE	AL	HT	BC	LO	MI	ML	CF	NC	LR
ST	1.7596										
SE	0.0195	0.5401									
AL	-0.1325	-0.2185	0.4888								
HT	-0.0531	0.0193	0.0344	0.1242							
BC	-0.0331	-0.1104	0.3230	0.0087	0.9922						
LO	0.1397	0.0010	-0.1576	-0.1454	0.2172	2.0344					
MI	-0.1046	-0.0171	0.1331	0.0976	-0.1089	-1.3375	0.8893				
ML	0.0175	-0.0907	0.0840	-0.1285	-0.0985	-0.7617	0.4982	1.0066			
CF	-0.0114	-0.0171	0.0301	0.0019	0.0373	0.0155	0.0003	-0.0095	0.0112		
NC	0.0057	0.0075	-0.0205	0.0002	-0.0226	-0.0147	0.0049	0.0106	-0.0051	0.0050	
LR	0.0000	0.0000	0.0000	0.0000	0.0000	0.0000	0.0000	0.0000	0.0000	0.0000	0.0050

Table A.2 Continued

COVARIANCE MATRIX OF THE FEATURES FOR CLASS 13

	ST	SE	AL	HT	BC	LO	MI	ML	CF	NC	LR
ST	0.8519										
SE	-0.0494	0.6922									
AL	0.0133	-0.0095	0.1860								
HT	0.0349	-0.0681	0.0055	0.0816							
BC	-0.0870	-0.0981	-0.1495	0.0084	0.7926						
LO	0.0115	0.0018	0.0251	-0.0221	-0.1038	0.0625					
MI	0.0188	-0.0183	0.2203	-0.0015	-0.6819	0.0925	0.8146				
ML	-0.0207	0.0050	-0.0468	-0.0163	0.0661	-0.0109	-0.0648	0.0533			
CF	0.0327	-0.0224	0.2483	-0.0125	-0.7905	0.1403	0.9214	-0.0761	1.0673		
NC	-0.1249	0.0348	-0.0974	0.0018	0.3119	-0.0616	-0.2801	0.0363	-0.3411	0.6923	
LR	-0.0687	-0.1001	0.0576	-0.0675	-0.4423	0.1559	0.5301	-0.0153	0.6641	-0.1880	0.9414

COVARIANCE MATRIX OF THE FEATURES FOR CLASS 14

	ST	SE	AL	HT	BC	LO	MI	ML	CF	NC	LR
ST	0.6771										
SE	0.1729	0.8079									
AL	-0.1885	-0.1507	0.3354								
HT	0.0748	-0.0231	-0.0035	0.0701							
BC	0.0306	-0.0104	-0.1753	-0.0223	0.7365						
LO	-0.1725	-0.0293	0.0731	-0.0966	-0.1908	0.5695					
MI	-0.0494	-0.1004	0.1553	0.0417	-0.2442	-0.1282	0.2903				
ML	-0.2844	-0.0334	0.0993	-0.1415	0.0404	-0.0098	0.1027	0.6847			
CF	-0.1729	-0.1267	0.2151	-0.0216	-0.3917	0.2626	0.2166	0.0965	0.4121		
NC	0.1800	0.4512	-0.4024	-0.0137	0.5041	-0.3538	-0.2189	0.0375	-0.4787	1.5377	
LR	0.0000	0.0000	0.0000	0.0000	0.0000	0.0000	0.0000	0.0000	0.0000	0.0000	0.0050

Table A.2 Continued

COVARIANCE MATRIX OF THE FEATURES FOR CLASS 15

	ST	SE	AL	HT	BC	LO	MI	ML	CF	NC	LR
ST	0.9545										
SE	0.0364	0.5913									
AL	-0.0399	-0.1036	0.4329								
HT	0.0284	-0.0028	0.0120	0.0329							
BC	0.3107	0.0330	0.0032	0.0228	0.8345						
LO	-0.0595	0.0053	-0.0152	-0.0120	-0.0733	0.0456					
MI	-0.0956	-0.0586	0.1441	0.0154	-0.4201	0.0138	0.5619				
ML	-0.0239	0.0217	-0.0992	-0.0584	0.0747	-0.0256	-0.0951	0.4608			
CF	-0.1429	-0.0583	0.1411	0.0093	-0.4903	0.0461	0.5981	-0.1219	0.6585		
NC	0.0004	0.0653	-0.0964	0.0020	0.1849	-0.0273	-0.2152	0.0474	-0.2451	0.1873	
LR	-0.0059	-0.0110	-0.2919	-0.0237	-0.2786	0.1069	0.1890	0.0150	0.2719	-0.0856	0.9282

COVARIANCE MATRIX OF THE FEATURES FOR CLASS 16

	ST	SE	AL	HT	BC	LO	MI	ML	CF	NC	LR
ST	0.8066										
SE	-0.0939	0.6329									
AL	-0.0146	-0.0106	0.0877								
HT	-0.1418	0.0105	0.0308	0.2858							
BC	0.1236	0.0063	-0.0179	-0.1000	0.9238						
LO	0.0225	-0.0021	0.0027	-0.0635	-0.0869	0.1037					
MI	-0.1803	0.0443	0.0300	0.2017	-0.4591	-0.0216	0.5248				
ML	0.2884	-0.1251	-0.0521	-0.4182	0.2940	0.0138	-0.4162	1.0322			
CF	-0.1964	0.0336	0.0401	0.2625	-0.5585	0.0235	0.5822	-0.5093	0.7213		
NC	0.1002	-0.0049	-0.0532	-0.2161	0.3322	0.0380	-0.3676	0.2883	-0.4364	0.6237	
LR	0.0910	0.0441	-0.2926	-0.2088	0.0598	0.0010	-0.1509	0.3405	-0.1954	0.1348	1.5004

Table A.2 Continued

COVARIANCE MATRIX OF THE FEATURES FOR CLASS 17

	ST	SE	AL	HT	BC	LO	MI	ML	CF	NC	LR
ST	0.7204										
SE	0.0112	0.5244									
AL	-0.0309	-0.0079	0.1461								
HT	0.0098	-0.0543	-0.0136	0.2660							
BC	-0.0356	-0.0678	0.0377	-0.0207	0.6223						
LO	-0.0085	0.0211	0.0090	-0.0516	0.0125	0.0925					
MI	-0.0175	0.0634	0.0144	-0.2131	-0.1284	0.0088	0.4973				
ML	-0.0188	-0.0845	0.0123	0.2020	-0.0001	-0.1545	-0.3439	0.7896			
CF	-0.0077	-0.0289	0.0172	0.0670	-0.1326	-0.0420	0.0961	0.1126	0.2037		
NC	0.0068	0.0377	-0.0262	-0.0663	0.1097	0.0314	-0.0813	-0.0939	-0.1882	0.2494	
LR	0.1042	-0.0445	-0.2477	0.0124	-0.1558	0.0141	0.2434	-0.2941	0.1403	-0.1114	1.0913

COVARIANCE MATRIX OF THE FEATURES FOR CLASS 18

	ST	SE	AL	HT	BC	LO	MI	ML	CF	NC	LR
ST	0.8531										
SE	-0.0899	0.6819									
AL	-0.0848	0.0442	0.3589								
HT	0.0485	-0.0538	0.0731	0.3295							
BC	-0.0068	-0.1446	0.1948	0.0230	0.8027						
LO	0.0034	0.0131	-0.0350	-0.0336	-0.0304	0.1941					
MI	-0.1005	0.1099	-0.0159	-0.2731	-0.0795	-0.0518	0.5584				
ML	0.0496	-0.0806	0.1341	0.1301	0.1929	-0.1524	-0.3109	0.7133			
CF	-0.0300	0.0255	0.0585	0.0088	0.0578	-0.0359	0.0568	0.0575	0.0725		
NC	0.0116	-0.0017	-0.0380	-0.0101	-0.0354	0.0189	-0.0202	-0.0362	-0.0373	0.0398	
LR	0.0000	0.0000	0.0000	0.0000	0.0000	0.0000	0.0000	0.0000	0.0000	0.0000	0.0050

Table A.2 Continued

COVARIANCE MATRIX OF THE FEATURES FOR CLASS 19

	ST	SE	AL	HT	BC	LO	MI	ML	CF	NC	LR
ST	0.8474										
SE	0.0938	0.4439									
AL	0.0048	0.0343	0.1942								
HT	-0.0144	0.0345	-0.0034	0.0935							
BC	0.0055	0.0066	0.0926	-0.0160	0.7774						
LO	0.0000	0.0000	0.0000	0.0000	0.0000	0.0050					
MI	-0.0244	-0.0053	-0.0003	-0.0143	-0.0445	0.0000	0.0127				
ML	0.0233	0.0045	-0.0032	0.0166	0.0493	0.0000	-0.0142	0.0168			
CF	-0.0084	-0.0021	0.0383	-0.0019	0.0260	0.0000	0.0002	-0.0006	0.0224		
NC	0.0022	-0.0006	-0.0257	0.0039	-0.0122	0.0000	-0.0009	0.0012	-0.0144	0.0108	
LR	0.0000	0.0000	0.0000	0.0000	0.0000	0.0000	0.0000	0.0000	0.0000	0.0000	0.0050

COVARIANCE MATRIX OF THE FEATURES FOR CLASS 20

	ST	SE	AL	HT	BC	LO	MI	ML	CF	NC	LR
ST	1.2422										
SE	0.1266	0.4355									
AL	0.0205	-0.1059	0.2657								
HT	-0.1025	-0.0810	0.1049	0.1502							
BC	-0.0063	-0.0343	0.0664	-0.0052	0.1678						
LO	0.0000	0.0000	0.0000	0.0000	0.0000	0.0050					
MI	0.0193	0.0229	-0.0195	-0.0221	-0.0034	0.0000	0.0166				
ML	-0.0158	-0.0242	0.0194	0.0173	0.0058	0.0000	-0.0169	0.0188			
CF	0.0009	0.0012	0.0004	-0.0012	0.0036	0.0000	-0.0002	0.0004	0.0050		
NC	-0.0021	-0.0014	-0.0001	0.0018	-0.0035	0.0000	0.0003	-0.0005	-0.0007	0.0050	
LR	0.0000	0.0000	0.0000	0.0000	0.0000	0.0000	0.0000	0.0000	0.0000	0.0000	0.0050

Table A,2 Continued

REFERENCES

Agee, E. M. and K. E. Dowell, 1974: Observational studies of mesoscale cellular convection, J. Appl. Meteor., 13, 46-53.

Bakan, S., 1985: On the structure of open cellular convection as revealed by time series of surface observations: a case study, Beitr. Phys. Atmosph., 58, 11-16.

Bates, J. J. and W. L. Smith, 1985: Sea surface temperatures: observations from geostationary satellites. J. Geophys. Res., 90, C6, 11609-11618.

Beniston, M., 1985: Organization of convection in a numerical mesoscale model as a function of initial and lower boundary conditions, Beitr. Phys. Atmosph.,58, 31-52.

Brard, A., 1980: Sur une analyse automatique simple des images d'un satellite meteorologique geostationnaire, Ministere des Transports,Direction de la Meteorologie, France, tech. note 77, Nouvelle serie, 48pp.

Bunting, J. T. and R. F. Fournier, 1980: Tests of spectral cloud classification using DMSP fine mode satellite data, Environmental Reasearch Papers, no. 704, Air Force Geophys. Lab., AFGL-TR-80-0181, 42pp.

Desbois, M., G. Seze and G. Szejwach, 1982: Automatic classification of clouds on METEOSAT imagery: Application to high-level clouds. J. Appl. Meteor., 21, 401-412.

Duda, R. O. and P. E. Hart, 1973: Pattern Classification and Scene Analysis, John Wiley & Sons, 482pp.

Forsythe, G. E.,M. A. Malcolm and C. B. Moler, 1977: Computer methods for mathematical computations, Prentice-Hall, 259pp.

Garand, L., and J. A. Weinman, 1986: A structural-stochastic model for the analysis and synthesis of cloud images, J. Climate Appl. Meteor., 25, 1052-1068.

Garand, L., J. A. Weinman and C. M. Moeller, 1987, Automated recognition of oceanic cloud patterns. Part 2: application to remote sensing of meteorological parameters, J. Climate Appl. Meteor, 26, pp.

Hahn, C. J., S. G. Warren, J. London, R. M. Chervin and R. Jenne, 1982: Atlas of Simultaneous Occurrence of Different Cloud Types over the Ocean, NCAR Tech. Note TN-201+STR, 212pp. (NTIS PB83-152074.)

Haralick, R. M., K. Shanmugam and I. Dinstein, 1973: Textural features for image classification, IEEE Trans. Systems, Man, Cybernetics, 3, 610-621.

Hibbard, W. L. and D. P. Wylie, 1985: An efficient method of interpolating observations to uniformly spaced grids, Preprint volume of Int. Conf. on Interactive Processing Systems for Meteorology, Oceanography, and Hydrology, Los Angeles, CA, Jan 7-11, Amer. Meteor. Soc., 144-147.

Hoeber, H. C., 1982: KONTUR Convection and Turbulence Experiment Field Phase Report, Hamburger Geophysikalische Einzelschrif-

ORIGINAL PAGE IS
OF POOR QUALITY

ten, Reihe B, Heft 1.

Logan, T. L., J. R. Huning, J. R. and D. L. Glackin, 1983, Cloud cover typing from environmental satellite imagery; discriminating cloud structure with fast Fourier transforms, Jet Propulsion Lab. publication 84-17, Pasadena Calif., 55pp.

Martin, R. S., G. Peter and J. H. Wilkinson, 1965: Symmetric decomposition of a positive definite matrix, Numerische Mathematik, 7, 362-383.

Minnis, P., and E. F. Harrison, 1984a: Diurnal variability of regional cloud and clear-sky radiative parameters derived from GOES data. Part I: Analysis method. J. Climate Appl. Meteor., 23, 993-1011.

____, and ____, 1984b: Diurnal varability of regional cloud and clear-sky radiative parameters derived from GOES data. Part I: November 1978 cloud distributions, ibid, 1012-1031.

____, and _____, 1984c: Diurnal variability of regional cloud and clear-sky radiative parameters derived from GOES data. Part III: November 1978 radiative parameters, ibid, 1032-1051.

Mui, J. K.,and K-S. Fu, 1980: Automated classification of nucleated blood cells using a binary tree classifier, IEEE Trans. on Pattern Analysis and Mach. Intell., 2, 429-443.

Parikh, J., 1977: A comparative study of cloud classification techniques, Remote Sensing of Environment, 6, 67-81.

Platt, C. M. R., 1983: On the bispectral method for cloud parameter determination from satellite VISSR data: Separating broken cloud and semitransparent cloud, J. Appl. Meteor., 22, 429-439.

Rochard, G., 1978: Sur quelques parametres simples de la texture nuageuse observee par satellite, Ministere des Transports, Direction de la Meteorologie, France, techn. note 408, 25pp.

Rosenfeld, A. and A. C. Kak, 1982: Digital picture processing, 2nd edition, Vol.1, Academic Press, 435pp.

Rossow, W. B., F. Mosher, E. Kinsella, A. Arking, M. Desbois, E. Harrison, P. Minnis, E. Ruprecht, G. Seze, C. Simmer and E. Smith, 1985: ISCCP cloud algorithm in tercomparison, J. Climate Appl. Meteor., 24, 877-903.

Schmetz, J., 1984: On the parameterization of the radiative properties of broken clouds, 1984, Tellus, 36A, 417-432.

Scheur, E. M. and D. S. Stoller, 1962: On the generation of normal random numbers, Technometrics, 4, 278-281.

Scorer, R. S., 1972: Clouds of the World, A Complete Color Encyclopedia, Lothian Publishing Co Ltd, Melbourne, Australia or David & Charles, Newton Abbot, UK, 176pp.

Scorer, R. S., 1986: Cloud investigation by satellite, published by Ellis Horwood Limited, distributed by Halsted Press, a division of John Wiley and Sons, no paging.

Shenk, W. E., R. J. Holub and R. A. Neff, 1976: A multispectral cloud type identification method developed for tropical ocean

CLASSIFICATION OF SATELLITE IMAGES OF EXTRA-TROPICAL CYCLONES OVER THE OCEAN BY MEANS OF COMPUTERIZED PATTERN ANALYSIS

ORIGINAL PAGE IS
OF POOR QUALITY

Craig R. Burfeind and James A. Weinman

Department of Meteorology
University of Wisconsin-Madison 53706

I. Introduction

Currently, there are many regions over the oceans, where no surface or upper-air data are measured by conventional methods. Although upper-air temperature and humidity soundings can be obtained from infrared and microwave measurements from satellite-borne radiometers, the surface pressure is not at present being measured operationally using these methods. Accurate surface-pressure measurements are needed to obtain good weather forecasts.

Attempts have been made to manually assign quantitative parameters to large-scale vortices observed in satellite weather images. Troup and Streten (1972) devised a cyclone classification scheme according to developmental stage by means of an objective set of rules applied to a satellite picture to classify the cyclone. The surface-pressure field was statistically derived using the cyclone class and the climatology for that class. Guymer (1978) used both the large-scale shape and small-scale features to derive several meteorological parameters. This analysis was conducted by a human analyst. Such analysts may become less attentive after looking at many such satellite pictures.

No previous attempts have been made to automatically classify cyclone images or to derive meteorological parameters from satellite images by means of computer analysis. This study is a first attempt to automatically classify cyclones over the ocean. Once an objective technique for obtaining parameters from the shape, size, and orientation is devised, a regression scheme using climatology can be applied to the data without concern for errors induced by subjective biases. This paper presents an automatic satellite-image classification technique that places cyclones into five classes which are comparable to the five classes defined by Troup and Streten (1972) (see Figure 1).

The algorithm presented here classifies oceanic extratropical cyclones into one of these five classes, locates the cyclone center and the appropriate fronts, and derives a set of objective parameters that describe the size, shape and orientation of the storm system. All this is done without manual intervention.

The technique can be divided into four steps:

1) The image of the cyclone is extracted from the GOES hemispheric picture by means of the McIDAS image display system (Suomi et. el., 1983). This is done so that analyses can be done on only the extratropical cyclone in question. This procedure uses the position of the 24 hour LFM forecast cyclone-center as an approximate indicator to initiate the search for the cyclone.

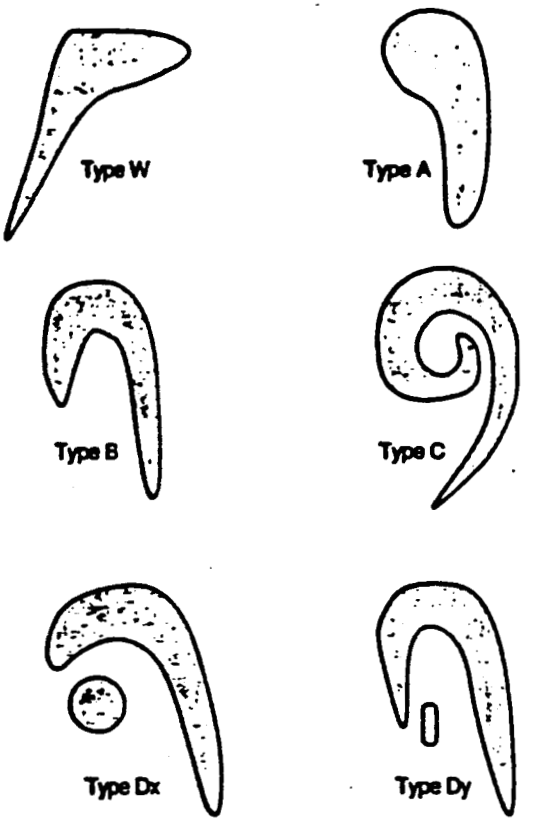


Figure 1: Schematic diagram of the six cloud pattern classifications defined by Troup and Streten (1972).

2) The cyclone is placed into one of five classes. In order to do this, objective parameters that describe the appearance of the system are calculated and used to determine the cyclone type.

3) The center of rotation is located using the cyclone class and the visible image.

4) The fronts are located using the class, the cyclone center, and the visible image as input information.

Fifteen cases are analyzed in this study. Their time of observation, location, and original spatial resolution are summarized in Table 1.

II. Preprocessing of GOES Visible and Infrared Images of Extratropical Cyclones

At any given there are numerous cyclone systems in various stages of

Data Set	Date	Time (GMT)	Latitude (deg)	Longitude (deg)	Resolution (km)
1	4-6-84	19:45	25-60N	125-170W	16X16
2	12-9-83	20:46	25-50N	130-160W	16X16
3	4-5-84	19:45	20-40N	120-235W	16X16
4	4-20-84	19:45	25-60N	130-170W	16X16
5	4-13-84	19:45	25-60N	125-150W	16X16
6	3-3-85	20:00	35-60N	120-150W	16X16
7	3-22-85	20:01	30-50N	125-165W	16X16
8	2-2-84	20:45	15-40N	145-170W	16X16
9	3-29-84	20:45	30-65N	130-170W	16X16
10	2-3-84	20:46	25-45N	155-180W	16X16
11	2-22-84	20:45	25-50N	130-175W	16X16
12	2-26-84	20:46	20-50N	125-150W	16X16
13	11-13-84	19:00	25-45N	130-150W	16X16
14	11-15-84	20:00	25-50N	120-140W	16X16
15	3-2-84	20:45	15-45N	140-170W	16X16

Table 1 : Data set number along with time and location of observation, and spatial resolution for each data set.

development over the oceans. In order to simplify the analysis, the extratropical cyclones are examined one at a time. This is done by extracting a single cyclone from the the GOES hemispheric picture. Because image analysis is computationally intensive, one desires to analyze an image which has the fewest number of pixels possible.

The position of the low-pressure center predicted by the 24 h LFM forecast is used as the first guess to locate the cyclone center. An area with dimensions of 5120 km in the latitudinal direction and 3840 km in the meridional direction with a pixel resolution of 16 km by 16 km is extracted from the full-disk visible and infrared pictures to produce images consisting of 320 pixels in the east-west direction, and 240 pixels in the north-south direction. These images, both visible and infrared, are extracted from GOES pictures so that the center of the cyclone is one-third of the distance from the northern edge to the southern edge and one-half of the distance between the eastern and western edges of the 320 X 240 image. These 320 X 240 pixel images are then remapped into a Mercator projection with the same number of pixels. This procedure is applied to both the visible and the infrared images to remove large shape distortions caused by the location of the storm relative to the GOES satellite location. This also allows all pictures to be analyzed in the same projection, which is important in the derivation of a single technique for classifying storms at different latitudes. Finally, the 320 X 240 pixel images are degraded by averaging over 8 X 6 pixel boxes to produce images consisting of 40 X 40 pixels each having a resolution of 128 km by 96 km.

The size of extratropical cyclones can vary over an order of magnitude; it is, therefore, desirable to scale all cyclone images so that an image can be created in which all possible cyclones cover approximately the same area in the 40 X 40 pixel image. To produce this image, smaller cyclones are enlarged by a greater factor than larger cyclones. The resolution will be different for each cyclone picture. This area normalization is important so that only one classification and location scheme needs to be developed, instead of having an analysis which depends upon the size of the cyclone.

The normalization process uses many digital image processing techniques, including brightness normalization, thresholding to produce a binary image, spatial filtering to reduce noise, and extraction from the original full resolution visible image to produce the normalized image. From the normalized image, the angle of orientation, along with various size parameters are determined for the cyclone's image. Brightness normalization is performed to correct for limb darkening produced at large solar zenith angles.

III. Classification of the Degree of Development of Extratropical Cyclones Using the Visible Image

The classification of the cyclone's degree of development is achieved by determining several features of the cyclone images, which are then used as indicators to classify the cyclone type. In order to identify the properties of the cyclone image, the scaled cyclone image must be further simplified.

A decision tree structure (see Figure 2) is used to classify the extratropical cyclones. At each node of the tree, one feature is used to determine whether the cyclone fits a certain class. If so, it is classified and the procedure is complete. Otherwise, the next feature is extracted and another decision takes place.

The first feature which is needed to classify cyclone systems is the orientation angle of the major axis of the elliptical approximation of the original visible image. The original image is fit to an ellipse so this analyses can be completed. The angle of orientation is taken to be zero if the major axis of the ellipse is oriented along an east-west line and 90 degrees if the cyclone's major axis is along a north-south line. This angle is used to determine if a cyclone is in the wave stage as opposed to a more developed cyclone. Cyclones with smaller angles

ORIGINAL PAGE IS
OF POOR QUALITY

ORIGINAL PAGE IS
OF POOR QUALITY

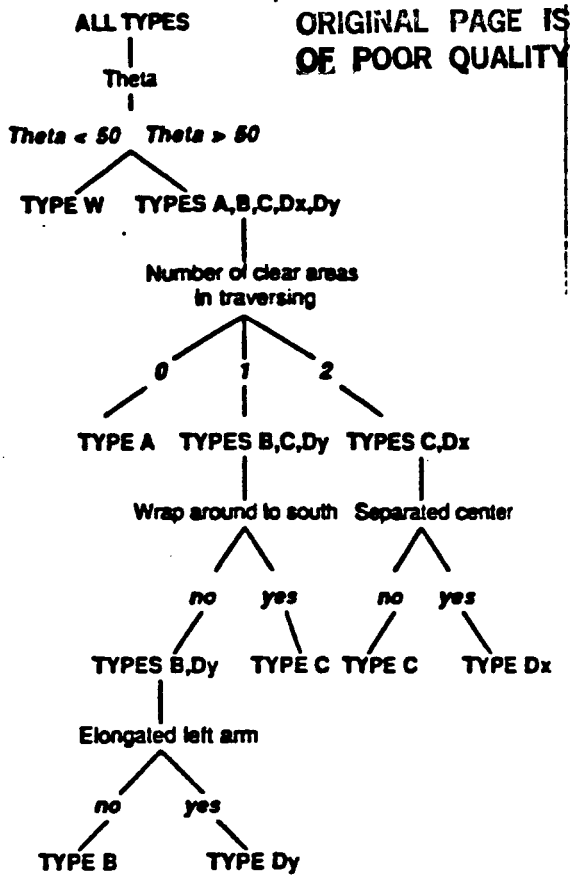


Figure 2 : Decisison tree structure for classifying cyclones.

are thus classified as wave-stage cyclones (denoted W). It is found empirically that a cutoff of 50 degrees best separates wave-stage cyclones from the other types of cyclones.

The remaining features are derived from an image which is a subset of the scaled visible image. A high-resolution image which consisists of the center core of the cyclone system is extracted from the original Mercator visible image. The center point and the size of this high-resolution center section is determined from the centroid of the degraded scaled image. Similer degradation is again applied to the scaled image to produce a noise-free, binary image of the center spirals of the system. This final image is used for cyclone classification.

The pattern-analysis algorithm searches for dry tongues by looking for the first continuous, horizontal string of pixels with a value of 200 on the east edge of the picture. From this continuous string, it searches towards the west until it finds a clear area. It then continues to search towards the west for a cloudy area and repeats the same procedure again, each time counting the number of pixels in the clear area. When a clear area is located, the program searches towards the south to determine whether the cyclone has begun to wrap up. A cyclone is considered to have wrapped up if there are at least two pixels extending toward the east from the southwestern arm of the system. This procedure yields two features--the number of clear slots and an indication as to whether the cyclone has wrapped up.

The binary image is used to classify the cyclones which did not fall into the W class, by looking for the dry tongue. If no dry tongue is present, then the cyclone is classified as a type A. If a dry tongue is present, the algorithm searches to the south to determine whether the cyclone has begun to wrap up or checks for two slots of dry air between the edges of the entire cyclone, thus indicating that the cyclone has wrapped around itself a second time. If either of these features are present, the cyclone is classified as a type C; otherwise, it is classified as a type B.

At this point all cyclones which can be classified as W, A, B, or C have been classified. Also, the algorithm has saved certain reference points on the image for later use in determining the cyclone center. In order to classify the types D_x and Dy, the program checks types B and C to see if they are not actually of type D, since all type D's would have been included in the classification of type B or C up to this point.

First a check is made to determine whether the wrapped-around cloud band of a type B or C is connected to the main cloud band. The segmented image is used to determine if the cloud band is continuous by comparing the label on the center spiral region with the label on the frontal band. If the labels are the same, the cloud band is continuous and the cyclone classification is left unchanged. If the regions have different labels, the cyclone system is classified as a type D_x. If the center spiral is disconnected from the main cloud band, it is classified as a dissipating cyclone.

Secondly, type B cyclones are checked to determine if the cloud band to the west, which has not wrapped around is elongated. This is done by comparing the lengths of the western arm and the eastern arm associated with the cold front.

IV. Location of the Cyclone Center

A different technique for locating the cyclone center is used for each of the five classes. Using points saved previously as starting locations, the program moves predetermined distances from these locations to determine the cyclone center.

This section of the program takes as input the three locations on the spirals: the location of the southwestern edge of the dry tongue, the center of the northern edge of the cloud band which is wrapped around to the south, and the western edge of the cloud band which has wrapped around a second time to the east of the second dry tongue.

For type W cyclones, the cyclone

center is located where the thickest bulge is found in the band of cloudiness, or where the curvature of the cloud bands changes sign. In either case, this is where the cloud band is thickest in the east-west direction. The same procedure that is used for type W cyclones is also used for type A cyclones. The only difference is that the classification of type A cyclone uses the entire image and not only the high-resolution center section. For type B cyclones, the point located at the southwestern edge of the dry tongue is used as a starting point for locating the cyclone center. This point is also used for type Dy. It was empirically determined that the center of the cyclone should be placed at the point one pixel to the south of the point saved in the above procedure. If the cyclone is determined to be a type Dy, then the cloud band is searched to find the southern-most tip of the western cloud leg of the type Dy. It is this point that is given as the cyclone center in type Dy cyclones. For type C cyclones, two possibilities exist. The first is that the cyclone has only begun to wrap around to the south, but has not started to form the second dry tongue. The second is that it has begun to wrap up, thus forming a second slot of dry air as the cyclone is traversed form east to west. For the first case, the algorithm begins searching from the point on the northern edge of the band which has wrapped to the south towards the northeast until it has located the northeastern-most edge of the cloud band. The cyclone center is placed two pixels to the west of this point, which corresponds to the vertex of the spiralling band. In the second case, the cyclone center is placed one pixel to the north of the point which is defined as the western edge of the cloud band which has begun to wrap around a second time to the east. This once again places the center at the vertex of the spiralling cloud band. If the cyclone is classified as a type D_X, then the cloudy area closest to the center of rotation is located. This cloudy area is disconnected from the main cloud structure as indicated above. The centroid of this region is determined and is taken to be the cyclone center.

V. Location of the Front

The final analysis done by this algorithm is to roughly locate the cold front, or the occluded front. In the case of the type W system, the warm front is also located. It should be pointed out that for dissipating cyclones (type D's) no front is located.

The original Mercator visible image is the starting point in the frontal analysis. A binary image is created from this image. A filter is placed over this binary image to remove the noise and rough edges while retaining the general shape of the frontal cloud bands. The front is determined by moving away from the center of rotation in predetermined directions until the frontal cloud bands are located. These points are marked and saved. After all points which make up the front are located, the front is smoothed by placing a running mean through the points.

VI. Results

The relative area of the cyclone cloud (Table 2) shows no strong correlation to the type of cyclone. This indicates that any cyclone type can vary in size. The value of theta changes as the cyclone matures. Small angles are noted in developing cyclones since the cold air is still to the north and has not begun to sweep southward to overtake the warm air. As the cyclones develop, larger angles are found as the tilt of the system becomes more negative due to the southward sweeping cold air. description of the cyclone system.

Data	Type	Area Str ($x10^3$ km)	Connect	Theta (deg)
1	C	92.77	1.00	87.1
2	C	54.95	1.00	139.5
3	B	34.76	1.00	97.3
4	DX	92.77	0.94	100.5
5	B	105.71	0.99	74.4
6	C	93.58	1.00	106.9
7	W	78.68	1.00	33.6
8	B	82.43	1.00	101.3
9	A	108.52	1.00	75.6
10	A	42.57	1.00	93.1
11	W	96.76	1.00	33.0
12	DY	104.27	1.00	101.7
13	DX	38.86	0.71	74.2
14	DX	79.64	0.93	114.9
15	B	88.61	1.00	94.7

Table 2 : Cyclone classification and features for each data set.

A comparison of the results of this study with the results obtained from human analysts was performed. Six meteorologists, all of whom have had experience in analyzing satellite imagery or a strong synoptic meteorology background, analyzed the 15 cases to locate the low pressure center and the fronts. The mean low pressure center location and the mean frontal position along with the standard deviation for each of the 15 data sets were calculated for the six analyses.

Table 3 displays the distance between the cyclone center found by the computer algorithm and the mean center location found by the analysts. Along with these values, the standard deviation for the human analysts and the ratio of the computer's distance from the mean to the human analysts' standard deviation is tabulated. Except for one very bad case (data set 4), the results show that the computer analysis is within one standard deviation half of the time and always

ORIGINAL PAGE IS
OF POOR QUALITY

Data Set	Subjective Std. Dev. (km)	Objective Dist. from Mean (km)	Ratio Dat from Mn Std dev
1	177	37	0.21
2	91	155	1.70
3	151	183	1.21
4	104	407	3.91
5	276	141	0.51
6	98	161	1.64
7	178	258	1.45
8	254	217	0.85
9	444	614	1.38
10	N/A	N/A	N/A
11	187	136	0.73
12	701	1086	1.55
13	70	32	0.46
14	202	101	0.50
15	343	268	0.78

Table 3 : Comparison of standard deviation of low pressure center position for a group of human analysts versus distance from the mean for the computer algorithm.

within two standard deviations. These results also show that the cases in which the computer algorithm had difficulty in locating the center and the fronts, the human analysts also produced a wide range of results.

Table 4 gives the same parameters for the frontal position. The computer algorithm did poorly on data sets 9 and 15, while the distances for the remaining cases are approximately equal to one standard deviation or less.

Overall, the computer algorithm showed the poorest results for type A cyclones, especially data set 9. This is due to the lack of large-scale structure encountered in type A cyclones when compared to the other types. Since the computer needs structure to serve as a guide in locating features of the extratropical system, it was unable to perform as well for these cases. Also, if more type A cyclones would be analyzed and used as training sets for the computer algorithm, performance might be improved.

The computer seemed to yield the best analysis on type C cyclones. This is mainly due to the structure associated with the spiralling center of rotation. The algorithm is able to locate many reference points on the spiralling cloud bands to use in identifying the low pressure center. Type C cyclones, especially data set 1, also show well defined and narrow frontal cloud bands which make the associated frontal position easy to locate.

These pattern analyses were conducted on an IBM AT-99 personal computer equipped with an 80287 coprocessor chip and 512 kb of random access memory. The

Data Set	Subjective Std. Dev. (km)	Objective Dist. from Mean (km)	Ratio Dist from Mn Std dev
1	143	44	0.31
2	86	24	0.28
3	75	80	1.07
4	N/A	N/A	N/A
5	125	312	2.50
6	118	91	0.77
7	151	141	0.93
8	114	41	0.36
9	170	1273	7.49
10	N/A	N/A	N/A
11	185	49	0.26
12	N/A	N/A	N/A
13	N/A	N/A	N/A
14	N/A	N/A	N/A
15	77	136	1.77

Table 4 : Comparison of standard deviation of frontal position for a group of human analysts versus the average distance from the human frontal position mean for the computer algorithm.

ORIGINAL PAGE IS
OF POOR QUALITY

extended "Turbo-Pascal" software system was used for programming these algorithms. The entire analysis took approximately 3 minutes from beginning to end for each cyclone. While the personal computer is in no way overburdened by these procedures, the analysis could be performed much more rapidly on a minicomputer equipped with a parallel array processor.

VII. Summary

An algorithm was developed that objectively analysed synoptic-scale satellite images depicting various stages of development of extratropical cyclones. The images were analyzed to assign a category to the cyclone based on its stage of development. Once classified, the rotation center and the fronts associated with the cyclone were located.

This classification scheme along with the parameters derived from the satellite images may ultimately used to empirically derive surface-pressure fields. Thus, the surface-pressure field could be derived from the large-scale features of the extratropical cyclone images. This would be similar to the work done by either Nagle and Hayden (1971) or Troup and Streten (1972). This technique would be especially useful over data-sparse regions of the oceans, where little surface-pressure data are available.

This study demonstrates that pattern analysis techniques may permit the development of rapidly executed, objective computer-assisted analyses of satellite images. These analyses are able to distinguish cyclones in any of their stages of development. It is realized that not all cyclone shapes will be analyzed correctly, but as more cyclones are analyzed, the program can be improved to accomodate the more complicated cloud shapes associated with various cyclone systems. This is only the beginning of the "learning" stage for the computer algorithm. It is evident that the program can become much more precise as more satellite images are analyzed.

REFERENCES

Guymer, L.B., 1978: Operational Application of Satellite Imagery to Synoptic Analysis in the Southern Hemisphere. Technical Report #29, Commonwealth Bureau of Meteorology, Melbourne, AUtralia, 83 pp.

Kelly, G.A.M., 1978: Interpretation of Satellite Cloud Mosaics for Southern Hemisphere Analysis and Reference Level Specification. Monthly Weather Review, 106, 870-889.

Nagle R.E. and C.M. Hayden, 1971: The Use of Satellite-Observed Cloud Patterns in Northern Hemisphere 500-mb Numerical Analysis. NOAA Technical Report, NESS 55, U.S. Department of Commerce, Washington D.C., 25 pp.

Suomi, .V.E, R. Fox, S.S. Limaye and W.L. Smith, 1983:McIdas III: A Modern Interactive Data Access and Analysis System, Journal of Climate and Applied Meteorology, 22, pp. 766-778.

Troup A.J. and M.A. Streten, 1972: Satellite Observed Southern Hemisphere Cloud Vortices in Relationship to Conventional Observations. Journal of Applied Meteorology, 11, pp. 909-917.

ORIGINAL PAGE IS
OF POOR QUALITY